SLAC-589
UC-404
(SSRL-M)

CHARGE DYNAMICS IN LOW DIMENSIONAL PROTOTYPE CORRELATED SYSTEMS: A VIEW WITH HIGH-ENERGY X-RAYS*

Md-Zahid Hasan

Stanford Synchrotron Radiation Laboratory
Stanford Linear Accelerator Center
Stanford University, Stanford, California 94309

SLAC-Report-589
November 2001

Prepared for the Department of Energy
under contract number DE-AC03-76SF00515

Printed in the United States of America. Available from the National Technical Information Service, U.S. Department of Commerce, 5285 Port Royal Road, Springfield, VA 22161

* Ph.D. thesis, Stanford University, Stanford, CA 94309.

CHARGE DYNAMICS IN LOW DIMENSIONAL PROTOTYPE CORRELATED SYSTEMS : A VIEW WITH HIGH-ENERGY X-RAYS

A DISSERTATION

SUBMITTED TO THE DEPARTMENT OF APPLIED PHYSICS

AND THE COMMITTEE ON GRADUATE STUDIES

OF STANFORD UNIVERSITY

IN PARTIAL FULFILLMENT OF THE REQUIREMENTS FOR THE DEGREE OF

DOCTOR OF PHILOSOPHY

Md-Zahid Hasan

November 2001

I certify that I have read this dissertation and that in my opinion it is fully adequate, in scope and quality, as dissertation for the degree of Doctor of Philosophy.

_____

Zhi-Xun Shen
(Principal Advisor)

I certify that I have read this dissertation and that in my opinion it is fully adequate, in scope and quality, as dissertation for the degree of Doctor of Philosophy.

_____

Robert B. Laughlin
(Co-Advisor)

I certify that I have read this dissertation and that in my opinion it is fully adequate, in scope and quality, as dissertation for the degree of Doctor of Philosophy.

_____

Douglas D. Osheroff

I certify that I have read this dissertation and that in my opinion it is fully adequate, in scope and quality, as dissertation for the degree of Doctor of Philosophy.

_____

Eric D. Isaacs

Approved for the University Committee on Graduate Studies

_____

Abstract

The electronic structure of Mott systems continues to be an unsolved problem in physics despite more than half-century of intense research efforts. Well-developed momentum-resolved spectroscopies such as photoemission and neutron scattering cannot directly address problems associated with the full Mott gap as angle-resolved photoemission probes the occupied states and neutrons do not couple to the electron's charge directly. Our observation of dispersive particle-hole pair excitations across the charge gap (effective Mott gap) in several low dimensional prototype Mott insulators using high resolution resonant inelastic x-ray scattering suggests that the excitations across the gap are highly anisotropic and momentum dependent. The results indirectly provide some information about the momentum dependence of unoccupied states in these correlated systems. The x-ray scattering results are complementary to the electron scattering results by the possibility of studying the excitations in the high momentum transfer regimes (near the zone boundaries and corners). This is also demonstrated in case of studying plasmons near the wave vector regime where Landau damping starts to dominate. X-ray scattering also allows one to probe the symmetry characters of localized electrons and the excitations through the strong polarization dependence of scattering near a core resonance. The study of charge-orbital localization is demonstrated in case of manganese oxides. Given its deeply bulk-sensitive and weak-coupling nature and the ability to probe dispersive behavior of charge fluctuations over several Brillouin zones, inelastic x-ray scattering shows the promise to become an important experimental tool to study the electronic structure of complex quantum systems.

Acknowledgements

The years at Stanford have been fantastic for me. I started out working with Prof. Artie Bienenstock who then was the director of the synchrotron division (SSRL) of the Stanford Linear Accelerator Center (SLAC). Artie told me his lab had a "flavor of both particle physics and condensed matter physics". That flavor caught on my full imagination and I joined his group. I learned that SSRL was great for doing high-energy x-ray scattering to study various condensed matter systems. It set the stage for my graduate career.

My principal academic interest in graduate school rotated around understanding (studying) the phases of many electron systems more specifically the Mott systems using momentum-resolved spectroscopies. First-time I learned about Mott phenomena was in connection to disordered systems (negative Hubbard-U systems) from the works of Phil Anderson. Many electronically disordered systems are among the most difficult systems to understand and soon I came to know that even the apparently simple Mott problem in a perfectly ordered square lattice is not understood. As it is believed by many to be the problem of high T_c superconductivity. Artie suggested that Prof. Z-X. Shen, a world-expert on angle-resolved photoemission at Stanford, was using SSRL facilities to study superconductivity. That was the connection to my current advisor whom I approached with the idea that I wanted to look at Mott gap in a quasi-1-D spin-Peierls lattice ($CuGeO_3$) using x-rays. Prof. Shen's enthusiasm for science, intellectual motivation and energy for "exciting experiment"s quickly convinced me to officially join his group and become a member of the ARPES group. I am deeply grateful to him for letting me try many "crazy" ideas for experiments at almost anywhere in the world as necessary. The four years spent with him was the highlight of my graduate school. I am proud to be his student. I am deeply indebted to him for guiding me throughout my PhD years.

I thank all the members of our group. Paul White showed me how to angle-resolve the photo-excited electrons at SSRL and being a great friend guided me with many advices that came out among the most useful ones. I am deeply indebted to Paul. I am indebted to Jeff Harris whom I did the 8-plane BSCCO experiment with, Stuart who showed me how to tighten flanges while I helped him to do his famous "Cerium-experiment" to look for the-Kondo-like physics, Changyoung – “the discoverer” of spin-charge separation helped me with crystals along with Filip in my early days in Shen-group. Thanks to Chul, Matthias and Anne. Donglai and I competed to take over BSCCO projects when Jeff left – Donglai won, I lost and was "exiled" to Berkeley to help out build the HERS system in Berkeley. I spent a year ‘n a half there, besides helping out HERS I tried to do photoelectron holography on manganites with Xingjiang, Scot, Zhou-Xin and Eddie. Never saw the hologram, the experiment failed but I learned all one could about UHV systems and it was fun. I am thankful to Donglai, Filip, Pasha, Peter, Kyle, Donghui, Andrea and Akihiro for friendship. I regret the opportunity to do experiments with them directly. Alessandra had been my principal "ARPES-partner" in two projects and special thanks to Alessandra and Xingjiang for helping me to do the insulating-stripe adventure in Berkeley.

I am deeply indebted to Dr. Zahid Hussain for guiding me through, in many senses working as my supervisor, during my stay at the Advanced Light Source (ALS) in Berkeley. I spent countless hours chatting with him and there was always something he had to offer anew. The great thing we did together was to come up with an idea how to build an efficient spectrograph to work in the soft x-ray regime which could be used as an inelastic scattering spectrometer. I still can not believe I was given the honor to first author that proposal and we got funded beyond expectation for that grant proposal. In many senses of the word, I am proud to have become his experimental "protege".

No matter what I did at Stanford or at Berkeley I always continued my inelastic adventure. I won a student research grant – thanks to the chemistry department at Brookhaven (Hamilton Scholarship, 1997) which opened the door for me to explore the great synchrotron facility there in the eastcoast – National Synchrotron Light Source (NSLS). I am deeply thankful to Eric Isaacs of Bell-Laboratories for a fruitful collaboration over the last 4-5 years. Eric Isaacs, Peter Abbamonte and Chi-Chang Kao showed me how to use the beamline. Peter taught me all about x-ray analyzers. Peter knew almost everything about almost everything related to the synchrotrons and used to bring good bagels at the beamline. I had a summer spent on doing standing wave (XSW) scattering at Brookhaven. I thank Erik Nelson, Joe Woicik (NIST), Lonny Berman, Bary Karlin

and Dave Heskett (Rhode Island) for a good collaboration which resulted in a good paper. At SSRL/Stanford, I had opportunities to work with John Arthur, Sean Brennan, Piero Pianetta, Martin Greven, Simon Larochelle, Alex Panchula, Hope Ishii, Anneli Munkholm, Ingrid Pickering and Ian Millet. I am thankful to all of them. I am very much thankful to Prof. Pedro Montano (Univ. of Illinois) and his group at the Advanced Photon Source (APS) of the Argonne National Lab for great support and fruitful collaborations. Thanks to Mark Beno, Jenifer Linton, Mark Engbreston, Jeane Cowan and others at the BESSRC-CAT of APS. During concurrent runs at the APS, Yinwan help me run the Compton scattering otherwise it could not be run. Thanks to Zahir who is a good friend and helped me with the experiments at APS despite his busy schedule. It was an honor for me to have collaborated with Sunny Sinha. On the sample side I had help from many - Hiroshi Eisaki (Stanford), Lance Miller (Ames Lab), Paul Canfeld (Ames Lab) and Y. Tokura (Tokyo) - some of the world's bests. I thank all of them for providing good quality crystals. Hiroshi has been a great friend besides a collaborator. There was always something new to learn from him. I thank Abhay Shukla, Clem Burns, Jean-Pascal Rueff for helping me during experiments at the European Synchrotron Radiation Facility (ESRF) at Grenoble, France. I have very much enjoyed the spring time in Grenoble. I also thank Fulvio Parmigiani, Luigi Sangaletti, and Gabrielle Ferrini for great hospitality during my experiment at the Italian synchrotron (ELLETA) near Trieste. I am also indebted to Kenji Tsutsui, Takami Tohyama and Prof. Maekawa (Tohoku, Japan) for performing the numerical calculations of the scattering cross-sections on Mott systems. Thanks to Shou-chang Zhang, Mac Beasley, Ted Geballe, Doug Osheroff, Bob Byer, Andre Linde, Walter Harrison and others at Stanford for many helpful discussions. I am thankful to Marilyn Gordon and Paula Perron for keeping me on-track through the administrative maze of the degree process.

I am deeply thankful to Bob Laughlin for always having plenty of time to talk whenever I needed to chat physics with him. His depth, originality and teaching style have had strong impressions on me. I feel honored having to know him. I am also thankful to Seb Doniach specially for helping me with my recent interests in big molecules. Much of what I think important in physics in a broad sense have had Bob and Seb’s combined influence as they have been my great mentors in graduate school.

I thank my parents and my brother and my sister for their support and love throughout. Among other things my parents have always inspired me to serve humanity at large through science, through philosophy, through education, through life.

I am deeply indebted to my wife, Sarah. Undoubtedly she has been the one to suffer for my idiosyncratic ***P***ermanent ***h.***ead ***D.***amage process. Even when we were away from each other, Sarah pursuing her degree at MIT and I on the other end of the continent at Stanford, she helped me through many difficult times with amazingly balanced and wise advice. I am what I am for her love, support and companionship throughout. Thank you Sarah because you brought me the joy, meaning, success, fulfilment and happiness of my life.

Zahid Hasan
November 2001
Stanford, California

To

My wife,

Sarahmonee

"Asceticism is not that one should not own things

but

nothing should own one for one is already owned by the One"

An Unknown One

Contents

List of Figures

List of Tables

Chapter 1

"More is Different"

Over the last century, physics went through major revolutions and our understanding of nature has significantly deepened and broadened over a fairly short period of time. Despite a great understanding of the fundamental forces and the basic essence of matter at the microscopic levels, it is becoming increasingly clear that this knowledge of microscopic world is of little or very limited use in predicting or describing or explaining the macroscopic behavior of matter. Even the dynamics of a system of three quantum particles can not be predicted exactly. In fact what we see around us – the macroscopic visible world – even the tiniest objects of which consist of particles of the order of 10^{23}. Tracking the motion of all these particles is virtually impossible - even if one could manage to do that it isn't very useful either. It turns out in many cases a large collection of particles would exhibit some properties that can not really be traced in the individual particle's motions pointing to a "holistic" reality (metaphysics) of nature. As Phil Anderson of Princeton University put it aptly "More is different".

There are many many-particle systems in nature and they span over a large range of length scales – cluster of galaxies exhibit complex dynamics at the scale of several million light-years, planetary systems around a star rotates about within several light-hours, a vast ocean containing zillions of water molecules shows nontrivial current patterns, a tiny fish consisting of billions of macromolecules swimming inside the ocean self-organizes and reprodues itself, a strand of RNA inside that fish does its own job of protein productions of thousands of types, each protein molecule consisting of tens of thousands of atoms takes a shape (folds into) within a microsecond and performs a very specific function. Molecules in purple bacteria absorb sunlight and pumps a proton inside a cell whereas photosynthetic centers in green leaves rearranges the electrons in the molecules and produces the primitive form of food. Even smaller particles such as electrons often get together and do strange things. Under very cold conditions electrons in a metal cooperate in a way that they travel through the solid without bouncing off anything a long long way. Most of these properties are some sort of collective behavior of many particles in nature. Condensed

matter physics is the study of many particle systems to account for their macroscopic collective properties. It provides a language and framework to describe collective properties of matter when a large number of particles interact with each other with well-understood forces. To a great extent the job of condensed matter physics is to understand the many-body groundstates or phases of matter, their excitations and relaxations and changes of phases (phase transitions) from one into the other.

Quantum Many-Electron Systems

Among the smallest-scale many-particle systems are the quarks in a nucleon or the electrons in a magnet or a superconducting crystal. In many cases, the small-scale many body systems have the strangest properties because of the proximity to the applicability of the uncertainty principle. In this thesis we would be focused on the many electron systems. The study of many electron systems began with the advent of quantum mechanics. So far a reasonable understanding has been achieved to describe electronic, magnetic and optical properties of many metals, insulators, semiconductors, low critical temperature superconductors, magnets and quantum Hall systems. One of the greatest challenges of many electron physics stems from the fact that there is no straightforward way to treat the effects of the strong Coulomb interaction in an interacting electron system.

Over the last two decades, the discovery of high temperature superconductivity, colossal magnetoresistance and many other unusual electronic, magnetic and optical properties have led to the extensive research interests in strongly interacting many-electron quantum systems. Such systems are characterized by a state of matter where large Coulomb interaction dominates the physics. As a consequence the low-temperature resistivity (to electronic conduction) in these systems shows the existence of a large energy gap - generally known as the Mott gap. Existence of this charge-gap is in contrast to the conventional band theory of electronic structure as that would predict these systems to be conducting (metallic). A Mott insulator is fundamentally different from a conventional band insulator or a semiconductor where the conductivity at low

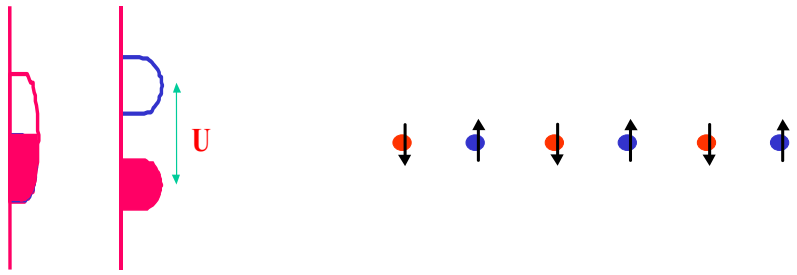

Figure 1.0.1 Strong local Coulomb interaction leads to a breakdown of conventional effective one-electron bandstructure and drives a system into an insulator. **(Left)** If the Coulomb interaction, U, is larger than the one-electron bandwidth a system shows an energy gap in the electronic excitation spectrum. **(Right)** Strong Coulomb interaction also causes a system to magnetically order. In the absence of orbital degeneracy Mott insulators often exhibit antiferromagnetism.

temperatures is blocked by the Pauli exclusion principle where as in a Mott insulator, charge conduction is blocked instead by direct electron-electron Coulomb repulsion. In such as system, only the spin degrees of freedom of the electron can fluctuate and such virtual charge fluctuations in a Mott insulator generate an effective magnetic interaction among the spins. In many such systems, this leads to long-range antiferromagnetic order. It is believed that the key to understand the unusual electronic and magnetic properties in many transition metal oxides such as non-

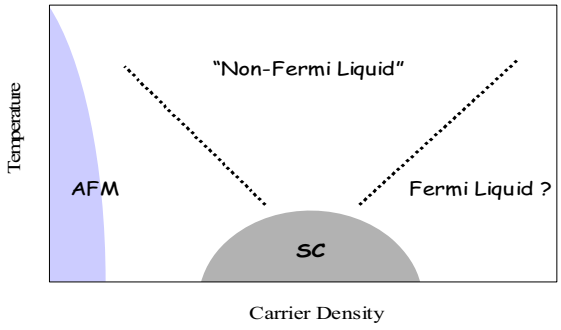

Figure 1.0.2 Breakdown of Fermi liquid behavior in doped Mott insulators. In doped Mott insulators such as high T_c copper oxides a standard paradigm of condensed matter physics - the Fermi liquid behavior breaks down due to strong electron-electron interactions.

Fermi-liquid behavior, psuedo-gapped metallic phase, high T_c superconductivity, charge-orbital striping, colossal magnetoresistance or giant optical nonlinearity is in the existence of a Mott state in their parent compounds. This suggests the importance of a thorough study of the charge and spin dynamics of these systems.

Within the framework of quantum mechanics, a system is typically described by a set of quantum numbers. These quantum numbers are the quantities measured and extracted from various experiments. Typically, an experiment on a system measures some response of the system under some probe and then the response is analyzed to relate to some intrinsic properties of the system. Spectroscopies using scattering techniques are among the most basic tools for condensed matter experimentalists. The general goal of scattering studies of condensed matter systems is to relate the kinematic parameters of the probes to the intrinsic quantities of the system under study.

A variety of spectroscopies have been used to study complex Mott insulators so far. The characterization of various groundstates and excitations from those states are the goals of these spectroscopies. Charge and spin localization, ordering and dynamics are among the central issues of strongly correlated electron systems Mott insulators being the simplest of this class. Neutrons, neutral particles with half-integral spins have been used to study the spin dynamics of these systems. As for the charge, momentum-resolved spectroscopies such as x-ray induced electron emission (angle-resolved photoelectron spectroscopy) has been successful in characterizing the electronic states of a system that are occupied, whereas, light scattering and independently, electron scattering are limited to measure excitations involving only low momentum transfers and unable to measure all the momentum information of interest. It turns out, as we would see in this thesis, that the high energy and momentum resolution x-ray scattering as a relatively novel spectroscopy can play a key role in elucidating the "charge" physics of these strongly correlated electron systems by resolving excitations in the momentum space.

In this thesis, I would present several momentum-resolved x-ray scattering study of charge dynamics and electronic order (localization) in Mott systems by starting with studying a simple non-Mott system, a nearly-free electron gas, to demonstrate the x-ray scattering as a technique to probe charge dynamics. In case of the simplest many-electron system - a weakly interacting electron gas we found that the dominant contributor to density fluctuations was a coherent collective mode, namely, a plasmon whose energy increases quadratically of its momentum. Perhaps the highlight of this thesis is the study of momentum-resolved charge fluctuations in low

dimensional Mott insulators. Fluctuations dominate in low dimensional systems due to the existence of kinematic singularities. Many low dimensional systems exhibit exotic groundstates. Our momentum-resolved inelastic x-ray scattering studies show that in contrast to the mean field theories, charge fluctuations in 1-D are more dispersive than in 2-D This is the first study of momentum-resolved charge dynamics in low dimensional Mott insulators covering the entire Brillouin zone. Our study of charge localization in doped Mott insulators fell little short of its kind to be the first but we studied a system that shows the most dramatic effect of long-range ordering of electrons in creating a rich "Wigner crystal" pattern in a Mott system.

"What Matters ?"

The study of many-electron systems not only can potentially unravel important issues essential to build new technologies for a better (more convenient?) society as it is fairly likely in the case of superconductivity at high temperatures or strong sensitivity of magnetic materials or the phenomena of fast optical switching, the concepts developed may find applications in diverse disciplines as it has been the case of most branches of physics.

The interplay of charge, lattice, spin and orbital degrees of freedom play important roles in determining various electronic and magnetic properties of transition metal oxides. In many of these systems one can identify three fundamental parameters : an electron's hopping freedom as

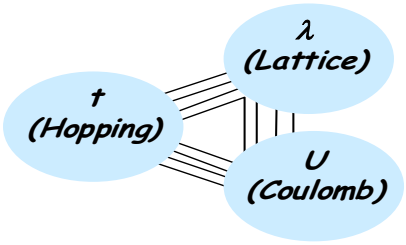

Figure 1.0.3 Fundamental interactions among electrons : The relative magnitudes of the hopping (t) or electron's delocalization energy, electron-lattice coupling (λ) and electron-electron Coulomb interaction (U) determine the phase ("groundstate") of a many-electron system.

granted by the quantum mechanics, its tendency to associate with the lattice (in crystalline solids) and its ability to see other electrons (Coulomb interaction). Depending on which of these parameters dominate or balance each other the many-electron system takes a phase. For example, if the hopping dominates the system is a metal or if the electron-lattice interaction dominates it can be a Peierls insulator or if the electron-electron coupling overrides other interactions the system can behave like a Mott insulator with long-range antiferromagnetic order.

The spectrum of phases (phase diagrams) observed in many interacting electron systems are created by competing orders due to frustrated or competing interactions. One such class of phases in doped Mott insulators are the stripes. The striped phases are a consequence of

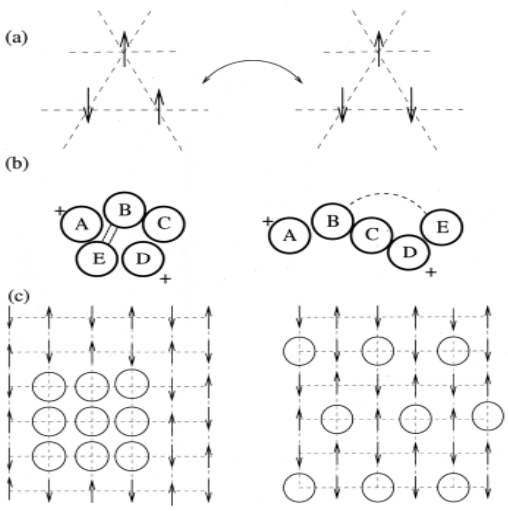

Figure 1.0.4 Competing interactions lead to different configuarations of spins, electrons and atoms : (*a*) For antiferromagnetically (AF) coupled Ising spins on a triangular lattice one of the AF bonds is always broken. (*b*) Folding of heteropolymers can be frustrated by the competing, e.g., bonding (indicated by solid lines) and Coulomb interactions (indicated by +) between different constituents (A-E). (*c*) AF interactions in doped transition metal oxides energetically favor a phase-separated state, which is unfavorable for the Coulomb interaction, whereas the Coulomb interaction favors a Wigner crystal state that is unfavorable for the AF interactions; the result of the competition (frustration) yields formation of patterns. (Courtsey : R. B. Laughlin [1]).

competition between strong magnetic interactions and Coulomb repulsions. Depending on the strength of these interactions the electrons' charge and spin distributions can take many different patterns (Fig.1.0.4(c)). These behaviors are not limited to many-electron systems. Similar or analogous competitions are also seen in biomacromolecules (Fig.1.0.4(b)). It is likely that the understanding developed in interacting electron systems can be applied elsewhere.

As for the experimental methods when a spectroscopic technique has wide applicability it is likely to elucidate many pieces of physics that have underlying connections. This is hoped for our efforts in developing x-ray scattering as a probe of charge dynamics of condensed matter systems. Dynamics of condensed matter systems spans a wide range of scales from the time scale of several seconds for slow protein folding to the fast oscillations of electrons in a plasmon seen in metals. In this thesis I stayed focused in studying the fast motion of electrons in metals and insulators. As it will be shown, inelastic x-ray scattering is an ideal and much needed probe for studying such fast motions of electrons.

Chapter 2

X-rays to Study Charge Dynamics

2.1 Inelastic X-ray Scattering to Probe Electron Dynamics

The general goal of scattering studies of condensed matter systems is to relate the kinematic parameters of the probes to the intrinsic quantities of the system under study. In case of x-rays scattering from a system, the experimental goal is to measure the cross-section as a function of the transferred momentum and transferred energy and relate them to some property of the scattering system. The coupling of the electromagnetic (x-ray) field to the scattering electron system is represented by the Hamiltonian (in the non-relativistic limit) :

$$H_{Int} \sim \Sigma_j (e^2/2mc^2) \, . \, \mathbf{A}_j^2 + \Sigma_j (e/mc) \, \mathbf{A}_j \, . \, \mathbf{p}_j \qquad (2.1.1)$$

where the sum is over the electrons of the scattering system, **A** is the vector potential of the electromagnetic field and **p** is the momentum operator of the scattering electrons.

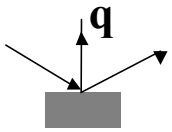

X-ray in & X-ray out :
Charge density fluctuates in the system

Figure 2.1.1 As x-rays scatter from a medium it perturbs (fluctuates) the charge density and provides information about spatial and temporal distributions of charge density.

To describe two photon processes (photon-in photon-out), the first term in the Hamiltonian which is quadratic in the vector potential can be treated to first order whereas the second term being linear in **A** has to be treated to second order. For an x ray of energy ω_1 , polarization $\boldsymbol{\varepsilon}_1$, and

momentum $\mathbf{q}_1$ ($\hbar$=1) scatters weakly from the electronic system in an initial (ground) many-body state |i> to a final state (ω_2 , $\boldsymbol{\varepsilon}_2$, $\mathbf{q}_2$) . This leaves the system in an excited state |f> with momentum $\mathbf{q} = \mathbf{q}_2 - \mathbf{q}_1$ and energy $\omega = \omega_1 - \omega_2$. In the nonrelativistic limit ($\omega_1 << mc^2 \sim 500$ KeV), the matrix element for scattering (assuming both the initial and the final photon state as simple plane waves) :

$$M = (e^2/mc^2)^2 [\langle f| \boldsymbol{\varepsilon}_2 . \boldsymbol{\varepsilon}_1 \boldsymbol{\rho}_{\mathbf{q}} |i\rangle + (1/m) [\{(\langle f| \mathbf{p}_{\mathbf{q}_2} . \boldsymbol{\varepsilon}_2 |n\rangle\langle n| \mathbf{p}_{\mathbf{q}_1} . \boldsymbol{\varepsilon}_1 |i\rangle)/(E_n - E_i - \omega_1 + i\delta)\} + \{(\langle f| \mathbf{p}_{\mathbf{q}_1} . \boldsymbol{\varepsilon}_1 |n\rangle\langle n| \mathbf{p}_{\mathbf{q}_2} . \boldsymbol{\varepsilon}_2 |i\rangle)/(E_n - E_i - \omega_2 + i\delta)\}] \quad (2.1.2)$$

where $\boldsymbol{\rho}_{\mathbf{q}} = \Sigma_j e^{iq.r}$ is the density operator, $\mathbf{p}_{\mathbf{q}} = \Sigma_j e^{iq.r}$ is the momentum operator. The energies E_i (E_n) are the energy of the ground (intermediate) state of the interacting many-body system with correlated wave functions (|i>, |n>) [2].

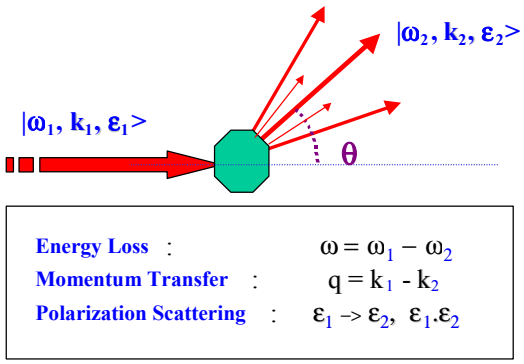

Figure 2.1.2 Kinematics of x-ray scattering : In a typical x-ray scattering experiment one measures the intensity of the scattered beam as a function of energy-loss (ω), change of momentum ($\mathbf{q}$) and change in polarization ($\boldsymbol{\varepsilon}_1 . \boldsymbol{\varepsilon}_2$) of x-ray beam.

When ω_1 is not near the binding energy of an atomic core state, Eq. 2.1.2 is dominated by the first term on the right-hand side and the scattering cross section (at zero temperature) can be written as

$$d\sigma/d\omega d\Theta = r_o^2 (\boldsymbol{\varepsilon}_1.\boldsymbol{\varepsilon}_2)^2 \Sigma_f |\langle f| \boldsymbol{\rho}_{\mathbf{q}} |i\rangle|^2 \delta(E_f - E_i - \omega) \quad (2.1.3)$$

where, $r_o^2 = (e^2/mc^2)^2$

We define :

$$S(\mathbf{q}, \omega) = \Sigma_f \ |\langle f| \boldsymbol{\rho}_{\mathbf{q}} |i\rangle|^2 \ \delta(E_f - E_i - \omega) \qquad (2.1.4)$$

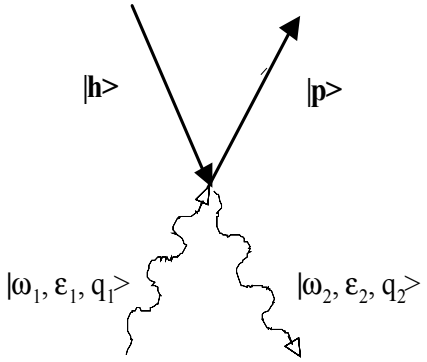

Figure 2.1.3 Scattering in the first order : The first term in Eq. 2.1.2 is typically described by a single vertex process in perturbation theory. The diagram suggests that a photon-in photon-out process creates a particle (|p>)-hole (|h>) pair in the system and energy, momentum and polarization are conserved through the scattering process.

The coupling to the electromagnetic field to the charge (Thomson cross-section) is described by the term $(e^2/mc^2)^2$: $r_o^2 = (e^2/mc^2)^2 = 10^{-26}$ cm^2 ; which is weak enough for scattering to be treated in lowest-order perturbation theory (Born approximation). $S(\mathbf{q},\omega)$ is known as the dynamic structure factor. It reflects the properties of the scattering system in the absence of the perturbing probe. The dynamic structure factor can be written into a form that reveals the best physical essence of the information about the scattering system [4]:

$$S(\mathbf{q},\omega) = \int dt \, e^{-i\omega t} \langle I \mid \Sigma_{jj'} e^{-i\,\mathbf{q}\cdot r_{j'}(t)} e^{i\,\mathbf{q}\cdot r_j(0)} \mid I \rangle \qquad (2.1.5)$$

Taking into account that $e^{i\mathbf{q}\cdot r_j(0)}$ determines the phase of the scattering amplitude of an electron at r_j, one can interpret $S(\mathbf{q},\omega)$ in the classical limit to be the Fourier transform of the correlation of scattering phase factor pairs at different times. This suggests that inelastic x-ray scattering (away

from any core resonances) measures a two particle function the charge-charge correlation function.

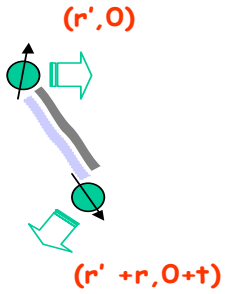

Figure 2.1.4 Two-particle correlation : The dynamic structure factor measures the spatial and temporal correlation of motions of two particles in a system.

The dynamic structure factor can also be related to the dielectric response function $\varepsilon(\mathbf{q},\omega)$ via the fluctuation-dissipation theorem [4][5]:

$$S(\mathbf{q},\omega) = (-\mathbf{q}^2/4\pi^2e^2n)\ \mathrm{Im}\ (\varepsilon^{-1}(\mathbf{q},\omega)) \qquad (2.1.6)$$

Where $\varepsilon^{-1}(\mathbf{q},\omega)$ is formally defined in terms of the response of the electron system to an external longitudinal potential $\phi_{ext}(\mathbf{q},\omega)$:

$$\varepsilon^{-1}(\mathbf{q},\omega) = \phi_{Total}(\mathbf{q},\omega) / \phi_{ext}(\mathbf{q},\omega) \qquad (2.1.7)$$

In a crystal, $\varepsilon^{-1}(\mathbf{q},\omega)$ reflects the lattice induced inhomogeneity. In this sense, the dynamic structure factor of an electron system is determined by transitions between occupied and unoccupied one-electron states (in a band system), induced by the momentum transfer **q** and the energy transfer ω. In other words, $S(\mathbf{q},\omega)$ is connected with the creation of electron-hole pairs [5].

Since $S(\mathbf{q},\omega)$ is the fourier transform of the correlation of scattering phase-factor pairs at different times it is dominated by different types of excitations at different regimes of momentum-transfers (**q**). For $\mathbf{q}.\ \mathbf{r} \ll 1$, the interference between the amplitudes scattered from different particles of the system is of importance where the phase-factor, exp(iq.r), oscillates very slowly in real space and large interference occurs in the system making the probe sensitive to long-range collective

excitations. For **q. r** >> 1, the phase-factor oscillates very fast in real space and hardly any interference occurs in the system and essentially a single particle property is observed in this limit [2][3].

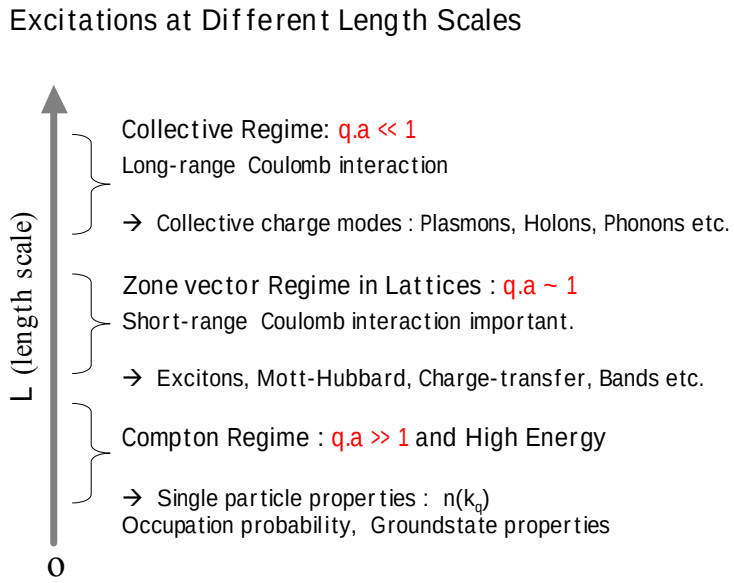

Figure 2.1.5 Excitations at different length scales : For small q one would be sensitive to the collective modes (plasmons, phonons etc.), for q in the intermediate regime one is sensitive to the bandstructure of a material whereas for very large q's and high energies the scattering would measure the single-particle density of states projected along the scattering vector.

When the incident x-ray energy is tuned near to the binding energy of a deep core level of an atom in the system, the second term in Eqn. 2.1.2 dominates the cross section. In this case the energy denominator can vanish and the cross section can become large [6]-[10]. However, the cross section also becomes more complicated than Eqn. 2.1.3, in that the nature of the coupling to the excited state |f> depends on the presence of the intermediate state |n> which contains an almost real, strongly perturbing core hole. Nevertheless the cross section can still be written as in Eqn. 2.1.3. [10]. It is

$$d\sigma/d\omega d\Theta = r_o^2 \, (\varepsilon_{1\alpha}.\varepsilon_{2\beta})^2 \; \Sigma_f \; |\langle f| \mathbf{O}_q^{\alpha\beta} |i\rangle|^2 \; \delta(E_f - E_i - \omega) \qquad (2.1.8)$$

The finite **q** resonant Raman operator $\mathbf{O}_q$ conserves momentum and gets large when ω_l is near an absorption edge. In principle $\mathbf{O}_q$ is a function of ω_l , $\mathbf{q_1}$, $\mathbf{q_2}$, $\boldsymbol{\varepsilon}_1$, $\boldsymbol{\varepsilon}_2$. The tensor character of $\mathbf{O}_q^{\alpha\beta}$ arises from the momentum operator in the matrix elements. This implies that it can couple to transverse charge and spin excitations as well as longitudinal excitations. No one has successfully given a complete many-body description of the operator $\mathbf{O}_q^{\alpha\beta}$. So far resonant scattering has been treated case by case. One simple approximation that has been discussed [10] is to assume that the intermediate state energy denominator can be replaced by some average energy which would allow one to sum over intermediate states and reduce the problem to the calculation of an autocorrelation function, as in the nonresonant case, of a simple operator such as $\boldsymbol{\rho}_q$. Such approaches are not generally valid but have been discussed in connection with resonant scattering from d-electron systems with some success [10].

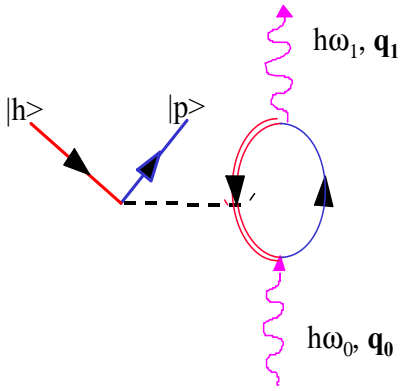

Figure 2.1.6 Perturbation method diagram describing x-ray scattering under some resonant condition. In the simplest form resonant scattering near an atomic core edge in a solid contains two particle-hole pairs - one, a core-hole and an excited electron pair (right) and the other pair is in the valence electron system a hole in the valence (occupied) band and an electron in the conduction (unoccupied) band (left). Under certain conditions the core particle-hole pair enhances the scattering cross section for the valence particle-hole pair [10].

When the incident x-ray energy is far from any atomic absorption edges in the sample, inelastic scattering, as discussed earlier, measures the dynamic structure factor of the electronic excitation spectrum. In some materials, the low-lying electronic charge excitation spectrum consists of, for example, collective features such as plasmons, spin waves, excitons, and a single-particle-like continuum related to the band structure. The excitation energies of these spectral features and

their momentum dependence can tell us a great deal about the role of electronic correlations, as well as the behavior of the material. Because hard x rays (10 KeV) have a wave vector $k_1 \sim 2\pi/\lambda_1 \sim 5\text{Å}^{-1}$, they are particularly well matched to studying the excitation spectrum over the entire Brillouin zone. However, because the scattering of x-rays from the valence electrons is weak, diffuse, and spread out in energy, and because the absolute energy resolution is so small ($\Delta\lambda_1 /\lambda_1 \sim 10^{-6}$) , most inelastic studies have been restricted to systems with low absorption in order to keep the scattering volume high [12]-[20].

Recently, it has been demonstrated that large enhancements in the scattering cross section can be achieved when the incident x-ray energy is tuned near to an atomic absorption edge of one of the atomic species in the sample [9][10]. Much as resonant enhancements have made it possible to study magnetic structure in a broad range of interesting condensed matter systems [22][23] resonance effects are now making it possible to study interesting electronic excitations previously inaccessible to inelastic x-ray scattering. In many electron systems interactions between electrons makes the possible excited states very interesting and the coupling to them difficult to analyze even for the case of nonresonant scattering. On resonance, because of coupling to the deep atomic core hole, the analysis is more difficult and possibly more interesting as the resonant process allows one to selectively enhance excitations of interest and the direct polarization dependence of the correlation function allows one to identify the symmetry characater of the excitations [10][24]-[26].

X-ray scattering is complementary to other scattering probes. Neutron couples to the spin densities in a system and provides information about magnetization densities and fluctuations (magnons). Electron based techniques such as photoelectron spectroscopy or electron scattering provides information mainly about the electronic states. X-rays couple directly to charge degrees of freedom and work as an "charge-analog" of neutron scattering providing information about charge densities and fluctuations. Unlike electron based probes, X-rays and neutrons interact weakly with the system and probes the bulk properties of a system. In Table-2.1 we compare the fundamental interaction strengths of these probe particles. The major disadvantage of x-rays and neutrons being weak probes is that the typical count rates are quite low and the experiments are slower as compared to electron based spectroscopies.

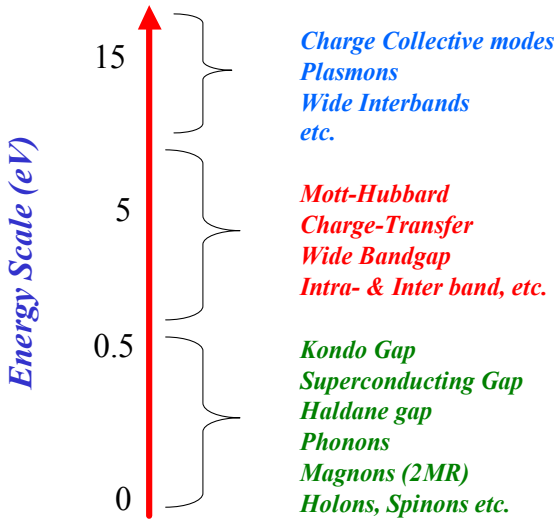

Figure 2.1.7 Electronic Excitations in Condensed Matter Systems : Excitations in condensed matter systems span a wide range in terms of energy scales. Here we list a few of them. Most of the excitations within several hundred millivolts are directly relevant to the properties of solids.

In this thesis, I would describe the study of momentum-resolved charge fluctuations in low dimensional complex insulators where electron-electron Coulomb correlation dominates the physics these systems exhibit. Such experiments have been possible due to the development of 3rd generation synchrotron facilities and the improvements in the quality of optical elements in the x-ray regime. The experiments performed with energy resolutions in the range of 300-450 meV are possible for studying valence electronic excitation. With the fast development of this field experiments with energy resolutions of in the range of 50-100 meV, would soon be possible. Such efforts are already underway at the Advanced Photon Source. Since scattering cross section from lattice vibrations are typically several orders of magnitude larger it is possible to study phonons with 1-2 meV energy resolutions without losing reasonable count rates. In general, inelastic x-ray scattering experiments will complement spectroscopies such as optical raman scattering which are confined to nearly zero momentum and inelastic electron scattering which is confined to small momentum transfer and microscopically thin samples.

Table-2.0.1

Character of Fundamental Probes

Probe	Coupling	Strength	Nature
Neutron	b^2	10^{-24}	Nuclear, Spin
Electron	$(2Ze^2/r_{Bohr}Q_{BZ}^2)^2$	10^{-15}	Coulomb
Photon	$(Zr_o)^2$	10^{-25}	Maxwell, QED

2.2 Experimental Scattering Set-ups

From the earliest experiments of W. Rontgen until very recently, x-rays have been produced most easily by accelarating a beam of electrons to energies in excess of 20 keV and slamming them into a metal target such as copper. The total power consumption of such x-ray tubes is less than 100 kilowatts and the total amount of x rays emitted into 4π steradians is less than 1 watt. Such sources are not bright enough to study dynamical properties of condensed matter systems since the fundamental coupling is fairly weak. In last 10 years or so, electron storage rings have given us access to new much brighter (6 to 10 orders of magnitude) sources of x-rays. The relatively high brightness (photons/steradian/energy band width) of these sources make it possible to achieve very good relative energy resolution ($\sim 10^{-7}$) over a broad range of absloute energy scale of excitations in solids and liquids to the point making experiments feasible. Experiments reported in this thesis were carried out at several different 2^{nd} and 3^{rd} generation of synchrotron facilities (National Synchrotron Light Source at Brookhaven National Laboratory, Advanced Photon Source at Argonne National Laboratory, European Synchrotron Radiation Facility in France).

The inelastic scattering spectrometer is typically a three-axis-of-rotation instrument that contains two major optical elements and a detector (Fig. 2.2.2). The first element is the monochromator crystal which passes a narrow, tunable energy band of width $\delta(h\omega_1)$ centered at energy $h\omega_1$ from the "white" synchrotron source onto the sample. The second optical element is the analyzer crystal which disperses the inelastically scattered radition onto the detector (Fig. 2.2.2).

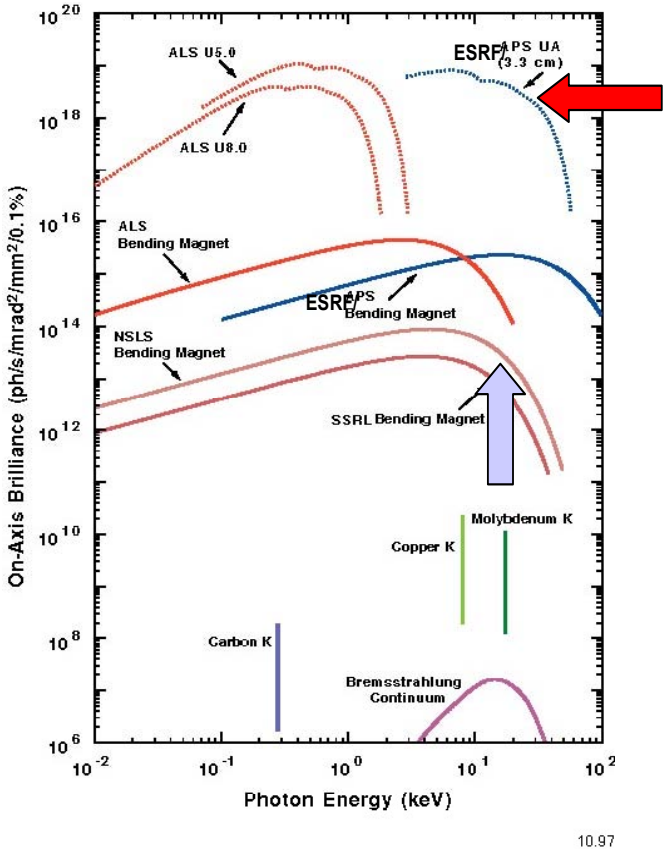

Figure 2.2.1 A comparison of Brilliance (roughly the number of photons emitted in a narrow cone within a narrow spectral region) as a function of photon energy from different types of conventional and Synchrotron x-ray sources. (Technically, Brilliance is defined as number of photons per second per milliradian-squared per millimeter squared within 0.1% spectral bandwidth). The arrow denotes the level of Brilliance needed to study low energy (5-500 meV) excitations from condensed matter systems [27].

There are two principal contributions to the energy resolution of the monochromator. The first derives from the intrinsic angular width of the Bragg reflection in a highly perfect crystal. This finite width which arises from the finite penetration depth over which the x-rays are fully reflected, is called the extinction length and is a function only of the type crystal material (such as

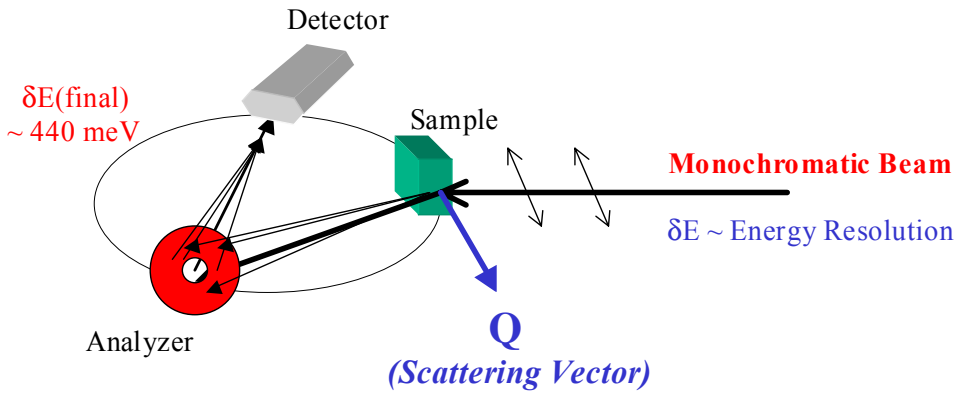

Figure 2.2.2 A schematic describing the key components of an inelastic scattering set-up. Typically, a monochromatic beam is scattered from a sample under study. The scattered beam is collected by an frequency (energy) analyzer through a Bragg reflection and then focused on a detector whose job is to count the number of photons for some specific energy chosen by the analyzer.

Si or Ge) and the order of the Bragg reflection. For example, for the Si(444) Bragg reflection, the extinction length is 31 microns which gives an intrinsic energy resolution $\delta(\hbar\omega_I)$ of about 40 meV at $\hbar\omega_I \sim 8$ keV [3]. The second contribution derives from the angular spread $\delta\Theta_B$ of the incident synchrotron beam which by Bragg's law gives an energy spread :

$$\delta(\hbar\omega_I)/(\hbar\omega_I) = \cot\Theta_B \,.\, \delta\Theta \qquad (2.2.1)$$

where Θ_B is the Bragg angle for the monochromator. Because $\delta\Theta_B$ is about 0.2 milliradians at current sources like NSLS, this energy spread is considerably larger than the Si(444) intrinsic width except very near backscattering where $\cot\Theta_B << 1$. The 3rd generation sources such as the ones at the Advanced Photon Source and European Synchrotron Radiation Facility are better matched to the perfect-crystal monochromators.

Since the inelastic process is incoherent the scattered radiation is spread out into 4π steradians. One therefore needs an analyzer that collects a relatively large solid angle. However, bacause the spectrum in the solid changes on a length scale characterized by the spacing of valence electrons, resolution requirements limit the solid angle to several degrees. The most common setup for a

Ge(733) Analyzer

(Spherically-bent)

Figure 2.2.3 An enlarged view of a diced crystal analyzer Ge(733) [Isaacs, Abbamonte et.al.][11].

high-energy-resolution (< 1 eV) analyzer consists of a large (about 50 cm^2) spherically bent perfect crystal with a 1-m radius of curvature which does indeed collect a few degrees of solid angle. If the Bragg planes are parallel to the surface of the crystal then the analyzer can be considered as a spherical x-ray mirror for a single frequency. Thus, the analyzer produces a single-frequency image of the sources at the detector, and the spectrum is obtained by scanning the input frequency. If ω_I is chosen such that the analyzer crystal backscatters the x-ray, the analyzer can have the intrinsic resolution of the crystal. Such a configuration is optimized when the monochromator resolution is matched to the analyzer. Because we are measuring one energy-shift $h\omega$ at a time, the signal is weak and because in most cases we want many $h\omega$'s an inelastic spectrum can take half a day to collect. We would discuss the various different analyzers and set-ups in connection with the specific systems under study.

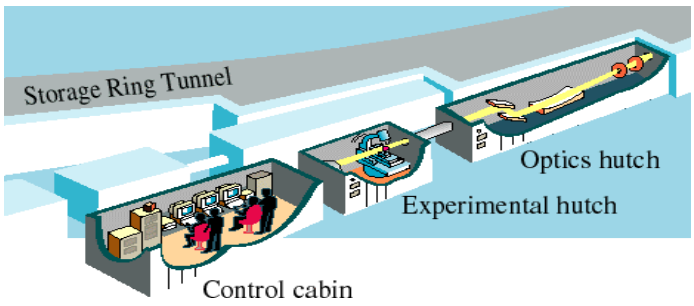

Figure 2.2.4 A standard experimental station at a synchrotron facility consists of three major units : An optics hutch containing the monochromator, an experimental hutch where the sample is set on a goniometer and scattered radiation is analyzed using another set of optics and a control cabin isolated from the experimental hutch where from the experiment can be remotely monitored and controlled.

Chapter 3

Collective Charge Fluctuations in Electron Gases

3.1 Collective Modes and X-ray Scattering

The homogeneous electron gas is one of the oldest and most studied model systems in many electron physics [5][29][30]. The properties of the electron gas (at zero temperature) are determined by the electron density which can be described by r_s (roughly the average distance between the electrons) defined as :

$$r_s = (4\pi n/3)^{-1/3} / a_o$$

where n is the free electron concentration and a_o is the effective Bohr radius, $a_o = h^2/me^2$. Here m is the effective mass of the electron, and e is the electric charge. r_s is approximately the ratio of the Coulomb energy to kinetic energies ($r_s \sim$ <V>/<K.E.>) for the electron in a uniform electron gas at zero temperature. Typical good metals have $2 < r_s < 6$ [31].

As a test experiment characterizing the scattering technique we looked at a simple system – a weakly-interacting gas of electrons as realized in a metal where the excitations are theoretically well studied. Traditionally, collective modes such as plasmons have been studied by electron energy loss spectroscopies (EELS) [32][33]. Electron scattering couples to the longitudinal dielectric function where as x-ray (electromagnetic field) couples to the transverse dielectric function providing complementary information about a system. EELS requires very thin samples with good surfaces under high vacuum, and multiple scattering effects are a significant complication (electron scattering cross-section falls off as $1/q^4$) . As a result, only low momentum transfers can be studied. X-ray scattering techniques lack such limitations but are best suited for relatively low-Z materials with long x-ray absorption lengths, since the ratio of absorption length

to inelastic x-ray scattering length determines the inelastic count rate. The availability of high brightness second and third generation x-ray sources has greatly increased the number of materials and types of studies that can be carried out with inelastic x-ray scattering [3][10][14][15].

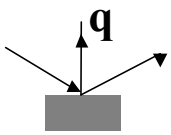

X-ray in & X-ray out :
Charge density fluctuates in the system

Figure 3.1.1 : As x-rays scatter from a medium it fluctuates the charge density. In a weakly interacting electron gas the dominant collective excitation modes are plasmons.

As x-ray scatters from the charge density of a system it creates density fluctuations. In a weakly interacting electron gas the dominant collective excitations are plasmons. It is straightforward to show that the solutions to the Maxwell eqns for an electron gas under the condition of

$$\varepsilon(\mathbf{q}, \omega) = 0 \qquad (3.1.1)$$

(Zeros or Poles of the dielectric function $\varepsilon(\mathbf{q}, \omega_q)$ where $\mathbf{q}$ is the wavevector and ω is the frequency of the excited mode)

implies a nonvanishing value of density modulation $<\rho(\mathbf{q},\omega)>$, in other words, one has a free oscillation of charge density (there being no external field). Such oscillation (longitudinal collective modes) constitutes a net longitudinal electric field in the collective mode [5]. The dynamical correlation function (described in Chapter-2), measured in an inelastic x-ray scattering experiment is related to the dielectric function :

$$S(\mathbf{q}, \omega) = \{\mathbf{q}^2 * \varepsilon_2(\mathbf{q},\omega)\} \;/\; \{4\pi^2 e^2 |\varepsilon(\mathbf{q},\omega)|^2\} \qquad (3.1.2)$$

Plasmons → $\varepsilon(\mathbf{q},\omega_p) = 0$; $S(\mathbf{q}, \omega)$ is singular (divergent) near $\omega = \omega_p$

So the existence of plasmons (undamped) would give rise to a δ-function singularity in S(**q**, ω). Even if the plasmon energy is large, damping of plasmons can arise because of contributions from single- and multi-pair (multi-paticle multi-hole) excitations and from umklapp scattering due to periodic potential in crystalline solids [5][18][19].

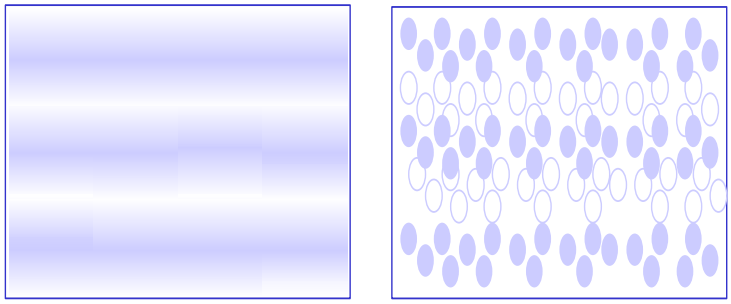

Figure 3.1.2 Plasmons are collective charge density fluctuations in an electron gas (such as a good metal).

3.2 Plasmons in metallic $NiAl_3$

In this section we present inelastic x-ray scattering results from $NiAl_3$ which is a good metal at room temperature. The experiment was carried out on beam line (ID16) at the European Synchrotron Radiation Facility (ESRF, France). The scattering was performed in a standard triple-axis arrangement as described in Chapter 2. The scattered beam was reflected from a spherically bent Silicon (551) crystal-analyzer in a near backscattering geometry and focused onto a solid-state energy-dispersive (AmpTek) detector. This analyzer allowed us to work near Ni K absorption edge with a high resolution setting. The detector was thermoelectrically cooled to achieve low level of random background which is necessary to detect small signals from the sample. For **q**-scans, the incident energy was kept fixed and **q** was varied by rotating the entire spectrometer around the scattering center. For the geometry employed, beam polarization had a nonvanishing component along the direction of the momentum-transfer. The energy resolution was set to about 1.5 eV to gain counts on the plasmon peak. Typically, energy resolution is measured by looking at the elastic scattering on a plastic sample since a plastic sample is fairly

amorphous and scatters almost isotropically in all directions. The background, measured on the energy gain side, was about 10 counts per minute.

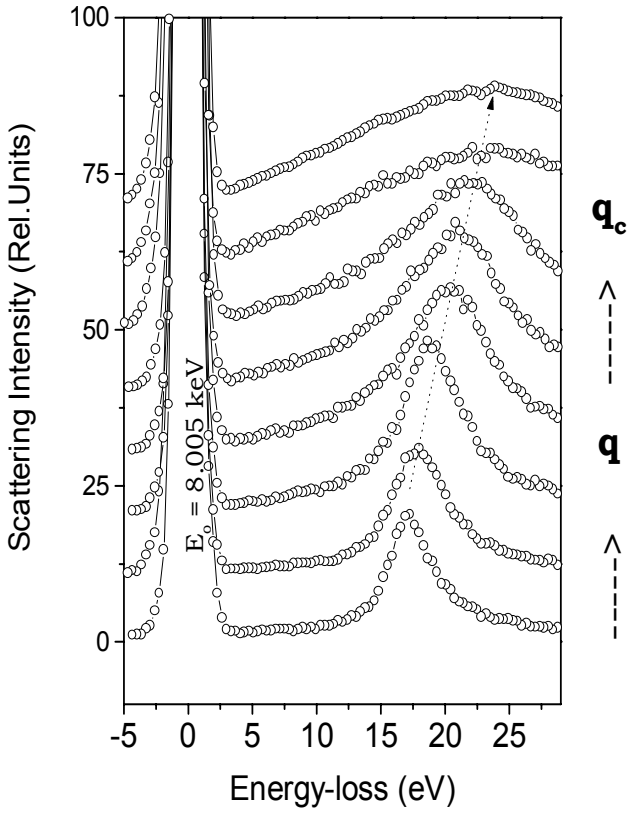

Figure 3.2.1 Momentum-transfer dependence of charge density fluctuations in $NiAl_3$. The excitation feature near 16 eV is identified as a volume plasmon. As momentum transfer (**q**) is varied to larger values plasmon disperses upward in energy, gains in intensity and becomes broader. Beyond some critical wave vector (q_c) a broad feature is seen indicating particle-hole excitations from small to large energies (top two spectra).

Fig. 3.2.1 shows excitation spectrum in $NiAl_3$ as a function of momentum transfer (**q**) into the system. Incident energy was set to 8.005 keV and all the data have been normalized to the incident flux. There are two principal features in these spectra - one at the zero energy-loss another in the energy range of 16 to 22 eV. The feature at zero energy loss appears at all **q**'s. This feature consists of elastic and quasi-elastic scattering and are dominated by lattice imperfections (disorder and defects) and lattice vibrations (phonons). The width of the quasielastic scattering is

set by the energy resolution (~ 1.5 eV) and it tails up to 2 eV on either sides of zero energy (loss or gain). The second feature appears around 16 eV for low **q**'s and moves upward as **q** is increased. As **q** is increased the feature also broadens. As we go beyond some critical value of **q** the feature becomes a continuum of excitation and extends all the way from very low energies to very high energies. The same scans were repeated for a different incident energy (E_o ~ 8.556 keV) and the **q**-dependence of the excitations were found similar. This is shown in Fig. 3.2.2.

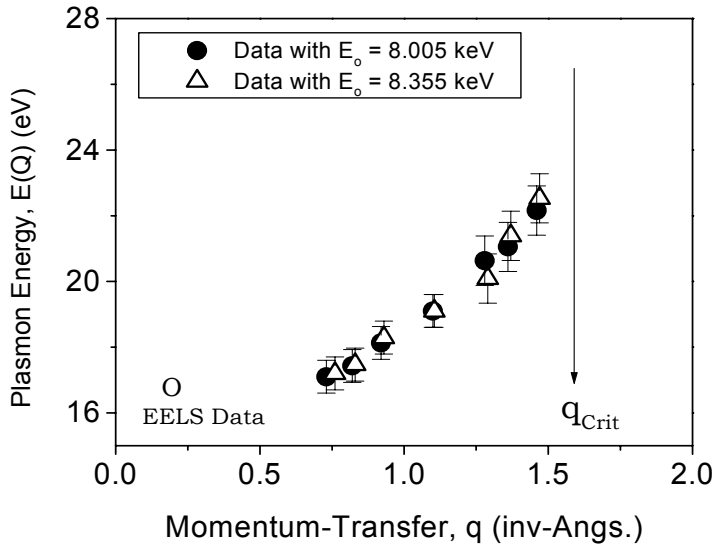

Figure 3.2.2 Dispersion (momentum dependence) of plasmons in $NiAl_3$. Two different types of symbols represent data taken with different incident energies. The data points with solid circle symbols were measured with incident x-ray energy of 8.005 keV and the points with open triangle symbols were measured with incident energy of 8.355 keV.

Based on simple calculations we identified the high energy excitation feature as a plasmon. We also plot the plasmon energy measured by electron energy-loss spectroscopy (EELS) in Fig. 3.2.2 [34] which agrees well with the plasmon energy measured from x-ray scattering at low momentum transfers. X-ray provides a unique way to study the behavior of plasmons at high **q**'s specially near the critical wave vector when overdamping (Landau damping) takes place due to free particle-hole pair excitations. The key experimental result here is that the plasmon is sharp at low **q** and as **q** increases the plasmon disperses upward in energy and grows in width and intensity.

Figure 3.2.3 shows the width of plasmon as a function of **q**. The width data is extracted from dispersions measured with two incident energies to rule out any instrumental systematic errors. The plasmon width changes very slowly before a critical value of **q** is reached when it jumps to a large value. This suggests a sudden turning on of some damping mechanism that desabilizes the coherent collective process.

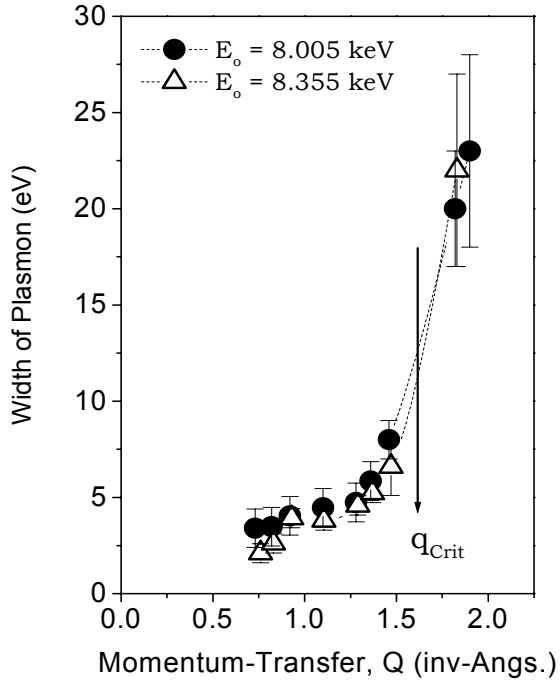

Figure 3.2.3 The width of plasmon excitations as a function of momentum transfer. Two different types of symbols represent data taken with different incident energies. The width increases dramatically as one crosses some critical value of momentum transfer.

3.3 Models of Collective Charge Excitations in Electron Gases

The collective charge excitations in an electron gas is well studied [5][17][21][29]. We consider the dielectric response of a gas within the random phase approximation (RPA) which replaces the actual electronic interaction with an average interaction due to all the electrons [2] :

$$\varepsilon^{-1}(\mathbf{q},\omega) \sim \varepsilon^{-1}{}_{RPA}(\mathbf{q},\omega),$$

$$\varepsilon_{RPA}(\mathbf{q},\omega) = \varepsilon_r(\mathbf{q},\omega) + i\,\varepsilon_i(\mathbf{q},\omega), \qquad (3.3.1)$$

The shape of the functions $\boldsymbol{\varepsilon_r}$ and $\boldsymbol{\varepsilon_i}$ will depend on the values of $\mathbf{q}$, below some $\mathbf{q}_{crit}$, $\boldsymbol{\varepsilon_r}$ goes through a zero and contributes most to the Im $(\varepsilon^{-1}(\mathbf{q},\omega))$. The frequency where the response peaks is the collective charge mode of the system known as the plasmon. This excitation is a stable mode only if

$$\varepsilon\,(\mathbf{q},\,\omega(\mathbf{q})) = 0 \qquad (3.3.2)$$

This condition also determines the dispersion relation of plasmons. For $\mathbf{q} < \mathbf{q}_{crit}$, the contribution of electron-hole pair is screened to a large extent and plasmon is a sharp excitation mode.

If , for $\mathbf{q} = \mathbf{q}_c$, the high-frequency edge of ε_i just touches the zero position of ε_r the plasmon excitation stops being an independent mode and becomes strongly damped. This condition defines the critical wave vector : $\mathbf{q}_{crit}$. For $\mathbf{q} > \mathbf{q}_{crit}$ no plasmon resonance can exist. The broad feature is enhanced near the minimum of ε_r . The RPA behavior of particle-hole excitations is summarized in Fig. 3.3.1.

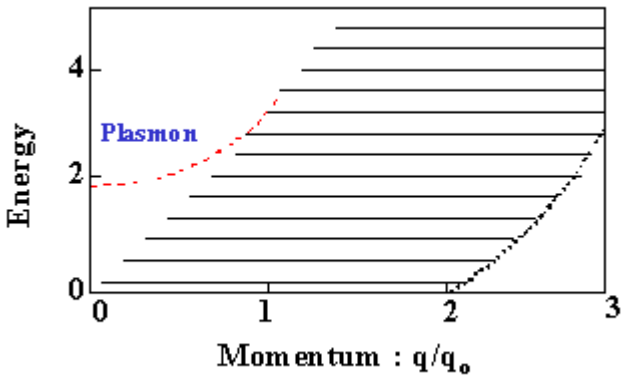

Figure 3.3.1 Momentum dependence of particle-hole excitations in a nearly free electron gas under random phase approximation (RPA) for r_s =4 [5]. At low momentum the collective mode (plasmon) is very stable and largely separated in energy from the single particle-hole pair continum. It then quadratically disperses upward in energy and eventually merges (damps out) into the free particle-hole pair continuum. Within RPA the width of the plasmon should be very sharp for low momenta. The width increases dramatically as one crosses somes critical value of momentum $\mathbf{q}_c$ (= $\omega_p{}^o/v_f$ where v_f is the Fermi velocity). [5].

The plasmon energy (ħ=1) at zero momentum transfer is

$$E(0) = \omega_p = (4\pi ne^2/\varepsilon m)^{1/2} \qquad (3.3.3)$$

where n is the electron density, e is the electron charge, ε is the dielectric constant and m is the electron mass. For momentum transfer $\mathbf{q} < \mathbf{q}_c$ RPA predicts a quadratic dispersion of plasmons :

$$\omega(q) = \omega(o) + (\alpha/m)\mathbf{q}^2 \qquad (3.3.3)$$

where α is a coefficient that depends only on the electron density. We draw the dispersion relation for plasmons ω(q) within RPA using α ~ 0.3 which is the estimated value for the

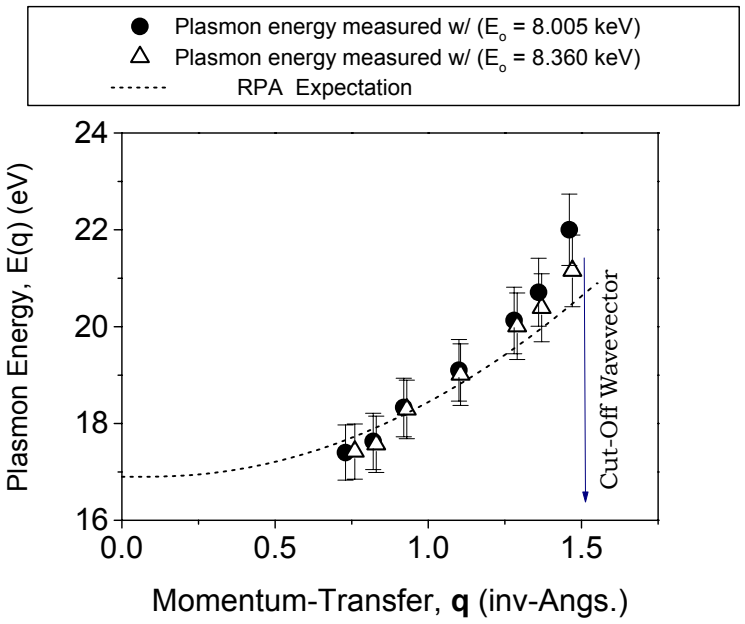

Figure 3.3.2 Plasmon dispersion compared with Random Phase Approximation (RPA). Plasmons measured with two different incident energies - one far away from absorption edge and another near an absorption edge. Dispersion (momentum dependence) is identical within the level of experimental resolution.

electron density in $NiAl_3$. The RPA dispersion curve goes through the experimentally measured dispersion within the level of experimental errors (Fig. 3.3.2). This suggest that the dispersion of plasmons in $NiAl_3$ is consistent with RPA even up to the critical wave vector although the data

points seem to show deviation toward high energies from RPA value for higher wave vectors (**q**'s). At large momentum transfers other interactions beyond RPA may need to be included such as effect of the periodic lattice (band structure) or electron-electron correlations. Experiment with better energy resolution would be necessary to further investigate the intrinsic origin of this deviation from RPA at high **q**'s.

As for the width, RPA predicts infinite lifetime or zero linewidth for **q** less than the cutoff momentum $\mathbf{q}_c$ ($\sim \omega_p^o/v_f$ where v_f is the Fermi velocity). At momenta above $\mathbf{q}_c$, the plasmon can decay into single electron-hole pairs and has a finite width. We do not see the evidence for a sharp cutoff, and the plasmon is not resolution limited even at $\mathbf{q} \sim 0$. One possibility is that RPA does not properly treat electron-electron interactions at large momentum transfers neither does it consider band-structure effects. Many authors have attempted to go beyond the RPA in the weakly interacting electron gas (jellium) model. The RPA with small corrections for the electronic interactions accurately predicts the dispersion of many other free-electron-like metals, such as Al, Na, and Be [35]. However, some metals such as Li (r_s ~3.27) have a measured dispersion significantly less than the RPA prediction [36]. In addition, EELS measurements of plasmons in the heavy alkali metals found the dispersion to be virtually flat in Rb (r_s ~5.2) and even negative in Cs (r_s ~5.62) [37][38]. For these values of r_s theoretical models that use a local field factor to go beyond the RPA predict a positive dispersion, although with a dispersion coefficient reduced from the RPA value. It has been unclear whether these disagreements are due to the insufficiencies in the present theoretical treatment of the electron gas or solid state effects (such as band structure). Measurements to determine the effect of band structure on the plasmon were carried out by Schülke and collaborators on single crystals of Li, Be, and Al [39][41]. However, these studies did not show much dependence when they measured the plasmon dispersion along different crystal directions below the cutoff wave vector (although structures at momentum transfers above the cutoff did depend strongly on the crystal orientation).

The purpose for this experiment on $NiAl_3$ has been to describe a simple model system as an example to describe the technique of inelastic x-ray scattering. We conclude that charge collective modes in $NiAl_3$ are quadratically dispersive and qualitatively consistent with RPA model. We now turn to a different aspect of the technique - the effect of core resonances (incident x-ray energies set near an absorption edge of the sample under study) in studying the valence excitations using inelastic x-ray scattering.

3.4 Plasmon Scattering near an X-ray Resonance

Since a lot of inelastic x-ray scattering studies of high-Z materials such as transition metal oxides are performed near an atomic core resonance to enhance the overall scattering cross-section it would be interesting to study the effects of working near a resonance (incident energy dependence) in a simple well-understood system. In this section we briefly discuss the dependence of incident x-ray energies on the scattering of plasmons near an absorption edge of

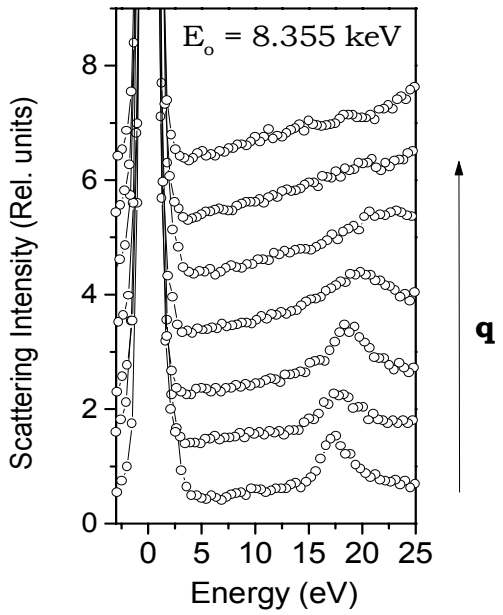

Figure 3.4.1 Momentum-transfer dependence of plasmons for incident x-ray energy near a core resonance (E_o = 8.355 keV). Within the level of experimental resolution dispersion of plasmon is found to be identical to that measured with incident energy far away from a resonance although the intensity of the plasmon is reduced.

the material. We measured **q**-dependence of plasmons near resonance (E_o = 8355 eV) as shown in Figure 3.4.1. Within the level of energy and momentum resolutions the dispersions look identical to that measured with incident x-ray energies far away from a resonance. A comparison is shown in Fig 3.4.2 (this is a similar result as in Fig. 3.2.2). The dispersions of plasmons are independent of the choice of incident energies as expected.

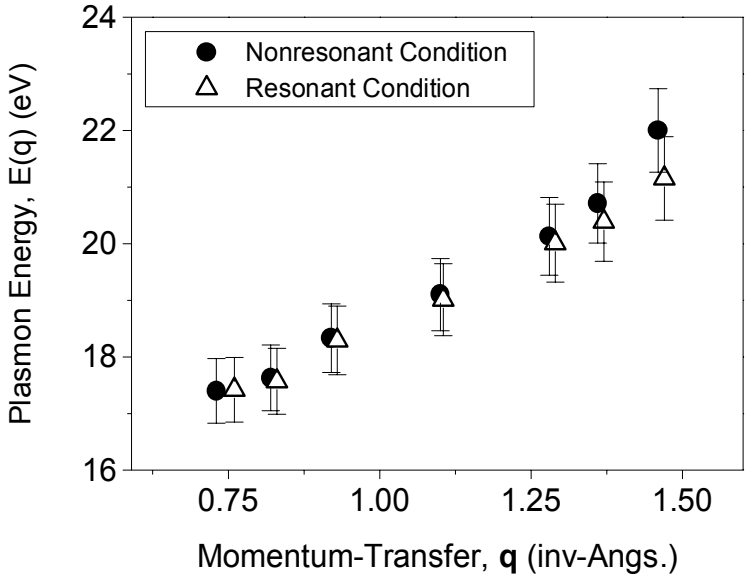

Figure 3.4.2 Dispersion of plasmons measured with two different incident energies - one far away from absorption edge and another near an absorption edge. Dispersion (momentum dependence) is identical within the level of experimental resolution. Nonresonant and resonant energies correspond to 8.005 keV and 8.355 keV.

The interesting fact about incident energy dependence is that the intrinsic plasmon scattering cross-section go through a dip near the core resonance. We measured the intensity of plasmons as a function of incident energy as we sweep across an absorption edge (Ni K-edge). This dependence is plotted in Figure 3.4.3. The square symbols represent the raw scattering intensity of plasmons normalized to the incident flux which decreases as the incident energy increases through the absorption edge. The decrease may have two factors contributing to it - one, reduction of effective scattering volume near an absorption edge two, drop in intrinsic cross-section for plasmon scattering. We can calculate the contribution of the first factor - reduction of effective scattering volume near an absorption and correct for it and then compare the scattering intensities intrinsic of plasmons as a function of energy. The analysis procedure is detailed in Appendix : A-2.

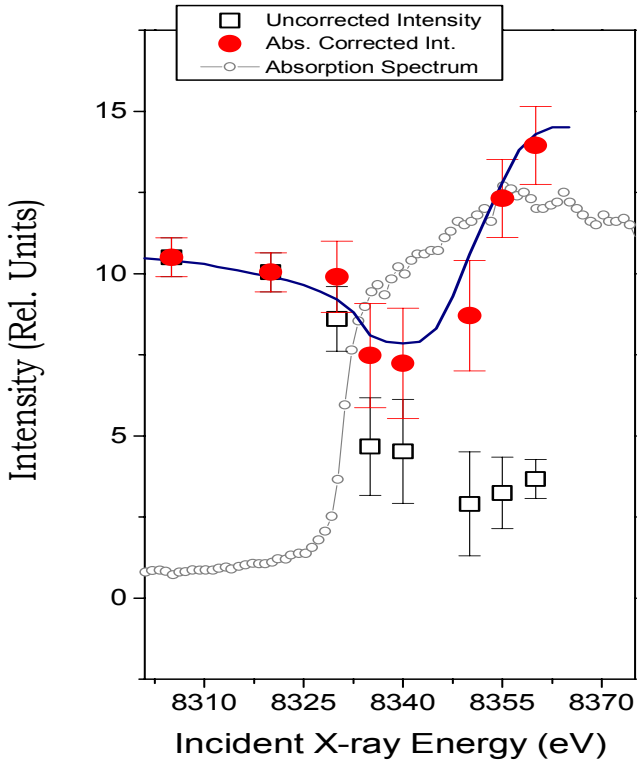

Figure 3.4.3 Incident energy dependence of plasmon scattering near an absorption edge (Ni K-edge) of the material. Open squares represent normalized scattering intensities of plasmons uncorrected for sample absorption. The filled circles represent normalized scattering intensities of plasmons corrected (compansated) for sample absorption. The intrinsic scattering of plasmon may go through a dip near a core resonance.

The filled circles in Figure 3.4.3 show the plasmon scattering intensities as a function of incident energy near an absorption edge of the sample. Now we notice that the intrinsic plasmon scattering intensity, which we call the resonance profile, tends to enhance as one goes past the absorption edge but the enhancement is not significant and there may be a dip right at the absorption edge. The shift of the enhancement further up in energy from the absorption edge is also observed in scattering from valence electrons in copper oxides. In case of transition metal oxides the nonresonant signal is very small and often hard to use to measure momentum dependence. Since in case of copper oxides the nonresonant signal is extremely weak (as we would see in chapter four and five) it is not possible to say whether there is a dip in the resonance profile or not. The

origin of this weak dip and weak enhancement is likely to be due to an intereference effect - the intereference between the nonresonant and resonant terms in the cross-section. A much better set of data with sufficient statistics is necessary to fit these results with a model describing such interference.

3.5 Conclusion

In case of the metallic $NiAl_3$ - a weakly interacting electron gas we found that the dominant contributor to density fluctuations was a volume plasmon. Plasmons are the zero-sound modes of a charged Fermi liquid but possess a mass even in the long-wave-length limit (small wave-vectors) due to the long-range nature of the Coulomb interactions. In case of weak interactions among electrons in the gas and at high number densities random phase approximation (RPA) works well to describe the excitation spectra below the critical wave vector. Under RPA, plasmon is stable and sharp at low momenta and increases in energy quadratically as a function of momentum until it hits the free particle-hole continuum as the phase velocity of plasmon becomes comparable to the fermi velocity of the electrons and gets damped (Landau damping). The experimental results are consistent with RPA expectations within the level of energy and momentum resolution. We have also seen a change in plasmon scattering near a core resonance of the material. The scattering profile shows a dip near resonance suggesting some sort of interference effect. More systematic studies of such an interference effect can potentially be used to extract phase information associated with electronic excitations. Our preliminary studies are inadequate for a detailed analysis at this point but the results are promising for a future pursuit.

Chapter 4

Charge Dynamics in Quasi-Two-Dimensional Mott Insulators

The discovery of high temperature superconductivity, colossal magnetoresistance and many other unusual electronic properties in transition metal oxides have led to the extensive research interests in these systems [43]-[48]. The parent compounds of such oxides are characterized by large onsite Coulomb interaction. As a consequence the low-temperature resistivity in these systems shows a large energy gap generally known as the Mott gap which is in contrast to the conventional one-electron band theory as that would predict these systems to be metallic [49]-[53]. Mott systems fall into the general class of interacting electron systems known as correlated electron systems where electron-electron correlation predominantly determines the properties of the system [54]-[56]. A Mott insulator is fundamentally different from a conventional band insulator or a semiconductor. In a band insulator, conductivity at low temperatures is blocked by the Pauli exclusion principle - when the highest occupied band contains two electrons per unit cell, electrons cannot move because all orbitals are filled. In a Mott insulator, charge conduction is blocked instead by direct electron-electron Coulomb repulsion. When the highest occupied band contains one electron per unit cell, electron motion requires creation of a doubly occupied site. If the electron-electron repulsion is strong enough, this motion is blocked [49]-[52]. The amount of charge per unit cell remains fixed and only the electron spin on each site can fluctuate. Such virtual charge fluctuations in a Mott insulator generate an effective magnetic interaction known as the superexchange interaction, which favors antiparallel alignment of neighboring spins in the absence of orbital degeneracy. In many materials, this leads to long-range antiferromagnetic order [49]-[52]. It is believed that the key to understand the unusual electronic and magnetic properties in many transition metal oxides such as non-Fermi-liquid behavior, psuedo- gapped metallic phase, high T_c superconductivity, charge-orbital striping, colossal magnetoresistance or giant optical nonlinearity is in the existence of a

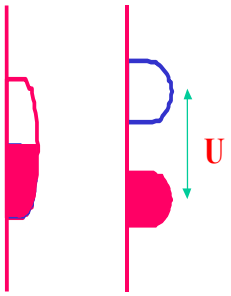

Figure 4.0.1 Strong local Coulomb interaction leads to a breakdown of conventional one-electron bandstructure and drives a system into an insulator which would otherwise be a simple metal. If the Coulomb interaction, U, is larger than the one-electron bandwidth a system shows an energy gap in the electronic excitation spectrum.

Mott state in their parent compounds [43]-[47]. This suggests the importance of a thorough study of the charge and spin dynamics of these systems.

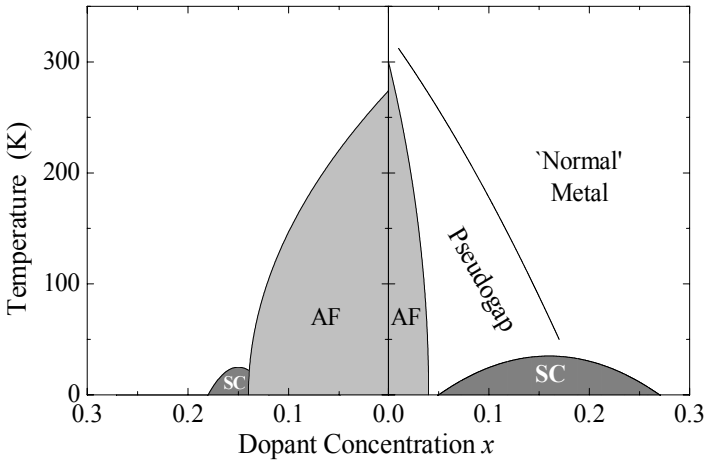

Figure 4.0.2 Phase diagram of copper oxides : Doped copper oxides exhibit variety of phases such as antiferromagnetism (AF), high temperature superconductivity (SC), Gapped metal (Pseudogap phase). The right side of the x ~ 0 line represents hole doped system where as the left represents doping with electrons. The x~ 0 antiferromagnetic phase is insulating at low temperatures which is believed to be a Mott insulator. High temperature superconductivity is seen in doped cuprate Mott insulators [45]-[47].

So far, inelastic neutron scattering has been extensively used to study the spin dynamics of these compounds [57]-[65]. As for the charge, momentum-resolved spectroscopies such as angle-resolved photoemission (ARPES) has been quite successful in characterizing the occupied electronic states of these oxides [66]-[73], whereas, electron-energy-loss spectroscopy (EELS) is limited to low momentum transfers and complicated due to multiple scattering [74] and inverse photoemission spectroscopy, on the other hand, is plagued with many technical difficulties [68]. A study of the momentum-resolved bulk electronic structure, especially for the excitations involving unoccupied electronic states and charge collective modes, is largely absent for these correlated insulators.

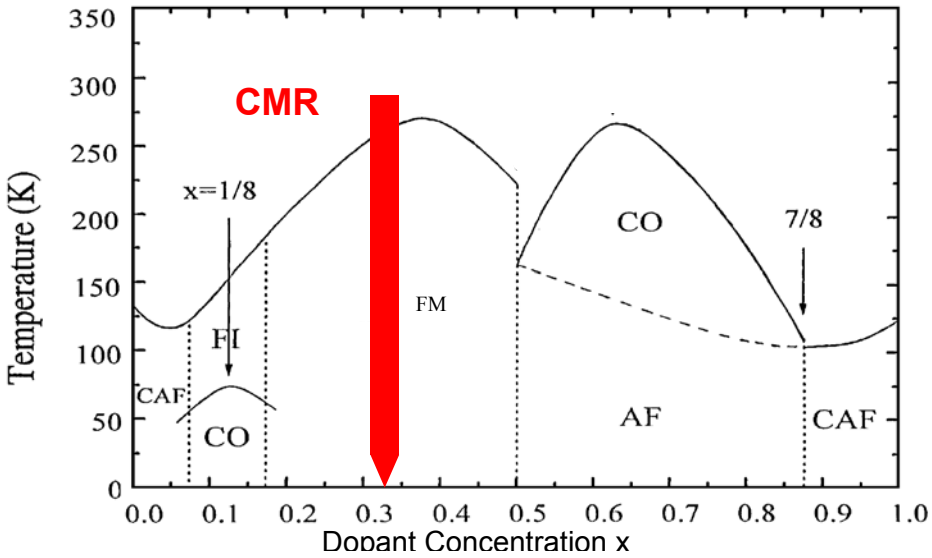

Figure 4.0.3 Manganese oxides exhibit many different phases as a function of doping. The $La_{1-x}Ca_xMnO_3$ system exhibits canted antiferromagnetism (CAF), charge ordered (CO) phase, ferromagnetic insulation (FI), ferromagnetic metallic (FM) [57]. Colossal Magnetoresistance (CMR) in this system is seen near x ~ 0.3 doping. The undoped manganite (x ~0) is a Mott insulator. CMR is found in doped manganite Mott insulators.

In this chapter, we would present a study of the full Mott gap and excitations across the gap in a parent compound of high temperature superconductors. The results reveal the anisotropic and highly momentum dependent nature of excitations across the Mott gap over the entire Brillouin zone for the first time [76].

4.1 Basic Electronic Configuration of Planar Cuprates

The basic electronic configuration of copper oxides are directly related to their crystal structure. The parent copper oxides are structurally lamellar - having one fundamental ingredient in common : the existence of two dimensional sheets of CuO_2. These sheets are separated by layers of other atoms. It is widely believed that superconductivity in these systems is primarily due to electronic processes occuring in the CuO_2 sheets [68]. A typical crystal structure is shown in Fig. 4.1.1. In this system, the CuO_2 sheets are separated by CaCl bilayers. We are primarily interested to look at the electronic excitations in the systems with momentum transfer within the Cu-O plane.

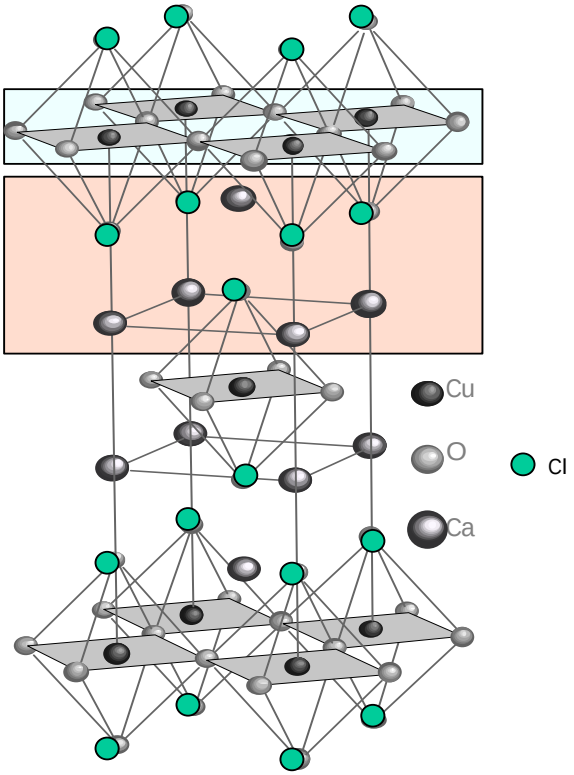

Figure 4.1.1 Crystal structure of $Ca_2Cu_2O_2Cl_2$ - a model parent compound of the high-temperature superconductors. The crucial structural subunit is the Cu-O_2 plane. Electronic couplings in the interplane (perpendicular) direction is very weak hence the system effectively behaves like quasi-two-dimensional.

The basic electronic configuration of the CuO_2 plane is shown in Fig. 4.1.2. The low energy physics of the CuO_2 plane mainly involves the hybridization of $3d(x^2-y^2)$ orbital of copper and $2p\sigma$ orbitals of oxygen. Due to the crystal field, d and p bands are not degenerate and they hybridize as shown in Fig. 4.1.2 (right). The resulting band structure would be metallic with the antibonding band being half filled (Fig. 4.1.3(A)). However because of the localized nature of d-orbitals and strong onsite Coulomb interaction the undoped system is actually a Mott insulator. The on-site Coulomb interaction splits the anti-bonding band into a filled lower Hubbard band and an empty upper Hubbard band (Fig 4.1.2(left))[43][45]. It also has an antiferromagnetic ground state due to the superexchange interaction between the neighboring spins (Fig 4.1.2(right))[43]. Because the nonbonding band which is largely of oxygen nature located in between the LHB and UHB the lowest excitation is not of the Hubbard type but charge transfer type [52]. The excitation is $d^9 \rightarrow d^8$ for LHB and charge transfer excitation has addition hopping from the nonbonding band to the LHB to lower the system energy. Thus the overall process is $d^9 \rightarrow d^9\ L^{-1}$ where L^{-1} represents a hole in the nonbonding band. The late transition metal oxides are such charge transfer insulators. When such systems are doped with holes the holes are believed to mainly occupy the oxygen site. The strong Cu-O hybridization binds a hole on each square of O atoms to the central Cu^{+2} ion to form a local singlet which is a coherent superposition of the $2p\sigma$ orbitals of the four nearest-neighbor oxygen atoms.

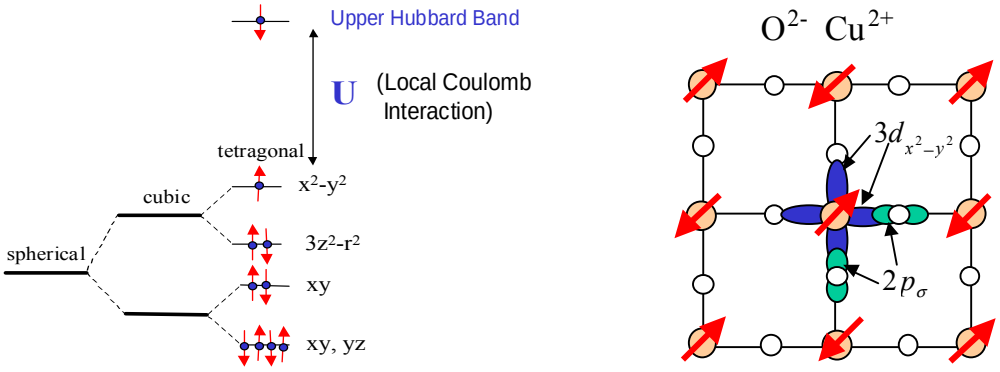

Figure 4.1.2 **(Left)** Electron distribution in Cu-3d orbitals. All the 3d orbitals are nondegenerate due to the tetragonal symmetry of crystal. The lowest binding energy electrons have the $d(x^2-y^2)$ character. The strong local Coulomb interaction leads to a breakdown of conventional one-electron bandstructure and splits the $d(x^2-y^2)$ levels. **(Right)** The low energy physics of the CuO_2 plane mainly involves the hybridization of $d(x^2-y^2)$ orbital of copper and $2p\sigma$ orbital of oxygen consistent with the local crystal structure.

This complex is known as the Zhang-Rice singlet. This singlet moves through the lattice in a similar way as the motion of a hole in the single band effective Hamiltonian in the strongly interacting limit of Hubbard model [77]. The momentum dependence of the single particle excitations (occupied electronic states) are described in Fig. 4.1.4.

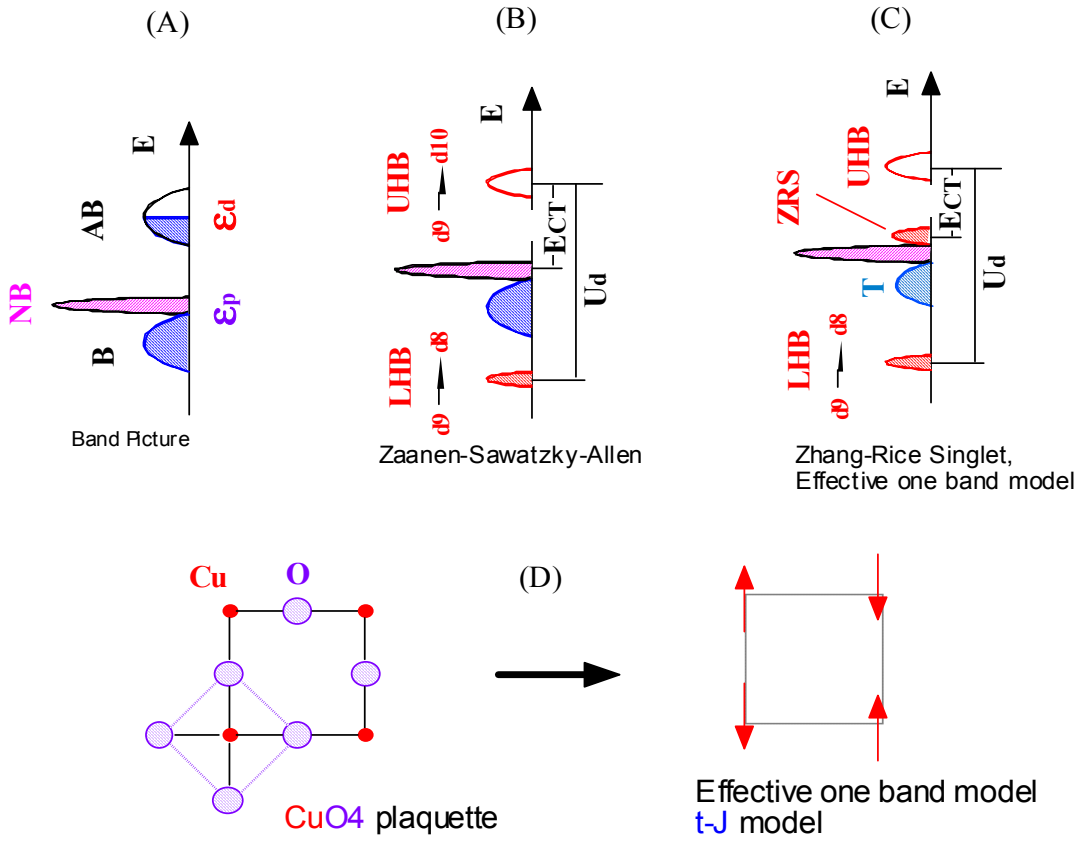

Figure 4.1.3 Schematic of electronic structure models of the CuO_2 plane : **(A)** Within one-electron band picture the antibonding band is half filled the the system would be a metal. **(B)** Inclusion of onsite Coulomb interaction splits the highest occupied band into lower and upper Hubbard bands. In this case the energy gap is set by the charge transfer from oxygen band to the upper Hubbard band known as the Zaanen-Sawatzky-Allen scheme **(C)** A hole in the CuO_2 plane is delocalizes on the oxygens surrounding a copper ion and hybridizes strongly with the Cu d orbital and forms a many-body state known as the Zharge-Rice singlet. **(D)** The low energy excitations can be modeled using two parameters - hopping of electrons from site to site described by t, and the magnetic interaction, J (~ $4t^2/U$), between the spins arising due to strong Coulomb interaction (U).

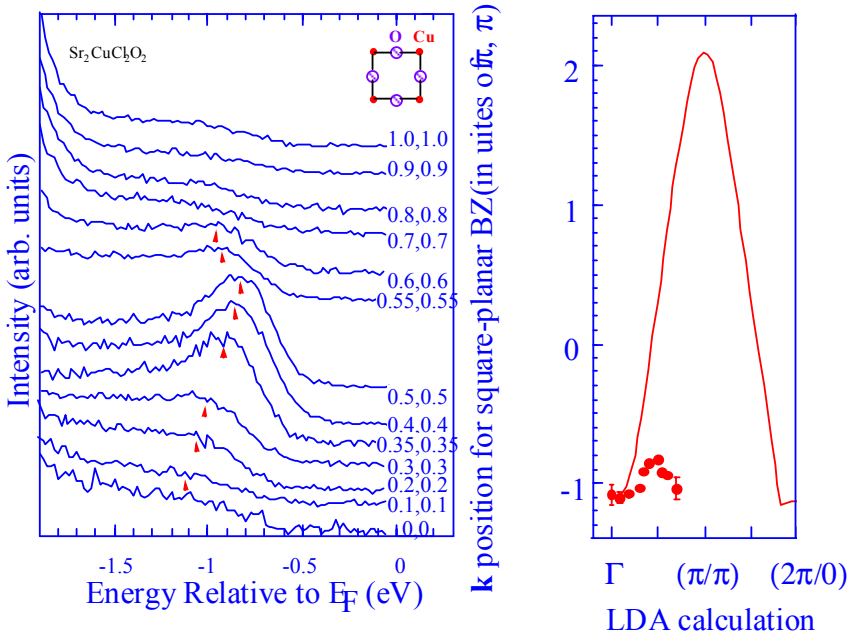

Figure 4.1.4 **(Left)** The momentum dependence of electronic states in $Sr_2CuO_2Cl_2$ along 45 degrees to the bond direction (Γ to (π,π)). The lowest energy state occurs for momentum (π/2, π/2). **(Right)** The dispersion of the band is much less than as it would be expected from an effective one-electron band model (LDA calculation : narrow line). The solid circles represent the measured data points. The measured dispersion is better described by a many-body model known as the t-J model (Fig. 4.1.3) [73].

4.2 Charge Dynamics and X-ray Scattering

In order to better understand the electronic structure of Mott systems, it is of significant importance to study the nature of the charge-excitation gap as it is the key signature of strong electron-electron correlation [47]. Angle-resolved photoemission which probes the occupied electronic states has been remarkably successful in characterizing the electronic structure of high temperature superconductors and related compounds [66]-[70]. There has not been any weak-coupling probe with deep bulk sensitivity providing information about momentum-resolved electronic structure for condensed-matter systems in general so far. The other electron based spectroscopies, besides photoemission, such as electron-energy-loss spectroscopies (EELS)

require extensive sample preparation (similar to the requirements faced by ARPES) and need to be corrected for multiple scattering effects because of its strong coupling nature [19]-[74]. So any deeply bulk and multiple-scattering-free (weak-coupling) study of the electronic structure is absent. We have carried out direct bulk measurement of cuprate electronic structure upto 9 eV energy-losses along high symmetry directions over a large part of the Brillouin zones. These results reveal the anisotropy of charge-excitations across the full gap. Particle-hole excitations are fundamental to understand the transport phenomena in general so it is of significant importance to use two-particle spectroscopies (besides single-particle spectroscopies) in a momentum-resolved mode so that nonlocal and anisotropic information about the interaction potentials can be obtained which determine various groundstates a correlated system can exist in.

The observation of a d-like dispersion of the insulating gap in $Ca_2CuO_2Cl_2$ in the momentum dependent study of the low-energy occupied states using ARPES and its possible relation to the pseudogap observed in the doped copper oxides may shed light in understanding the multiplicity of energy scales in the physics of high T_c superconductivity [71]. It would be interesting in this light to study the momentum dependence of the full Mott gap. When extended to doped system the closing of Mott gap can be studied to learn about the changes in the electronic structure that drives the system into a superconductor near $x \sim 0.65$ doping. With this view in mind we have studied the momentum dependence of the full Mott gap in the prototype 2-D Mott insulator $Ca_2CuO_2Cl_2$. X-ray scattering studies span the full Brillouin zone and provides symmetry selectively because of accessibility of core resonances and polarization dependence of the scattering factor [10][24]-[26].

4.3 Experimental Conditions

In recent times, it has been demonstrated by several groups that the inelastic x-ray scattering can be a good probe of electronic excitations in condensed matter systems because of its fairly wide kinematic range and direct coupling to the electron charge [6]-[21]. However, since x rays are highly absorbed in high-Z materials, applications of the technique have been mostly limited to low-*Z* systems [12]-[21]. Several recent studies, both experimental results and

theoretical/numerical investigations [9]-[10][25][26][78][79] have shown that by tuning the incident energy near an x-ray absorption edge a Raman-like effect could be measured with nonzero momentum transfer, despite the high absorption cross-section, through the large resonant enhancement which eventually dominates the overall cross-section. These studies have characterized the use, though not very straightforward, of this technique well. The observation of a low-energy charge-transfer gap has been reported recently with nonzero-q in a parent cuprate $Sr_2CuO_2Cl_2$ using resonant inelastic x-ray scattering (RIXS) [10] and has extensively been studied by optical spectroscopies (with q ~ 0 momentum transfer) [80]. The excitation band seen near 2 eV in optical spectroscopies is also seen in electron-energy-loss spectroscopy [74]. No q-resolved study covering the high momentum transfer regime has been reported along high symmetry directions like having q along the Cu-O bond directions (<100>) and 45 degrees to the bond-direction (<110>) to our knowledge. We chose to work with lower absorption and better single-crystal quality material $Ca_2CuO_2Cl_2$ and studied the excitations along <110> and <100> directions. $Ca_2CuO_2Cl_2$ has a better spectral property compared to $Sr_2CuO_2Cl_2$ [71] and the samples for this experiment are of the same growth batch used for ARPES experiments which exhibited best spectral quality (sharper band features).

Experiments were performed at the X-21 wiggler beamline [81] at the National Synchrotron Light Source (located at the Brookhaven National Laboratory) with an overall energy resolution of 440 meV determined by fitting the elastic scattering away from the Bragg condition on the sample. The best resolution achieved (with reasonable count rates) with this analyzer at the X-21 beamline near Cu K-edge was about 390 meV (Fig.4.3.2). Typical inelastic count rates from the sample were 20 to 30 counts per minute at energy losses of several electron volts around 250 mA ring current. The scattered light was analyzed by a spherically bent, diced crystal Ge(733) analyzer and focused onto an x-ray detector (a Rowland Circle focusing geometry). A large component of the incident polarization vector was in the plane of the Rowland Circle. Energy analysis was done by rotating the analyzer and translating the detector accordingly at the focus of the analyzer.

The momentum transfer (q) was scanned by rotating the entire apparatus around the center of the spectrometer. Incident energy was kept fixed near the Cu K-edge (E_0 = 8.996 KeV) determined from the flourescence profile. Several energies near the edge were checked for best resonant enhancements of prominent loss features to set the incident energy. The background was measured by keeping track of scattering intensities on the energy gain side (several eV on the

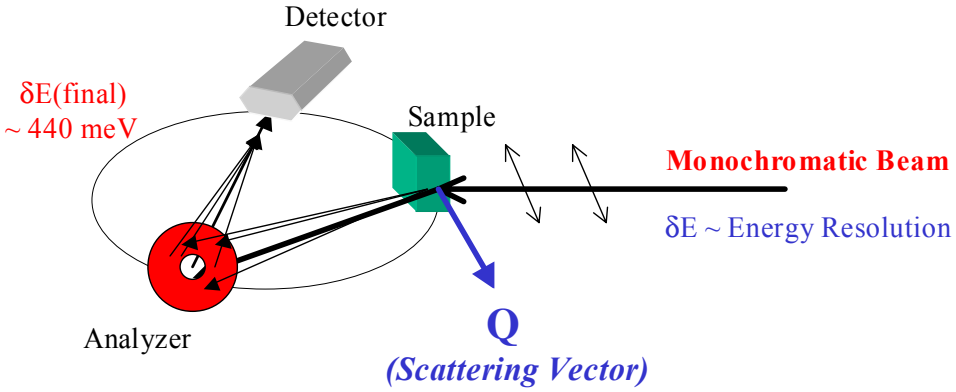

Figure 4.3.1 A schematic showing the scattering geometry for the experiment. In this arrangement incident polarization had a nonvanishing component along the direction of momentum transfer. The scattered beam collected by an energy analyzer (Ge(733)) then focused on a solid state detector.

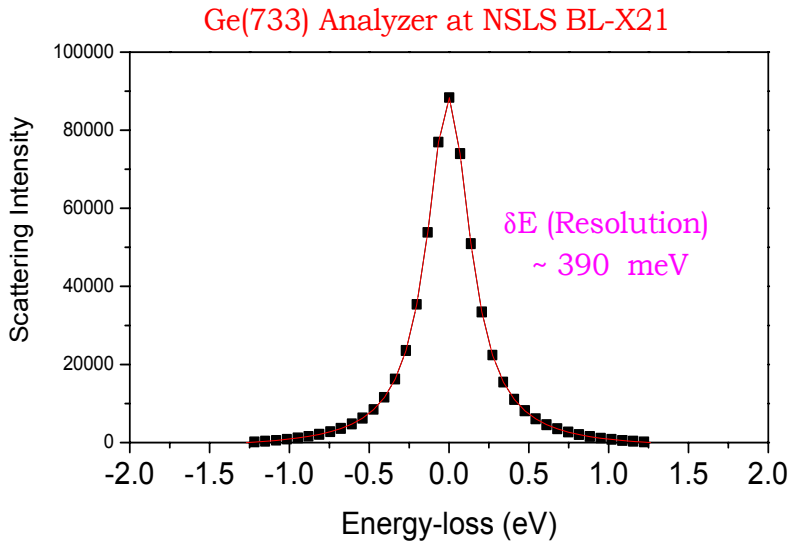

Figure 4.3.2 Resolution scan based on an amorphous scatterer (plastic sample) using Ge(733) analyzer at NSLS BL-X-21 at Brookhaven National Lab. To work near Cu K-edge with about 10 counts/min in the 2-6 eV energy-loss region from copper oxides it was possible to get down to 390 meV overall energy resolution.

energy gain spectrum) which was about 1-2 counts per minute. The detector was sufficiently shielded by a funnel made of thick lead tapes so as to block away any stray scattering entering into it. The $Ca_2CuO_2Cl_2$ crystals were grown and characterized by techniques described elsewhere [82]. Due to its extreme hygroscopic nature the crystal used for the experiment was always kept and prepared and preoriented for the mount under dry N_2 and chemical desiccant environments and the experiment was perfomed in a 3-scale (10^{-3} Torr) vacuum system with transparent capton windows for the entrance and the exit of the x-ray beam. Beamline (NSLS x21) characteristics and the standard experimental set-up used are further detailed elsewhere [81].

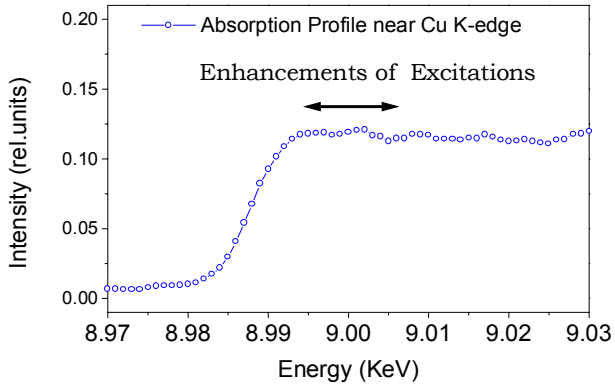

Figure 4.3.3. Absorption spectrum near Cu K-edge. The enhancements of inelastic excitations were seen several electron volts past the absorption edge. The double edge arrow marks the energy region near the absorption edge where incident x-ray energies were used for the experiment.

4.4 Excitation Spectra in Planar Cuprates

Fig. 4.4.1 shows inelastic x-ray scattering spectra near Cu K-edge from parent cuprate $Ca_2CuO_2Cl_2$ with varying momentum transfers along <110> (45 degrees to the Cu-O bond direction) and Fig. 4.4.2 shows spectra with momentum transfers along <100> (the bond direction). All the spectra in each panel were normalized near 8 eV energy-loss so the intensities reported here are only relative. Each spectrum exhibits two features – one broad hump around 5.8 eV and a weak feature around 2.5 to 3.8 eV for different q-values. The broad feature centered around 5.8 eV, reported earlier along different directions <001> and <210> ([10][25]) changes

shape with change of q (also polarization) but does not show any significant dispersion (compared to its width) in either <100> or <110> directions in our measurements (there is no earlier report of its q-dependent measurement along <100> and <110> directions) thus establishing on rigorous grounds that it has a highly local character. Based on electronic structure calculations the 5.8-eV feature is believed to be a charge transfer excitation from mostly nonbonding oxygen-like orbitals to the unoccupied copper d-like orbitals with antibonding character ([25][83]). The lower energy feature, on the other hand, has a significant movement in changing q from (0,0) (measured near (2π,2π) because of kinematic limitations) to (π,π) as seen in Fig. 4.4.1. The feature clearly appears near (π/4,π/4) then disperses upward about 1.35 eV monotonically in this direction. Where as if the momentum transfer is along (0,0) (measured at (2π,0)) to (π, 0), it is not clearly visible in the raw data but if we believe the hump of spectral

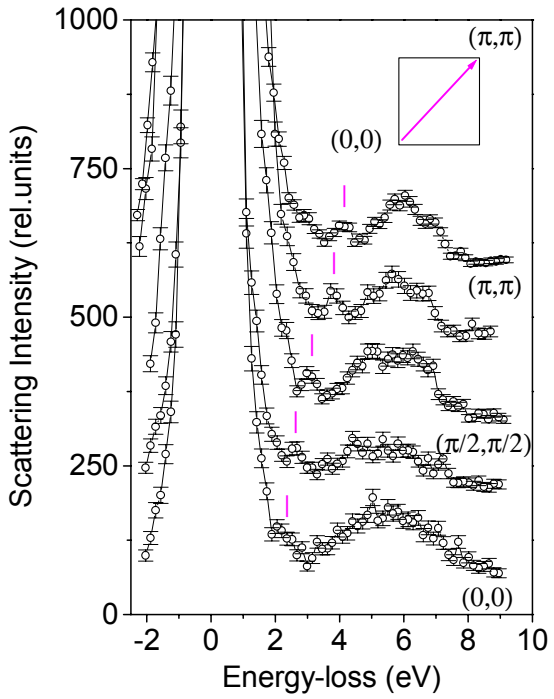

Figure 4.4.1 Momentum (**q**-) dependence of inelastic x-ray scattering spectra near Cu K-edge along the <110>-direction from equivalent-(0,0) to (π,π) in $Ca_2CuO_2Cl_2$. Incident photon energy E_o = 8.996 eV. The pointers (|) are used to indicate the positions of the low-energy inelastic features.

weight near the tail of the elastic peak to indicate the low-energy feature's presence (there is no such intensity-hump on the other side of the elastic peak) it can be seen that it does not show much dispersion in going from (0,0) to (π/2, 0) and perhaps appears slightly lower in energy-loss

near (π/2,0). But it seems to appear as q is past (π/2,0) and near (3π/4,0). In going from (π/2, 0) to (π, 0) it disperses again upward by about 0.5 eV. Not all the spectra were taken in the same Brillouin zone (q-space) because of various kinematic limitations, beam spot size contributions to the cross-section, resolution issues or to avoid a near-Bragg large quasi-elastic scattering tail. Appendix-A-3 shows the actual momentum transfers and their equivalent zone co-ordinates determined by the lattice symmetries.

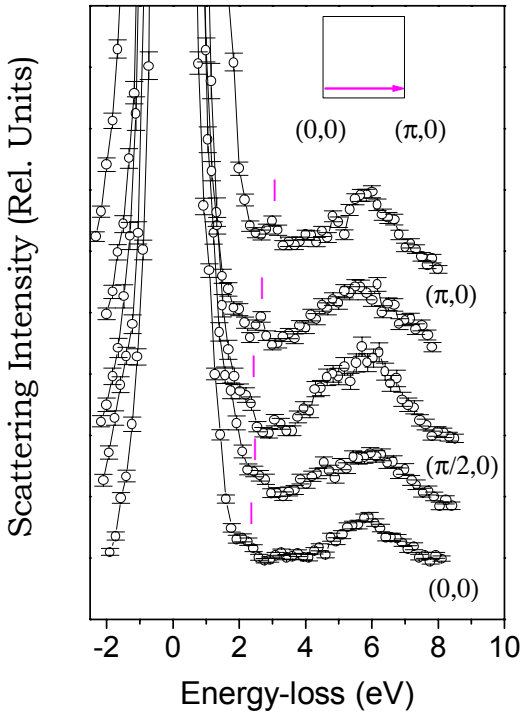

Figure 4.4.2 Momentum (**q**-) dependence of inelastic x-ray scattering spectra near Cu K-edge along the <100>-direction from equivalent-(0,0) to (π,0) in $Ca_2CuO_2Cl_2$. Incident photon energy E_o = 8.996 eV. The pointers (|) are used to indicate the positions of the low-energy inelastic features.

A closer observation at the spectra taken near q = (π,π) reveals that there might be some additional spectral weight near 2.8 eV energy-loss, hence a possibility of another even lower energy feature. In order to make a more reliable estimate on the q-dependence and such weaker features, we fit and subtract out the zero energy loss peaks (quasi-elastic scattering) using a combination of Gaussian and asymmetric Lorentzian functions. Because of large fluctuations in 0-1 eV region within the elastic peak arising from the subtraction of two large numbers (data and the fit) we can not extract any useful information about the electronic structure hence keep the 0-1

eV energy-loss region blank and focus our attention on features arising above 1 eV only. The very fact that we can identify most of the principal features of the spectra in the raw data has motivated us to do the background subtraction and look at the low-energy features. Now we can clearly see the dispersive behavior of the low-energy excitations in Fig. 4.4.3(A) having q along <110> and Fig. 4.4.3(B) along <100>.

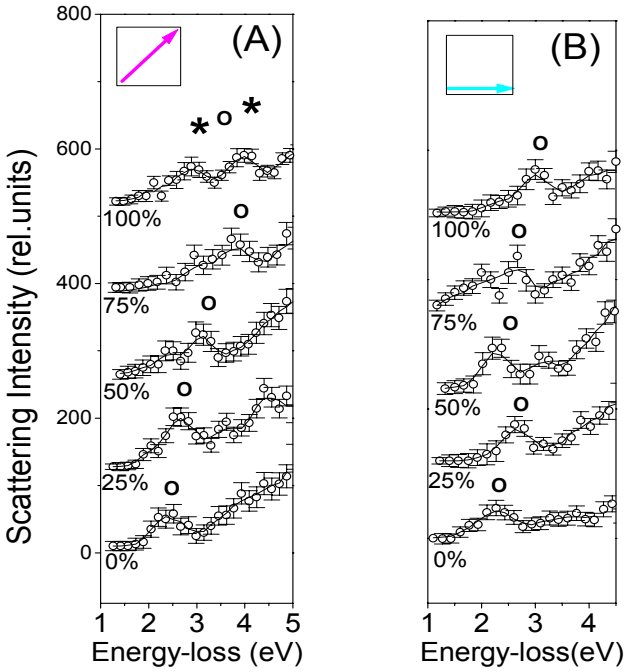

Figure 4.4.3 Momentum dependence of the lower energy inelastic feature for q || <110> in figure (A) and q || <100> in figure (B). Background due to quasielastic has been removed. The center of gravity of spectral weights are indicated by the open circles The percent numbers show the normalized q co-ordinates (locations inside the Brillouin zone) and the inset in each panel shows the direction of the scattering wave vector (momentum transfer).

After the elastic subtraction our conclusions from the raw data do not change in a qualitative manner. The only new feature that reveals itself with some statistical significance is on the q =(π,π) spectrum as suspected from the raw data. In addition to the 3.8 eV feature there seems to be another lower energy feature around 2.9 eV [Fig. 4.4.3(A), topmost spectrum].

We make estimates on the center of gravity of the low-energy feature's spectral weights after subtracting the 'background' due to the high energy feature centered around 5.8 eV by extrapolating its tail to low energies. We plot these extracted excitation energies in Fig. 4.4.4 as

functions of q and Fig. 4.4.5 shows a 4-fold symmetrized q-space map of the charge-excitations across the effective Mott-gap, constructed based on the data, revealing its q-space symmetry.

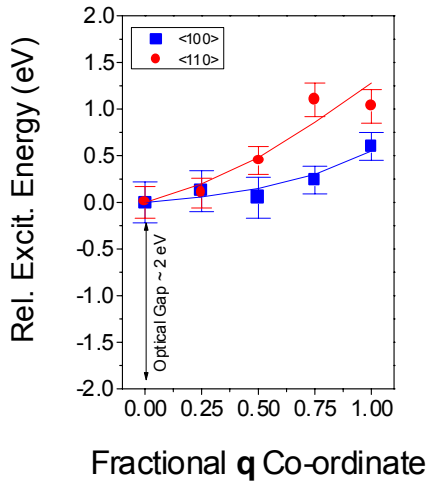

Figure 4.4.4 Momentum dependence of the center of gravity of the low-energy inelastic feature in $Ca_2CuO_2Cl_2$. Relative excitation energies are plotted referenced to the energy (E_o) at q = (0,0) along each direction [101].

We interpret the low-energy feature in the data as the observation of q-resolved excitations across the effective Mott-gap (Fig. 4.4.6). The RIXS process shakes up the valence electron system and creates a particle-hole pair across or below the gap which carries energy and momentum. This pair propagates in a background of antiferromagnetically ordered lattice. In a local picture, the created hole forms a Zhang-Rice singlet and an electron is excited onto the neighboring Cu site (at the upper Hubbard band). Fig. 4.4.7 shows a schematic of a particle-hole pair excitation in the CuO_2 plane (the arrows denote the spins of holes). Antiferromagnetic correlation of the system plays a key role in determining the anisotropic propagation (dispersion) of the particle-hole excitations. In an attempt to understand the observed dispersions, we note that in the absence of strong electron-electron correlation such as in case of the band insulators (or semiconductors) a convolution of the 'valence band' and the 'conduction band' is sufficient to understand their RIXS

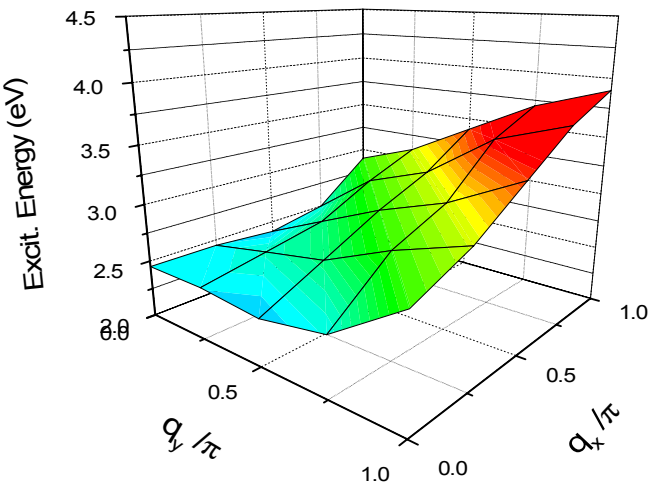

Figure 4.4.5 A q-space map of charge excitations across the Mott gap summarizing the overall dispersion behavior is summarized in this figure. The shade in this figure recodes the energy axis to create a clear visual representation for the shape of the dispersion surface.

spectra whereas for a Mott insulator such an approach is not sufficient because the gap does not originate from band effects but rather from the strong correlation effects so the particle-hole excitations of the Mott system can not be treated as independent excitations of single-particle states. Higher-order correlation functions (e.g., Second-Order Green's function) are necessary to

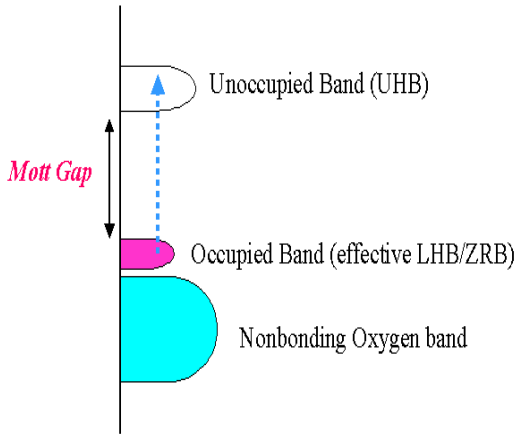

Figure 4.4.6 A schematic of (k-integrated) electronic structure of the parent copper oxide insulator which shows a charge gap between the effective occupied Zhang-Rice band and the unoccupied upper Hubbard band. It is to keep in mind that Mott excitation is really a many-body excitation more than this cartoon represents.

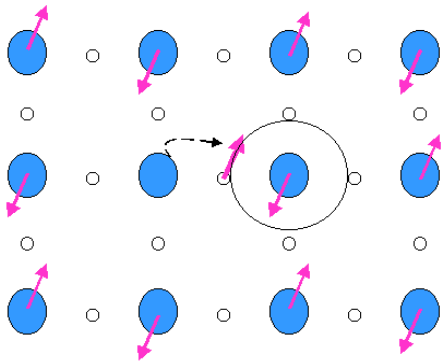

Figure 4.4.7 A schematic of particle-hole pair excitations in a CuO_2 square lattice with long-range antiferromagnetic order. The arrows denote the spins of holes. The filled blue and empty white circles denote Cu-sites and O-sites respectively. The blue empty site in the middle is the electron (particle) and the big complex containing four oxygen sites is the Zhang-Rice singlet (hole). The experimental results reveal that the propagation of particle-hole excitations are strongly anisotropic in this antiferromagnetically ordered lattice [76].

interpret RIXS spectra, so, in this sense, RIXS would provide more information than combined ARPES and IARPES.

We note that the center of gravity of the low energy feature we interpreted as a Mott excitation (excitation across the Mott gap) appears somewhat higher in energy compared to the feature seen in optical experiments (~2 eV) [80]. In optical experiments, the gap is defined to be the onset of predominantly dipolar excitation which is about 1.8 eV in case of $Sr_2CuO_2Cl_2$. In case of x-ray scattering one picks up cross-section from both dipolar and non-dipolar excitations hence it is not unlikely that the line shape of the Mott feature would be different from edge-like feature seen in optics. We believe that center of gravity of the Mott feature in our experiment apearing at higher energies for q ~ 0 is due to nondipolar contributions to the excitations that make up the feature. Where as the spectroscopic definition (there is no reason to define the gap as onset of dipolar excitations as in optics) of the gap is somewhat arbitrary considering the large error bars in the x-ray or electron scattering case a precise comparison with optics is difficult. This view is also consistent in connection with EELS results for low-q's where the center of gravity of the Mott

feature is around 2.6 eV and we know that EELS spectrum contains both dipolar and nondipolar contributions [74].

A model based rigorous calculation is necessary to elucidate the origin and nature of the q-resolved charge excitations in a strongly correlated quantum system. In the next section we present calculations of RIXS spectra in a Mott insulator within the framework of Hubbard model and compare with our experimental results.

4.5 Hubbard Model and Charge Excitations

We consider the extended Hubbard model with long-range hoppings, where the lower Hubbard band (LHB) is regarded as the Zhang-Rice band. The Hamiltonian is given by [78]

$$H_{3d}=-t\Sigma_{i,\sigma}(d_{i,\sigma}^{\dagger}d_{j,\sigma}+\text{h.c.})-t'\Sigma_{i,\sigma}(d_{i,\sigma}^{\dagger}d_{j,\sigma}+\text{h.c.})-t''\Sigma_{i,\sigma}(d_{i,\sigma}^{\dagger}d_{j,\sigma}+\text{h.c.})+U\Sigma_i n_{i,\uparrow}^{d}n_{i,\downarrow}^{d}$$

where $d_{i,\sigma}^{\dagger}$ is the creation operator of 3*d* electron with spin σ at site i, $n_{i,\sigma}^{d} = d_{i,\sigma}^{\dagger}d_{i,\sigma}$, and $n_i^{d} = n_{i,\uparrow}^{d} + n_{i,\downarrow}^{d}$. The on-site Coulomb energy U corresponds to the charge transfer energy of cuprates. The values of the parameters are set to be t = 0.35 eV, U/t = 10, t'/t = –0.34, and t''/t = 0.23 [73][78].

In the intermediate states of Cu *K*-edge resonant inelastic x-ray scattering (RIXS) process, 3*d* electrons interact with a 1*s* core hole created by the dipole transition of a 1*s* electron to 4*p* orbital due to an absorption of an incident photon with energy ω_i and momentum K_i. This interaction is written as

$$H_{1s\text{-}3d} = -V_c\Sigma_{i,\sigma,\sigma'}n_{i,\sigma}^{d}\,n_{i,\sigma'}^{s},$$

where $n_{i,\sigma}^{s}$ is the number operator of 1*s* core hole with spin σ at site i, and V_c is taken to be positive. This interaction causes excitations of the 3*d* electrons across the gap. The photo-excited 4*p* electron is assumed to go into the bottom of the 4*p* band with momentum k_0 and not to interact with either the 3*d* electrons or the 1*s* core hole due to delocalized nature of the 4p bands.

In the final state, the 4*p* electron goes back to the 1*s* orbital emitting an "off-energy shell" photon with energy ω_f and momentum K_f. The RIXS spectrum is then given by [78][79] :

$$I(q,\Delta\omega) = \Sigma_\alpha |<\alpha|\Sigma_\sigma s_{k0-Kf,\sigma} p_{k0,\sigma} (H+\varepsilon_{1s\text{-}4p}-E_0-\omega_i-i\Gamma)^{-1} p_{k0,\sigma}^\dagger s_{k0-Ki,\sigma}^\dagger |0>|^2 \delta(\Delta\omega-E_\alpha+E_0),$$

where $H = H_{3d} + H_{1s\text{-}3d}$, $q = K_i - K_f$, $\Delta\omega = \omega_i - \omega_f$, $s_{k,\sigma}^\dagger$ ($p_{k,\sigma}^\dagger$) is the creation operator of the 1*s* core hole (4*p* electron) with momentum k and spin σ, $|0>$ is the ground state of the half-filled system with energy E_0, $|\alpha>$ is the final state of the RIXS process with energy E_α, Γ is the inverse of the relaxation time in the intermediate state, and $\varepsilon_{1s\text{-}4p}$ is the energy difference between the 1*s* level and the bottom of the $4p_z$ band. The values of the parameters are set to be $V_c/t = 15$ and $\Gamma/t = 1$.

One can also calculate the single-particle excitation spectra for this model. Figure 4.5.1 shows the single-particle excitation spectrum $A(k,\omega)$ obtained by using the numerically exact diagonalization techniques on the 4x4 site cluster of the half-filled Hubbard model with *t'* and *t"* terms. Below the chemical potential set to be the energy zero in Fig. 4.5.1, a sharp peak appears at $(\pi/2,\pi/2)$ with the lowest-binding energy. The spectrum at $(\pi,0)$ is broad and deep in energy. These features are consistent with the ARPES data [73]. Above the chemical potential, the dispersion of UHB has the minimum of the energy at $(\pi,0)$. Due to the *t'* and *t"* terms the UHB and the LHB are not symmetric, that is, the particle-hole symmetry is broken. Thick lines are the functions $\pm 0.55J(\cos k_x+\cos k_y)^2 - 4t'_{\text{eff}}\cos k_x \cos k_y - 2t''_{\text{eff}}(\cos 2k_x+\cos 2k_y)$ for the LHB (–) and the UHB (+) for a guide to eyes, where $J = 4t^2/U$. These functions are the effective dispersion relations for the single-particle excitations in the undoped Hubbard model.

Figure 4.5.2 shows the RIXS spectra calculated on a 4x4-site cluster [73][78]. Along the <110> direction, the energy position of the centroid of the spectrum increases monotonically with increasing $|\Delta K|$, being consistent with the low energy feature of the experimental spectrum. If the excitation across the charge gap were interpreted as the convolution of the single-particle excitation spectra, the spectrum at $q = (\pi/2,\pi/2)$ should have the lowest energy excitation, that is, the excitation from the $(\pi/2,-\pi/2)$ state in the top of the occupied LHB to the $(\pi,0)$ state of the bottom of the UHB should be the lowest in energy. However, we find that by calculating the spectral function of the two-body Green's function, which is the propagator of the state after the creations of a hole at $(\pi/2,-\pi/2)$ and an electron at $(\pi,0)$ in the ground state, this process is almost

forbidden. The RIXS spectrum at (π/2,π/2) in Fig. 4.5.2, therefore, involves excitations of some other processes

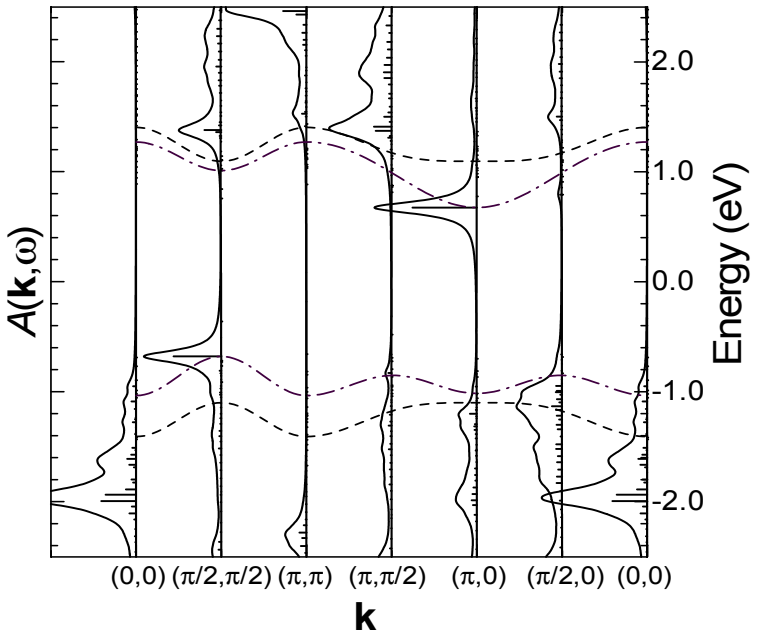

Figure 4.5.1 Single-particle excitation spectrum in the t-t'-t"-U-V model. The values of the parameters are t = 0.35 eV, U/t = 10, V/t = 1, t'/t = -0.34, and t''/t = 0.23. The dot-dashed lines are the functions $\pm 0.55J(\cos k_x+\cos k_y)^2 - 4t'_{\text{eff}}\cos k_x \cos k_y - 2t''_{\text{eff}}(\cos 2k_x+\cos 2k_y)$ for the LHB and the UHB, where $J = 4t^2/U$ and $t'_{\text{eff}}/t' = t''_{\text{eff}}/t'' = 0.3$, for the guide to eyes. The dashed lines are schematic dispersions fitted by the functions $\pm 0.55J(\cos k_x+\cos k_y)^2$ for the t-U-V model.

keeping the momentum transfer of (π/2,π/2), for example, the excitation from the occupied (π/2,0) state to the unoccupied (π,π/2) state. The spectrum at q = (π,π) has two structures: One is the peak at 3.1 eV and the other is higher-energy broad structure above 3.4 eV. The former is due to strong 'excitonic' effect enhanced by V. For comparison, the spectrum in the absence of V is shown as the dotted line in Fig. 4.5.2.

For a direct comparison between experiment and theory, we plot in Fig. 4.5.3 the momentum dependence of the low energy inelastic feature. Along the <110> direction, the energy position of the features increases monotonically with increasing q. In contrast to the <110> direction, the spectral threshold along the <100> direction decreases in energy from q = (0,0) to (π/2,0), and then increases toward q = (π,0). These features are overall consistent with the low energy

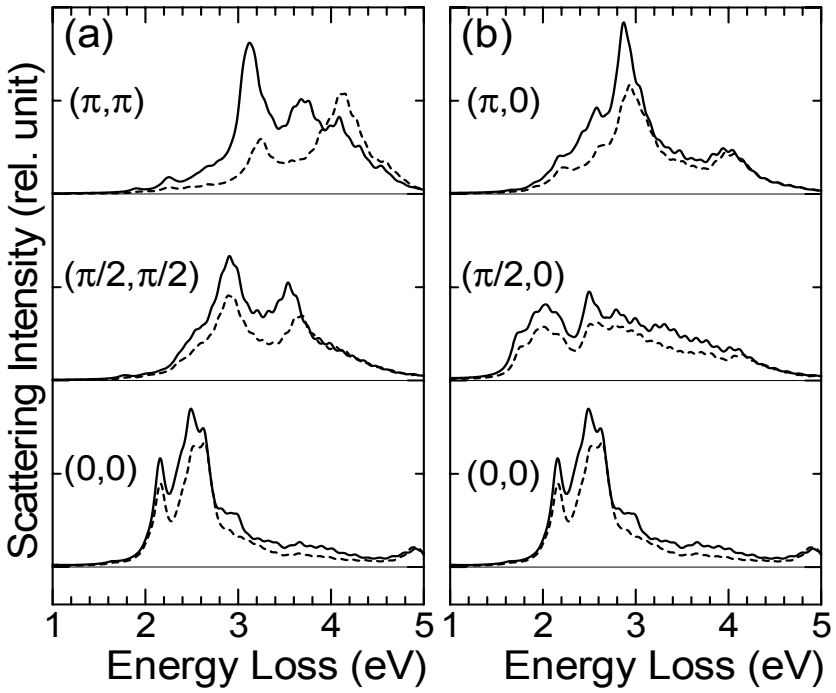

Figure 4.5.2 Momentum dipendence of the calculated RIXS spectra along (a) <110> and (b) <100> directions. The parameter values are t = 0.35 eV, U/t = 10, V/t = 1, t'/t = -0.34, and t''/t = 0.23, and V_c/t = 15. The dashed lines are in the case of the absence of intersite coupling V [78].

features of the experimental spectra (Fig. 4.5.3(A) and (B)). For more quantitative comparison between experiment and model, we plot in the momentum dependence of the center of gravity of the experimental and numerical results (Fig. 4.5.4). For for the dispersion plots, we first make estimates on the center of gravity of low-energy feature's spectral weights for the experimental data after subtracting the 'background' due to the high energy feature centered around 5.8 eV by extrapolating its tail to low energies. Along the <110> direction, the overall trend of the center of gravity is similar between the experiment and the model. For the q =(π,π) spectrum we plot two centers of gravity due to two separable low-energy features [Fig. 4.5.3(A) top spectrum]. We note that the theory curve at q=(π,π) also contains two features that are most separated in energy [Fig. 4.5.3(C), top spectrum]. The lower energy peak near 2.8 eV in the 'doublet' seen for q =(π,π) spectrum [Fig. 4.5.3(A), top spectrum] is likely to be of strongly excitonic origin due to intersite coupling. Along the <100> direction, the correspondence of the centers of the gravity between

experiment and theory is reasonably good. The flatness in energy dispersion from q = (0,0) to (π/2,0) [Fig. 4.5.4(B)] is likely to be due to the fact that in t-t'-t''-U model, that is, in the presence

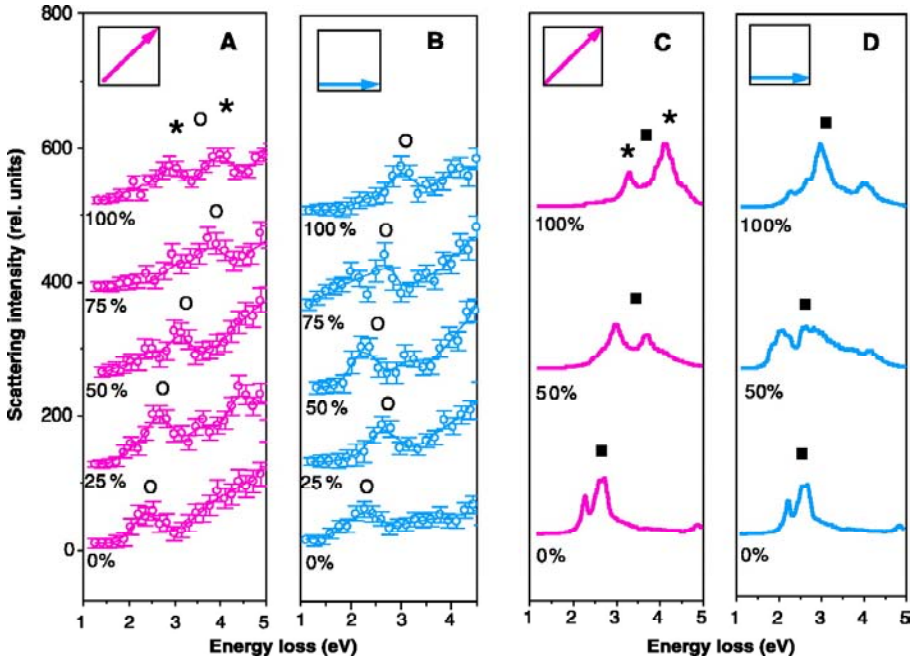

Figure 4.5.3 Momentum dependence of the RIXS spectra. The experimental spectra (with elastic scattering removed) along (A) <110> and (B) <100> directions, and the calculated ones (low-energy component only) along (c) <110> and (d) <100> directions. The parameter values for (C) and (D) are t = 0.35 eV, U/t = 10, t'/t = -0.34, and t''/t = 0.23, V_c/t = 15 [73][76][78]. The center of gravity of spectral weights are indicated by the open circles for the experimental data and closed squares for the Hubbard model calculations. The percent numbers show the normalized q co-ordinates (locations inside the Brillouin zone) and the inset in each panel shows the direction of the scattering wave vector (momentum transfer).

of higher-order hopping, the single-particle spectral function for the unoccupied states (upper Hubbard band) has a minimum near k = (π, 0) [Fig. 4.5.1] quite unlike the occupied band's maximum which is near k = (π/2,π/2). Such flatness is not expected in t-U model. The finite values of long-range hopping in the system have important consequence for the shape of the upper Hubbard band. It shifts the lowest energy state of the upper Hubbard band from (π/2, π/2) to (π,0). It was also confirmed that the excitation from occupied (π/2,0) to unoccupied (π,0) points induces the large spectral weight in the two-body Green's functions, in contrast to the case

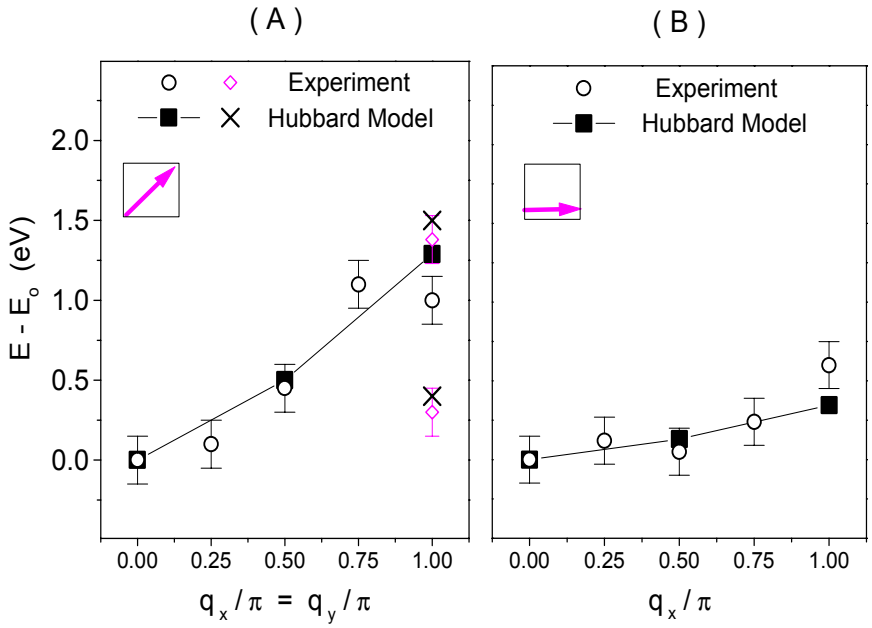

Figure 4.5.4 Momentum dependence of the center of gravity of the low-energy inelastic feature in the experimental and the theoretical (Hubbard model) results along (A) <110> and (B) <100> directions. Relative excitation energies are plotted referenced to the energy (E_o) at q = (0,0) along each direction. Open red circles and closed cyan squares denote experimental and theoretical centers of gravity, respectively. For q at the boundary (in Fig-(A)) in addition to plotting center of gravity (o, red) we plot the locations of two separable features.

of the excitation from the (π/2,π/2) to (π,0) points mentioned above. Other excitation processes with the momentum transfer (π/2,0) are higher in energy. Therefore, the flat dispersion from (0,0) to (π/2,0) in the RIXS is originated from the fact that the state at (π,0) in the unoccupied UHB has the lowest energy. Based on these experimental results we suggest that the doped electrons in n-type high temperature superconductors occupy mostly the states near (π,0) on the upper Hubbard band unlike the p-type superconductors which exhibit nodes near (π/2,π/2). The disparity between the p-type and n-type superconductors is most likely due to this asymmetry of the lowest energy states as extracted from our experimental data (different dispersive behaviors of two bands) [78]. Based on these results we construct a model for the dispersion behavior for the upper Hubbard band in cuprate Mott insulator as shown in Fig. 4.5.5.

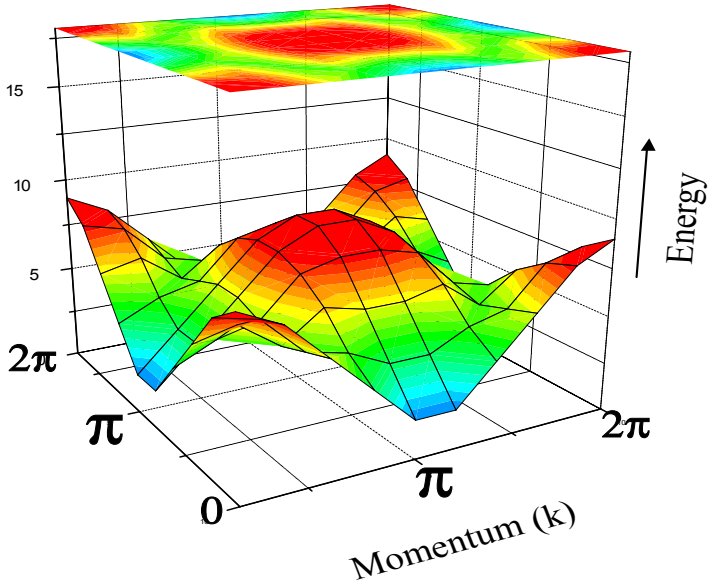

Figure 4.5.5 Schematic model for the momentum (k-) dependence of the unoccupied states (upper Hubbard band) in cuprate Mott insulator. The lowest energy state occurs at k = (π,0).

Further higher resolution work is definitely necessary to resolve the details of these issues. The single-particle spectral function analysis and the present q-resolved correlated charge-fluctuation spectral analysis, taken together, restrict the values of long-range hopping parameters in a consistent fashion. These results in general indicate that the q-resolved charge excitations across the Mott gap can be described within the framework of standard Hubbard model.

4.6 Conclusion

Our results from this experiment hints on the power and versatility of x-ray spectroscopy, and its complementary nature to other well-developed spectroscopic techniques, in addressing some fundamental issues of charge excitation in Mott insulators that are not directly possible by other well-developed spectroscopic techniques. The availability of brighter synchrotron sources with higher resolution would permit a more detailed study of various aspects of Mott insulators, such

as the possibility of the broken particle-hole symmetry (as hinted here), the magnitude of intersite Coulomb coupling, importance of long-range hopping and charge correlations in a Mott state as in quasi-two-dimensional high T_c parent cuprates. It would be interesting to look at the doping dependence of these features and study how the system evolves from the Mott insulator to a high T_c superconductor among other things. The feasibility of such experiments points to the opening of a new frontier of correlated systems research.

Chapter 5

Charge Dynamics in a Quasi-One-Dimensional Mott Insulator

Lower dimensional systems possess fewer degrees of freedom. The theoretical machineries to study many-body quantum effects have had better success in understanding behavior of correlated electrons in one dimension as compared to higher dimensions [84]-[90]. In the 1960s, Lieb and Wu suggested that the low-energy excitations in a 1D system with short range antiferromagnetic correlations are not quasiparticles with charge e and spin 1/2 as it would be in an ordinary Fermi liquid. Instead, they are decoupled collective modes of spin and charge excitations called spinons and holons [87]. The decoupled nature of the excitations leads to different speeds for spin and charge propagation. This is interpreted as the separation of the spin and charge degrees of freedom for a single electron, or equivalently, a decay of a quasi-hole into a holon and a spinon. This novel concept has received renewed interest, largely due to the recent attempts to understand high-T_c superconductors in the context of Mott systems [43][44][84][86]. An experimental investigation of this phenomenon is of conceptual significance for several reasons. First, it provides a strong test for the many-body theoretical model Hamiltonians that are extensively used to describe highly correlated electron systems. The solution of these Hamiltonians are well accepted in one dimension. A comparison of experiment and theory thus provides a quantitative test for the models. Second, if spin-charge separation does occur in one dimension, holons, and spinons can be considered as new elementary particles in solids with similar conceptual importance as that of phonons or magnons. In this chapter we present study of momentum-resolved charge fluctuations in quasi-one dimensional Mott insulators and compare the results with quasi-two dimensional systems.

5.1 Charge Dynamics and X-ray Scattering

Several attempts have been made to detect the spin-charge separation using electronic spectroscopies in quasi-one dimensional system [91][95]. Recently, high quality single crystals of a new family of 1D antiferromagnetic insulators, such as $SrCuO_2$ and Sr_2CuO_3, became available which made many spectroscopic experiments possible [96]. Basic crystal structure and electronic configuration is shown in Fig. 5.1.1[97]. The important structural character of these compounds is that it has 180° Cu-O-Cu bonds that form the chains and the almost 90° Cu-O-Cu

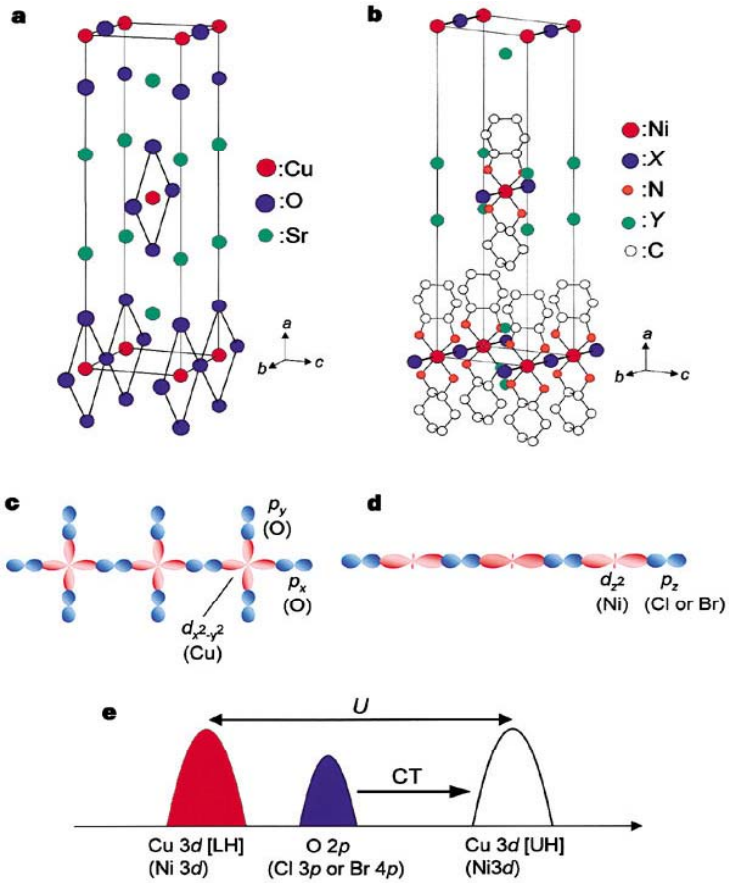

Figure 5.1.1 Crystal and electronic structures of the 1D Mott insulators. **a**, Structure of Sr_2CuO_3. **b**, Structure of $[Ni(chxn)_2X]Y_2$. **c**, Configuration of Cu $3d_{x^2-y^2}$ (red) and O $2p_x$, $2p_y$ (blue) orbitals in Sr_2CuO_3. **d**, Configuration of Ni $3d_{z^2}$ (red) and X $2p_z(4p_z)$ blue orbitals in $[Ni(chxn)_2X]$ Y_2. **e**, Schematic electronic structure of the 1D Mott insulators [97].

bonds that give the coupling between the chains. The coupling along the chains is at least an order of magnitude stronger than the interchain coupling, making $SrCuO_2$ a quasi-one dimensional compound. $SrCuO_2$ has a weakly coupled double Cu-O chain structure [96]. For low-energy excitations, these materials can be modeled by chains of atoms with one electron per site. The electrons on the neighboring sites interact with each other through the antiferromagnetic exchange interaction J [96][98][99].

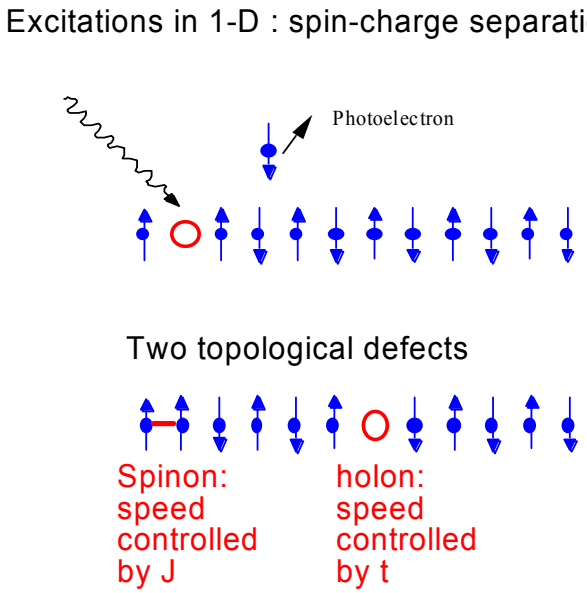

Figure 5.1.2 The topological defects created in a spin-1/2 antiferromagnet can move within the linear lattice without breaking more than one bond. The decoupled nature of these motions can be thought of separation of spin and charge fluctuations. The ture nature of these excitations are highly delocalized and there is no long-range antiferromagnetic order so the limitations of above cartoon should be kept in mind [87].

In a spin-1/2 quantum Heisenberg antiferromagnetic chain , when an electron is kicked out by a photon, it leaves a hole behind it. Hopping of this hole to a neighboring site, or equivalently, hopping of a neighboring electron into the hole site, creates a magnetic excitation marked as a short dash in the Fig. 5.1.2. However, additional hopping in the same direction does not create magnetic excitations (Fig. 5.1.2). The motion of the charge vacancy is free from magnetic interaction aside from the first step. Therefore, the original single photohole decays into two separate ``defects'' in the chain. The motion of the charge is governed by the hopping energy t and

the propagation of the magnetic excitation is governed by exchange interaction J . Propagating with two different speeds, these two defects can be regarded as two separate particles that is, spin and charge are separated and they give the essence of a holon and a spinon [98][99]. Thus, even without going into a rigorous approach, we know that the spin-charge separation may manifest itself through a mixture of two branches of dispersive bands due to two particles with different interaction energies in the electronic excitation spectrum. ARPES results exhibit similar branching of low energy excitations [98][99]. ARPES looks at the dynamics of a photohole injected into the system hence measure the quasiparticle excitations and different decay products show up as different branches of excitation bands. Holon is in essence a collective charge mode. So naturally, it would be interesting to use a probe which couples directly to the collective charge fluctuations in the system. In this sense inelastic x-ray scattering is the natural probe to study such excitations.

5.2 Experimental Conditions

The experiment on the quasi-one dimensional system was performed using the high flux undulator beamline 12-ID (BESSRC-CAT) at the Advanced Photon Source of Argonne National Laboratory. Inelastic scattering was measured by varying q along the chain direction (Cu-O bond direction) of single crystalline Sr_2CuO_3. Overall energy resolution of 325 meV was achieved for this experiment. This is an improvement over our earlier works on 2-D Mott systems by more

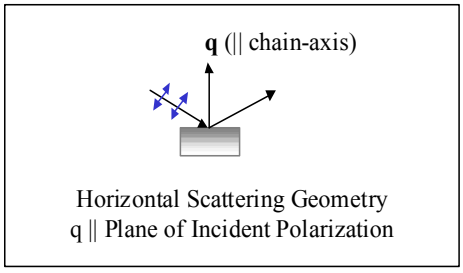

Figure 5.2.1 A schematic showing the scattering geometry for the experiment. In this arrangement incident polarization had a nonvanishing component along the direction of momentum transfer.

than 100 meV [100][101]. This improvement in resolution (in combination with the high flux from the Advanced Photon Source) allowed us to resolve the Mott excitations in 1-D systems despite high-level of x-ray absorption due to Sr in the system. The energy of the incident beam was set near the Cu K-edge (E_o = 8.996 eV) for resonant enhancement of excitation features (Fig. 5.2.2). The scattered beam was reflected from a diced Ge-based analyzer (Ge(733)) and focused onto a solid-state (Cd-Zn-Te based) detector. For q-scans, the incident energy was kept fixed and q was varied by rotating the entire spectrometer around the scattering center. The background, measured on the energy gain side, was about 2-3 counts per minute. Sr_2CuO_3 and $SrCuO_2$ crystals used for this experiment were grown and characterized by techniques described previously which confirmed its quasi-one dimensionality above 6 K (Neel transition due to 3-D coupling) [96]. Unlike extensively studied 1-D cuprates such as $CuGeO_3$ or $KCuF_3$, Sr_2CuO_3 and $SrCuO_2$ show no spin-Peierls transition hence provide a unique opportunity to study the charge fluctuations in a 1-D spin-1/2 quantum Heisenberg system [96][98].

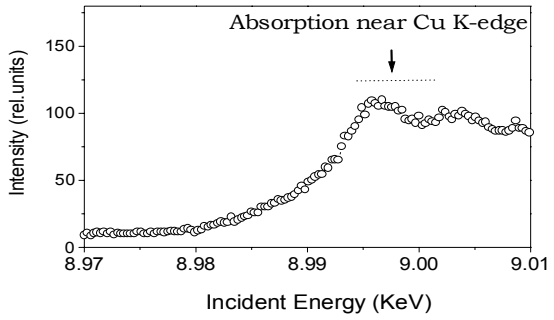

Figure 5.2.2 Absorption spectrum near Cu K-edge. The enhancements of inelastic excitations were seen several electron volts past the absorption edge. The dotted line marks the energy region near the absorption edge where incident x-ray energies were used for the experiment.

5.3 Excitation Spectra in One Dimensional Cuprates

Fig. 5.3.1 shows inelastic x-ray scattering spectra with varying momentum transfers along the chain direction (the Cu-O bond direction) with incident energy fixed near Cu K-edge (E_o = 8.996 keV). All the spectra in each panel were normalized using intensities from a window of 8 to 9 eV

energy-loss. Each spectrum shows two features, one around 5.6 eV and another, lower in energy, appear in the range of 2.5 to 3.5 eV depending on different values of the scattering wave vector, **q**. The 5.6-eV feature can be assigned to be a charge transfer excitation from the groundstate to the antibonding-type excited states which is analogous to the 6 eV excitation observed in 2-D cuprate insulators [10][25][76]. In order to have a closer look at the low-energy feature, we remove the quasi-elastic scattering by fitting and plot with a narrower energy range in Fig. 5.3.2. The lower energy feature has a significant movement in changing **q**. The feature disperses upward in energy about 1 eV monotonically over the full Brillouin zone in going from q = 0 to the edge of the zone (q = π). For the **q**-scans incident energy was set fixed at 8.996 keV. Inelastic features were also seen for incident energy of 8.992 keV and found similar within the level of experimental resolution. Two differently chosen incident energies allowed us to check for dispersions possibly arising due to spurrious instrumental systematics.

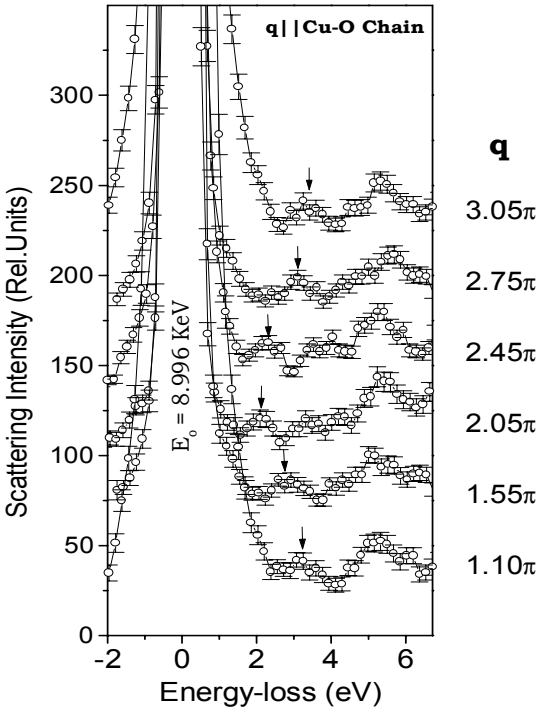

Figure 5.3.1 Inelastic x-ray scattering spectra near Cu K-edge are shown along the chain direction (the Cu-O bond direction). The values of **q** range from π to 3π. In this range of q the lower energy feature disperses about 1 eV. Incident photon energy was set to 8.996 KeV.

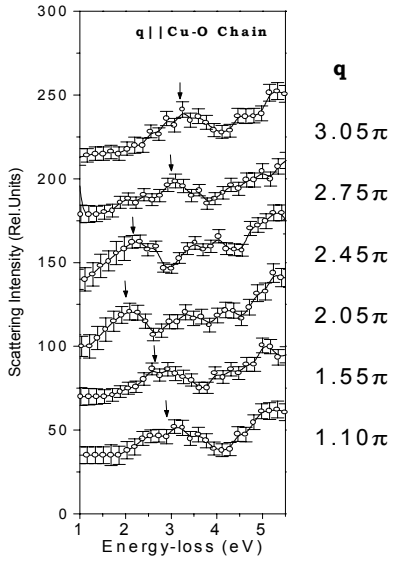

Figure 5.3.2 The low energy inelastic feature is shown without the background. The dispersive nature of the feature becomes more prominent after the subtraction of the quasielastic background.

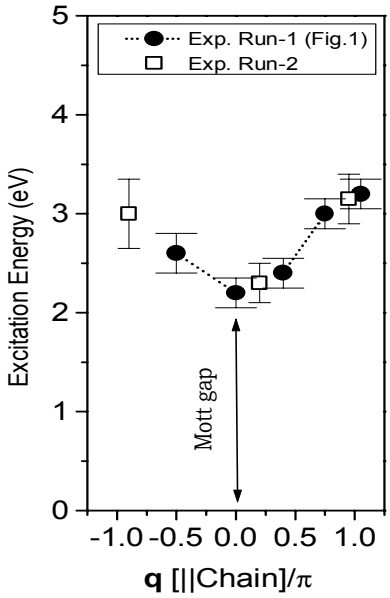

Figure 5.3.3 Dispersion Relation : Energy position of the excitation plotted as a function of momentum transfer (q). Data from two independent experimental runs are plotted together. They fall on a nearly parabolic curve (not shown in figure). The dispersion is shown in the (-π,π) range although the experiments were perfomed on different but equivalent parts of the Brillouin zone.

In Fig. 5.3.3 we plot the dispersion relation (energy vs. momentum) of the excitation. The plot shows the dispersion within the first Brillouin zone ($-\pi,\pi$) based on the values in equivalent parts of the Brillouin zones. The dispersion can be easily fit to a parabolic function much like the dispersion of a free particle. In the next section we compare the experimental dispersion relation in 1-D with the dispersion we measured in a quasi-two-dimensional system along the Cu-O bond direction with expectations from Hubbard model.

5.4 Charge Excitations : 1D vs. 2D

One dimensional half-filled spin-1/2 quantum systems are believed to exhibit spin-charge separation. As a consequence, in these systems charge fluctuations propagate rather freely and independently of the spin fluctuations [85]-[90]. This is in contrast to the two dimensional (2-D) spin-1/2 systems where charge motion is strongly coupled to the spin fluctuations and rather restricted [85]-[90],[98]. In 1-D, charge excitations would be expected to be highly dispersive compared to analogous 2-D systems in the presence of strongly Coulomb interaction. This behavior would contrast qualitatively to that of the band structure calculations with no interactions considered where the 1-D system would be expected to have only half of the dispersion than that of in 2-D (Fig. 5.4.1).

ARPES experiments performed on quasi-1D and quasi-2-D undoped cuprates suggest that the effective one-electron bandwidth in two dimensional case is actually smaller. ARPES results show a dispersive band as the crystal-momentum (k) is varied from 0 to π in quasi-one dimensional compound $SrCuO_2$. Detailed polarization analysis of the data yields multiple branches of dispersive bands for momenta from 0 to 0.5, but only a single band from 0.5 to 1 (in units of π/a with a being the Cu-O-Cu distance). The widths of the upper and lower bounds of the bands from 0 to 0.5 can be explained by underlying bands scaled by hopping energy (t) and superexchange interaction energy (J) , respectively, while the width of the band from 0.5 to 1 is scaled by t . These otherwise incomprehensible results can be naturally and quantitatively explained by many-body theoretical calculations. incorporating the concept of spin-charge separation. The observed dispersion (~ 1 eV) seen in $SrCuO_2$ below the insulating gap (Mott gap)

is much larger than the dispersion observed in $Sr_2CuO_2Cl_2$ which less than 0.3 eV as measured by ARPES.

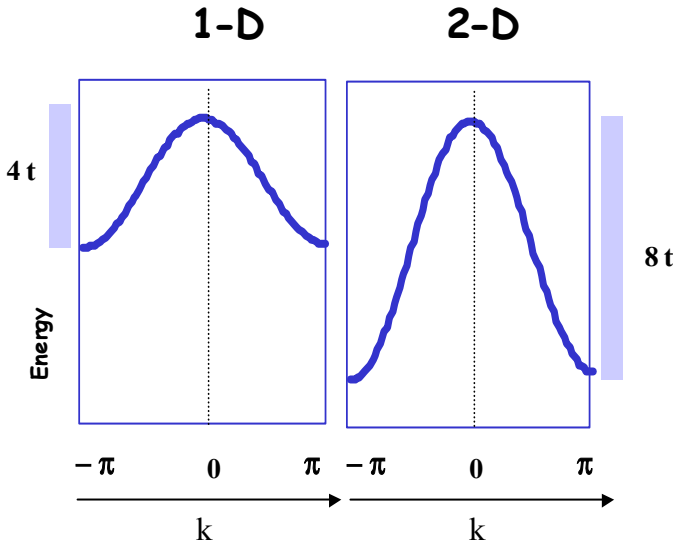

Figure 5.4.1 Model bandstructure in noninteracting 1-D and 2-D systems. The one-electron bandwidth for electrons in a 2-D lattice would be a factor of two larger than a 1-D lattice with same lattice constant. In 2-D electrons have "more room" to move about (delocalization). In the presence of strong electron electron interaction this simple relation would break down.

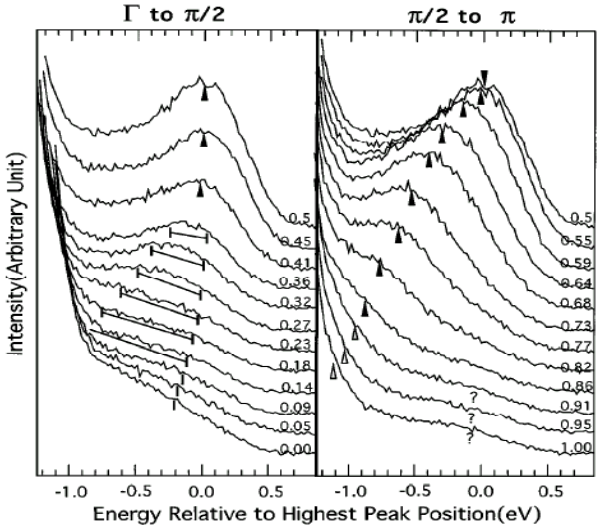

Figure 5.4.2 ARPES results show a dispersive band as the crystal-momentum (k) is varied from 0 to π in $SrCuO_2$. The dispersion is about 1 eV below the insulating gap (Mott gap) [98].

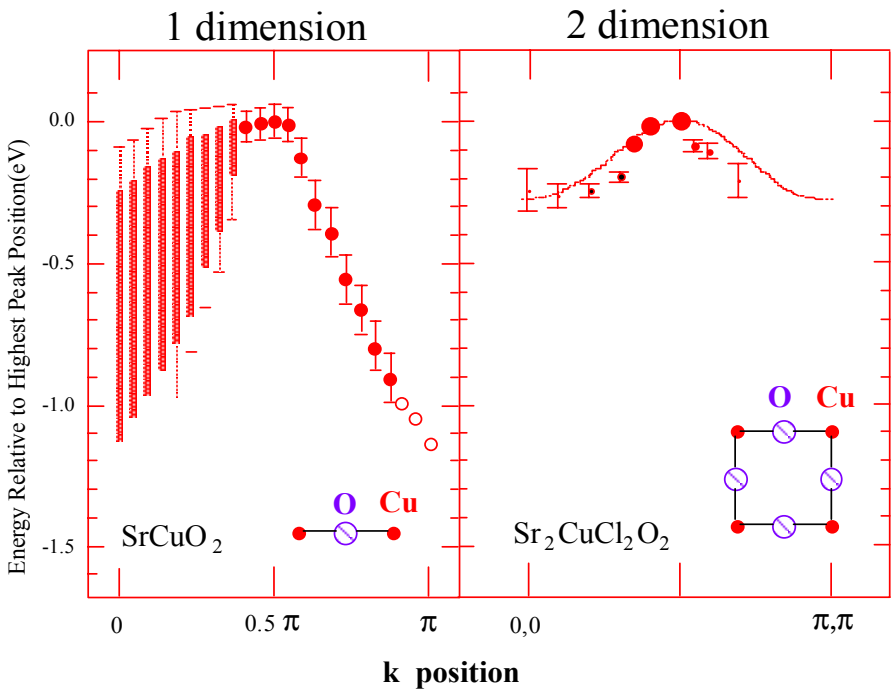

Figure 5.4.3 Comparison of dispersion in quasi-1D and quasi-2D case measured using ARPES : The dispersion is significantly lower in the two dimensional case compared to the dispersion in one dimension. This significant departure from the noninteracting case suggests the importance of strong electron-electron correlation in these low dimensional systems [98][99].

This significant departure from the noninteracting case suggests the importance of strong electron-electron correlation in these low dimensional systems. The large dispersion and the existence of two branches of excitations (or rather one single highly broad branch) for k below $\pi/2$ have been interpreted as being consistent with spin-charge separation in 1-D Mott insulators.

In case of inelastic x-ray scattering, one measures the dynamical charge-charge correlation function (charge fluctuations) which can be interpreted as particle-hole pair excitations in the range of momentum-transfers comparable to the size of the Brillouin zone of the system. Near an absorption edge the measured response function gets modified but it can still be interpreted as composites of pair excitations [11-14]. The particle-hole pair formed in the process absorbs the energy and momentum lost from the incident x-ray beam and propagates in the direction of **q**

with momentum ħ**q**. The propagation of this pair would depend on the charge and spin distributions in the system. X-rays couple to the charge degrees of freedom and measure the propagation of charge fluctuations in the system.. In case of the 1-D Mott insulator we studied, the charge fluctuations at the edge of the Mott gap are holons. One can construct a simple model to interpret charge fluctuations involving holons. Assuming spin-charge separation, the occupied states would have a bandwidth of 4t same as it would be for the unoccupied states (Fig. 5.4.3(left)) but such "bands" are separated by the Coulomb U. Now by taking convolution of these "bands" one can construct the charge fluctuation spectrum (ω(q)) as shown in Fig. 5.4.3 (right). One would then expect the onset of pair excitation energy to increase with increasing momentum transfer.

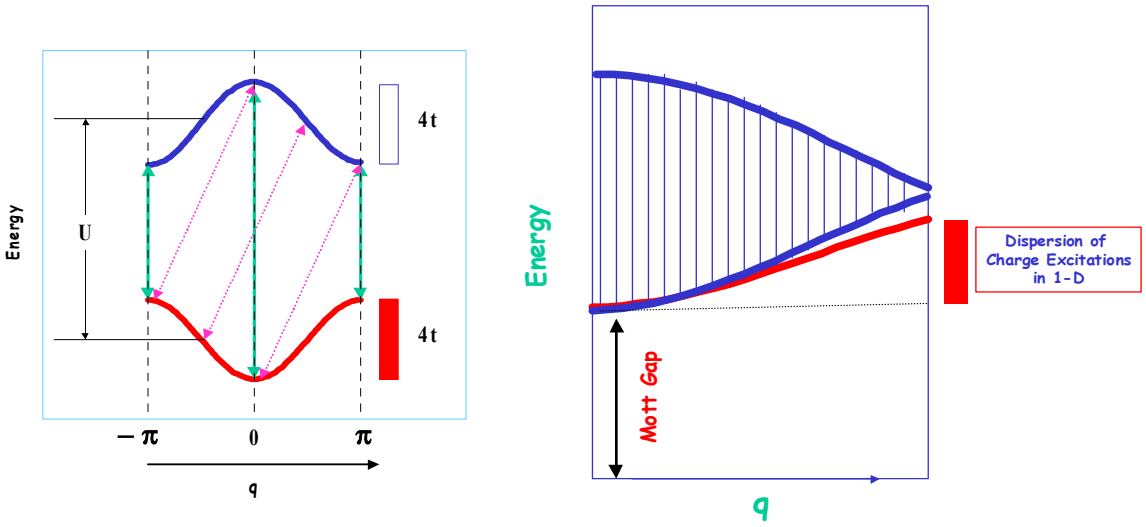

Figure 5.4.4 A cartoon model of the electronic structure of 1-D cpurates is shown. **(Left)** In the presence of spin-charge separation one can approximate the "charge bands" nearly parabolic (free-particle-like). **(Right)** The convolution of the occupied and the unoccupied bands then make up the charge excitation spectrum. The "red" line would be added to the spectrum in the presence of intersite coupling as calculated in [89][90].

Although this simple cartoon view captures the essentials of the excitation spectrum qualitatively, one can numerically calculate the excitations within Hubbard model. Similar to the 2-D case, one can calculate the momentum dependence of charge excitations in 1-D cuprates by using the exact diagonalization technique for the extended Hubbard model. The Hamiltonian in 1-D case can be written as :

$$H_{3d} = -t\,\Sigma_{i,\sigma}(d_{i,\sigma}^{\dagger} d_{i+1,\sigma} + \text{h.c.}) + U\,\Sigma_i n_{i,\uparrow}^{d} n_{i,\downarrow}^{d} + V\,\Sigma_i n_i^{d} n_{i+1}^{d}$$

where $d_{i,\sigma}^{\dagger}$ is the creation operator of 3*d* electron with spin σ at site i, $n_{i,\sigma}^{d} = d_{i,\sigma}^{\dagger} d_{i,\sigma}$, and $n_i^{d} = n_{i,\uparrow}^{d} + n_{i,\downarrow}^{d}$. The on-site Coulomb energy U corresponds to the charge transfer energy of cuprates. The values of the parameters are set to be $U/t = 10$ and $V/t = 1.5$.

In the intermediate states of Cu *K*-edge RIXS process, 3*d* electrons interact with a 1*s* core hole created by the dipole transition of a 1*s* electron to 4*p* orbital due to an absorption of an incident photon with energy ω_i and momentum K_i. This interaction is written as

$$H_{1s\text{-}3d} = -V_c \Sigma_{i,\sigma,\sigma'} n_{i,\sigma}^{d}\, n_{i,\sigma'}^{s},$$

where $n_{i,\sigma}^{s}$ is the number operator of 1*s* core hole with spin σ at site i, and V_c is taken to be positive. This interaction causes excitations of the 3*d* electrons across the gap. The photo-excited 4*p* electron is assumed to go into the bottom of the 4*p* band with momentum k_0 and not to interact with either the 3*d* electrons or the 1*s* core hole due to delocalized nature of the 4p bands [6]. In the final state, the 4*p* electron goes back to the 1*s* orbital emitting a photon with energy ω_f and momentum K_f. The RIXS spectrum is then given by [79]

$$I(q,\Delta\omega) = \Sigma_\alpha |\langle\alpha|\Sigma_\sigma\, s_{k0-Kf,\sigma} p_{k0,\sigma}\, (H+\varepsilon_{1s\text{-}4p}-E_0-\omega_i-i\Gamma)^{-1}\, p_{k0,\sigma}^{\dagger} s_{k0-Ki,\sigma}^{\dagger}\, |0\rangle|^2 \delta(\Delta\omega-E_\alpha+E_0),$$

where $H = H_{3d} + H_{1s\text{-}3d}$, $q = K_i - K_f$, $\Delta\omega = \omega_i - \omega_f$, $s_{k,\sigma}^{\dagger}$ ($p_{k,\sigma}^{\dagger}$) is the creation operator of the 1*s* core hole (4*p* electron) with momentum k and spin σ, $|0\rangle$ is the ground state of the half-filled system with energy E_0, $|\alpha\rangle$ is the final state of the RIXS process with energy E_α, Γ is the inverse of the relaxation time in the intermediate state, and $\varepsilon_{1s\text{-}4p}$ is the energy difference between the 1*s* level and the bottom of the $4p_z$ band. The momentum component parallel to the 1D chain is represented by ΔK. The values of the parameters are set to be $U/t = 10$, $V_c/t = 15$ and $\Gamma/t = 1$ as for the 2D cuprates. The RIXS spectrum is then calculated on a 14-site ring by using a modified version of the conjugate-gradient method together with the Lanczos technique.

In Fig. 5.4.4 we compare the experimental results with calculations based on Hubbard model. The results are in good agreement with Hubbard model within the level of experimental resolution.

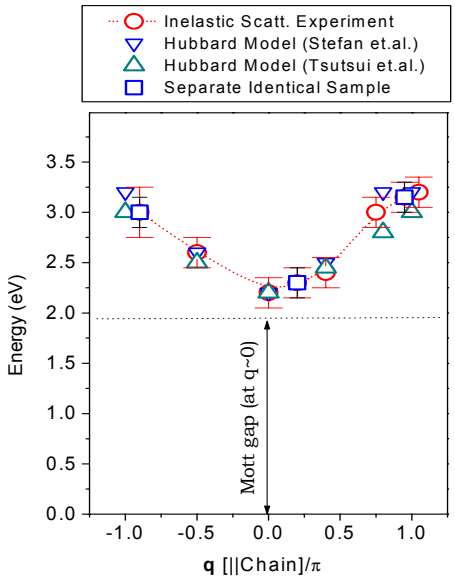

Figure 5.4.5 The momentum dependence of the center of gravity of the Mott features are compared with numerical calculations based on Hubbard model [79][89][90]. Experimental results show good agreement with the Hubbard model.

We now turn into the comparison of charge fluctuations in 1-D and 2-D. Fig. 5.4.5 shows comparison of dispersions of the charge excitations (near the edge of the gap) along Cu-O bond direction in 1-D and 2-D. The fluctuations in 1-D are more dispersive (more than 400 meV) than in 2-D. Such a behavior would be qualitatively expected from a system with spin-charge separation in the sense that charge fluctuations are free to move when they decouple from the spin and exhibits more dispersion. It is interesting to note that even the dispersion in 2-D along the Cu-Cu bond direction (45 degrees to the Cu-O bond) is comparable with dispersion in 1-D (Fig. 5.4.6). The results in 1-D and 2-D both agree well with Hubbard model within the level of energy and momentum resolution (Fig.4.5.4 (2-D) and Fig. 5.4.4 (1-D)).

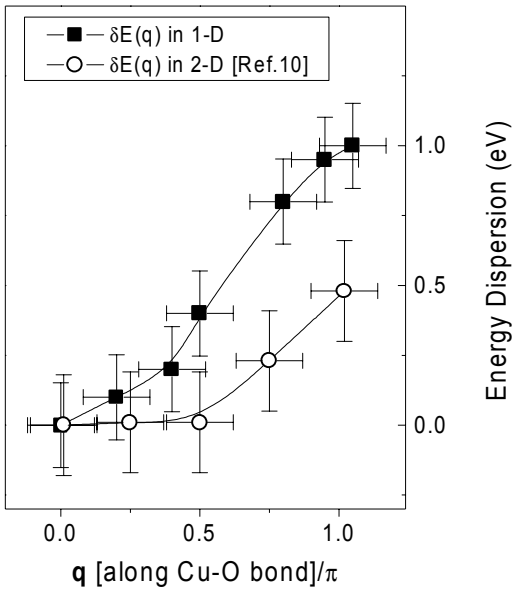

Figure 5.4.6 A comparison of q-dependence of charge excitations along the Cu-O bond direction in 1-D and 2-D. Charge excitations are experimentally found to be more dispersive in 1-D than in 2-D.

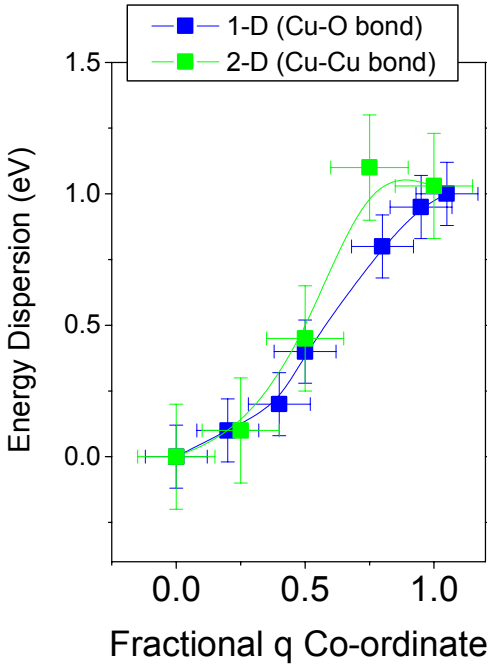

Figure 5.4.7 The dispersion in 2-D along the Cu-Cu bond direction (45 degrees to the Cu-O bond) is comparable with dispersion in 1-D.

5.5 Conclusion

We measured **q**-dependent charge fluctuations in a 1-D Mott insulator using inelastic x-ray scattering for the first time which indicates that in 1-D Mott gap is of direct nature (in the sense that the gap is smallest at q ~0) and excitations at the gap edge are more dispersive than in 2-D along Cu-O bond direction but compareable in other directions in the Cu-O plane (2-D system). The results are also consistent with Hubbard models describing the motion of holons in 1-D. The consistency of these results with model calculations for 1-D system suggests that the electron removal (ARPES) and electron addition (inverse ARPES) spectra would be symmetric at low energies [89][90]. Similar experiments could be performed when more than one orbital plays a role (as in many other transition metal oxides such as manganese oxides) and study the dispersions of collective orbital excitations which is a largely unexplored degree of freedom in a strongly correlated electron system.

As a future direction, it would be interesting to look at these correlated excitations in the presence of strong magnetic fields. Such studies can not be performed by electron-based spectroscopies such as photoemission or electron energy-loss spectroscopies.

These results in general suggest that inelastic x-ray scattering can be used to study electronic structure in complex insulators and correlated electron systems in general and would be complementary to standard momentum-resolved spectroscopies such as ARPES or Neutron scattering. Higher resolution experiments with better count-statistics would be necessary to extract quantitative details about the fundamental electronic parameters using such spectroscopies. Developments of high brightness x-ray synchrotrons can potentially make such experiments feasible with resolution at the millivolt regime.

Chapter 6

Charge Localization in Doped Cubic Manganites

The interplay of charge, lattice, spin and orbital degrees of freedom play important roles in determining various electronic and magnetic properties of transition metal oxides [46][47]. In perovskite manganites such interplay of various degrees of freedom lead to unusual groundstates which show anomalously large magnetoresistance and various magnetostructural transitions [47]. The discovery of colossal magnetoresistance in doped manganese oxides has lead to an extensive research interest in revealing the nature of electron correlations in these systems. In addition to

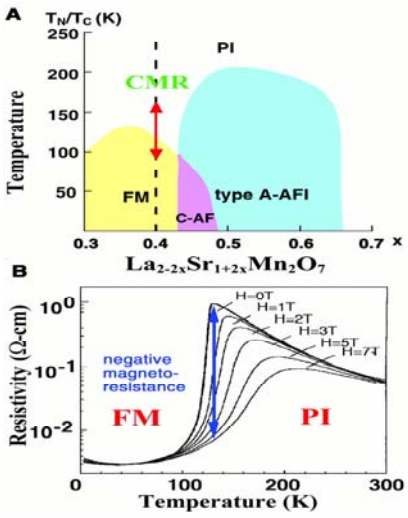

Figure 6.0.1 Phase diagram of an extensively studied manganite. Colossal magnetoresistance is observed near doping x ~ 0.4 in this system. The bottom figure shows the changes in resistivity as a function of applied magnetic field. (FM, PI and AFI stand for ferromagnetic metal, paramagnetic insulator and antiferromagnetic insulator respectively).

charge and spin degrees of freedom the valence electrons in manganites carry orbital degrees of freedom (Fig. 6.0.2) and exhibit strong localization and anisotropic effects. X-ray resonant

scattering is highly sensitive to charge localization and orbital orientations through polarization tunability of photons and its direct coupling to the charge densities [102]. In this chapter we briefly report our scattering studies of the metal-insulator transition in a cubic manganite $(NdSr)_{1/2}MnO_3$.

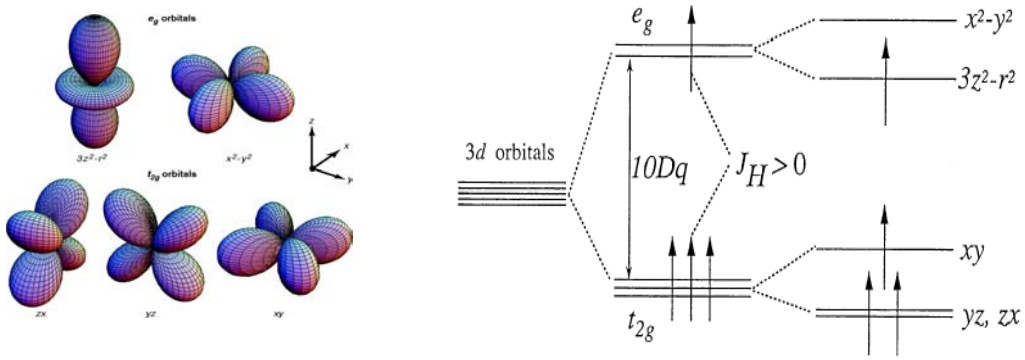

Figure 6.0.2 **(Left)** Five 3d orbitals. In the cubic crystal field, this fivefold degeneracy is lifted to two e_g orbitals [$(x^2\ y^2)$ and $(3z^2\ r^2)$] and three t_{2g} orbitals [(xy), (yz), and (zx)]. **(Right)** If the cubic symmetry at the Mn site is lifted the e_g orbitals [$(x^2\ y^2)$ and $(3z^2\ r^2)$] are further splitted. J_H is the Hund (rule) coupling between the d-electrons.

6.1 Charge-Orbital Order in Doped Manganites

Many cubic perovskites show strong metal-insulator transitions which are believed to be due to spin, charge and orbital ordering. A remarkable example of ordering/localization is seen in $(NdSr)_{1/2}MnO_3$ and $(PrSr)_{1/2}MnO_3$ which undergo metal-insulator transitions around 160K and 140K respectively [103]. In these systems, resistivity jumps by several order of magnitude as the system goes through the transitions.

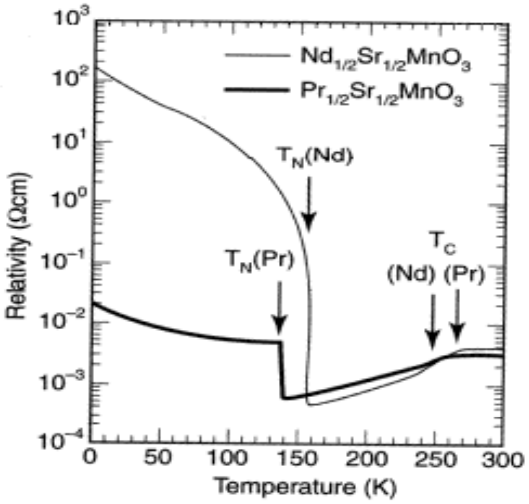

Figure 6.1.1. Temperature dependence of the resistivity of $(NdSr)_{1/2}MnO_3$ and $(PrSr)_{1/2}MnO_3$.[103]

It is believed that such metal insulator phase transitions in many doped manganese oxides are due to charge, spin and orbital ordering/localization of e_g electrons [46][47]. We have performed resonant elastic scattering on $(NdSr)_{1/2}MnO_3$, a cubic perovskite manganite, to look for any valence charge ordering through the metal to insulator transition in this system. We have observed charge and orbital-like superlattice reflections which appear in the insulating phase and exhibit strong polarization dependence of incident x-rays. Our x-ray scattering results are consistent with a CE-type charge [47] and orbital ordering in this system..

6.2 Superlattices in the Insulating $(NdSr)_{1/2}MnO_3$

Perovskite manganite $(NdSr)_{1/2}MnO_3$ has a pseudo-cubic crystal structure (Fig. 6.2.1). Neutron studies have shown that it shows a CE-type antiferromagnetic order [103]. We have used resonant elastic x-ray scattering to probe the possibility of charge localization and orbital ordering in this system [104]. Based on the crystal symmetry the main structural peaks in $(NdSr)_{1/2}MnO_3$ are

(h,k,l) with h+l even and k even when the indices are based on an orthorhombic distroted perovskite unit cell with a ≈ c ≈ 5.4 angstrom and b ≈ 7.5 angstrom.

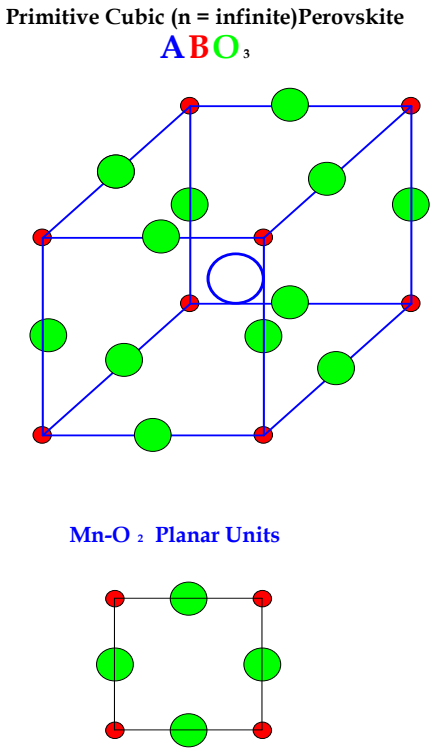

Figure 6.2.1 Crystal Structure of cubic manganites. Typically, cubic perovskites have ABO_3 structure (A, B and O refer to a rare-earth atom, transition-metal atom and oxygen atom respectively). Mn (red) atoms are octahedrally co-ordinated by the oxygen (green) atoms in this structural arrangements.

Diffraction due to new electronic order

X-rays strongly couple to the charge density distribution in a system. If some changes in the charge density occur due to some electronic phase transition it reveals a change in the scattering pattern of x-rays. Here we consider the simplest example of such a case. Consider a linear lattice of atoms with one atom per unit cell (Fig. 6.2.2). For x-ray scattering having q along the lattice one would find peaks corresponding to $q = n(2\pi/a)$ where n is an integer number. A scan of the scattered beam as a function of scattering angle would peak at $q(\theta) = 2\pi/a, 4\pi/a, 6\pi/a$ etc. with intensity scaled by $|f_o(q)|^2$ where $f_o(q)$ is the Fourier transform of charge density of one atom in

the unit cell with respect to q. This implies an overall monotonic decrease of scattering intensity at high q. Now, if the system goes through a phase transition which redistributes the electrons in the atoms in such a way that neighboring atoms along the lattice differ by two electrons the scattering pattern would change too. In this case one would see peaks additional peaks including the ones before the electronic redistribution. In this case one would see corresponding to n/2 where n is an integer number, in other words, the scattered beam would peak at q (θ) = π/a, 2π/a, 3π/a, 4π/a etc. with intensity oscillating with an envelop of overall decrease at high q values. The scattering of x-rays from charge, spin and orbital densities in condensed matter systems are described in Appendix A-4 in some details.

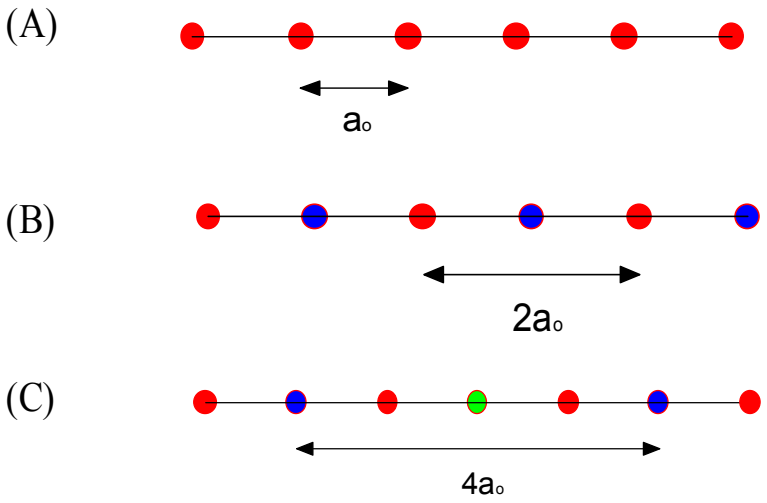

Figure 6.2.2 Changes in the charge distribution can be studied through the changes in the x-ray scattering pattern. The fundamental reflections in lattice A, B and C would be $2\pi/a_o$, π/a_o and $\pi/2a_o$ respectively.

Superlattices and their Temperature Dependence

We have observed three diffrent symmetry classes of superlattices in the low temperature insulating phase of $(NdSr)_{1/2}MnO_3$. In the 45 degree rotated perovskite unit cell, these belong to the following classes :

(1) (h,0,0) peaks with h odd.

(2) (h/2,0,0) peaks with h odd.

(3) (h/2,k,l) peaks with h odd and l nonzero.

The superlattices with (h,0,0) peaks with h odd integers correspond to charge ordering whereas superlattices with (h/2,0,0) peaks with h odd integers would correspond to some super-structures of charge ordering or lattice-coupled orbital ordering. This pattern is consistent with a model of CE-type AFM as proposed based on neutron scattering [46][47]. These superlattices appear only at low temperatures as one enters the insulating phase through the metal insulator transition (Fig. 6.2.3). They saturate below within 50K of the transition temperature. The superlattices we observed are (100), (300) and (500) for charge-ordering, (1.5,0,0), (2.5,0,0), (3.5,0,0) and (4.5,0,0) corresponding to lattice-coupled orbital ordering. The hysteretic behavior of (300) superlattice indicates that this transition is of first order. Temperature dependence of (5/2,0,0) and (3,0,0) are shown in Fig. 6.2.3. Other superlattices exhibit same temperature dependence.

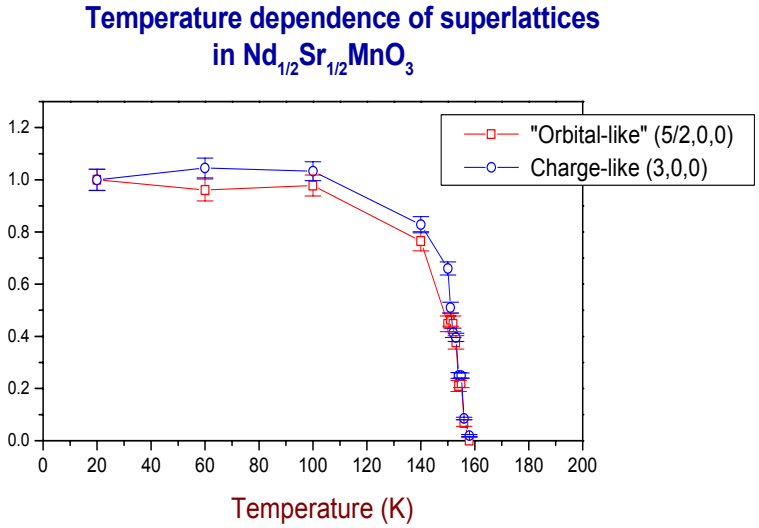

Figure 6.2.3 Teperature dependence of (3,0,0) and (5/2,0,0) superlattice. These superlattices appear only in the insulating phase which suggest that they are related to the valence electron ordering through the metal insulator phase transition.

6.3 Energy Dependence of Superlattices

In order to understand the electronic origin of these superlattices we have measured their energy dependence around the Mn K-edge (absorption edge). All the superlattices show characteristic enhancements close to the edge. Strong resonance enhancement near Mn K-edge would suggest that the superlattices involve Mn-atoms or electrons that originated from Mn-atoms. Energy dependence of (300) superlattice is shown in Fig. 6.3.1. This is characteristic of (h,0,0), h=odd integer class of superlattices. Besides the principal resonance near the edge this class of superlattices exhibits enhancement of scattering within 30 eV above the absorption edge (Fig. 6.3.1). We believe these resonances are due to the band-structure of Mn-4p states well above the fermi level. Such resonances are consistent with recent LDA+U calculations of Mn-O conduction bands [105]. It is interesting to note that these resonances are relatively weaker than the partial density of 4p states in this system. The energy profiles of the superllatices with (h/2,0,0)

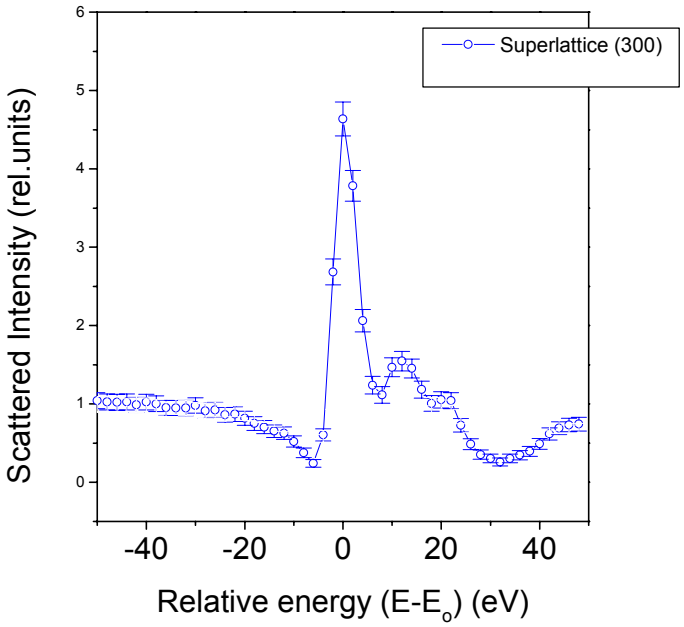

Figure 6.3.1 Energy dependence of superlattice (300) near Mn K edge (set as zero of energy). The superlattice (300) exhibits a strong enhancement at the Mn K edge. There are other weak resonances at energies past the edge.

Show similar strong enhancements near resonance. Within the CE-type models of ordering this class of superlattices could be identified as due to lattice-coupled orbital ordering. The energy structure shows additional weaker and broader resonances within 50 eV above the edge. These resonances reflect the band-like character of the empty 4p-states. If we normalize the orbital energy profile by the absorption curve we notice very weak and broad feature around 14 eV below the edgein the range of 6530 eV to 6545 eV. Scattering in this energy range would correspond to excitations involving the unoccupied d-bands (upper Hubbard band). The weak nature of this scattering suggests that the orbital ordering in this systems is strongly coupled to the lattice (periodic distortions of the oxygen octahedra).

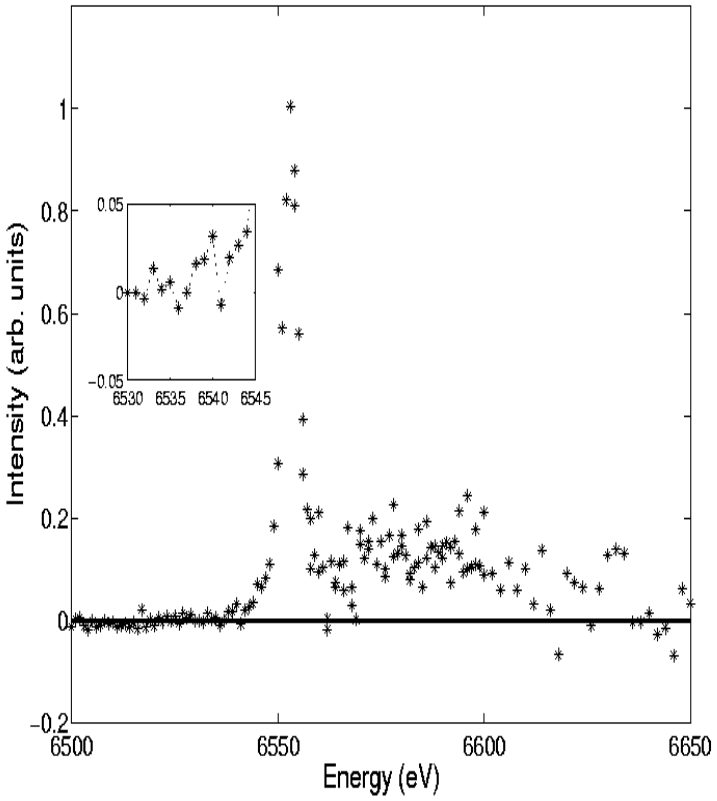

Figure 6.3.2 Energy dependence of superlattice (9/2,0,0) near Mn K edge (6553 eV). The superlattice (9/2,0,0) exhibits strong enhancement of scattering at the Mn K edge. There are other weak resonances at energies past the edge all the way up to 6650 eV.

6.4 Polarization Dependence of Superlattices

We have observed strong polarization dependence of the superlattices by performing azimuthal scans aroung the direction (axis) of the scattering vector (q). Azimuthal scan of (3,0,0) peak is shown in Fig. 6.4.1 and 6.4.2. The reference point for the azimuthal angle, $\Psi = 0$ corresponds to

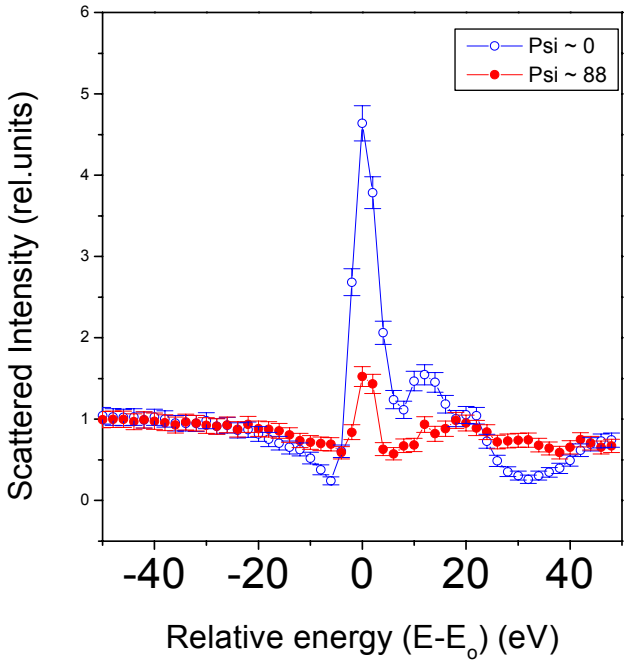

Figure 6.4.1 Polarization dependence of the (300) superlattice. Near 90 degrees azimuthal angle the scattering almost vanishes. Scattering curve for 88 degrees is shown.

c || **E** (x-ray field). Similar polarization dependence is also seen for the (h,0,0), h = odd integer class of superlattices. An azimuthal scan of (3/2,0,0) peak is shown in Fig. 6.4.2. The shape of the curve is not a simple $\cos^2(\Psi)$. This may suggest that the orbital ordering is more complex than a simple model of checker-board-like alternating orientations of orbital. A detailed model calculations would be necessary to extract electronic parameters from fit to these scattering results.

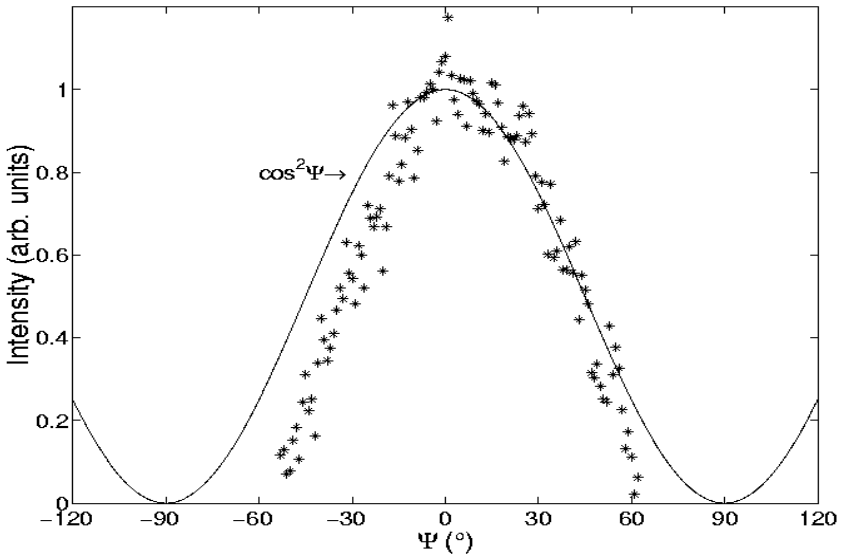

Figure 6.4.2 Azimuthal (Ψ) dependence of (3,0,0) reflection at resonance (6554 eV) at the base temperature (20 deg. K). This dependence can be fitted with squared sinusoids.

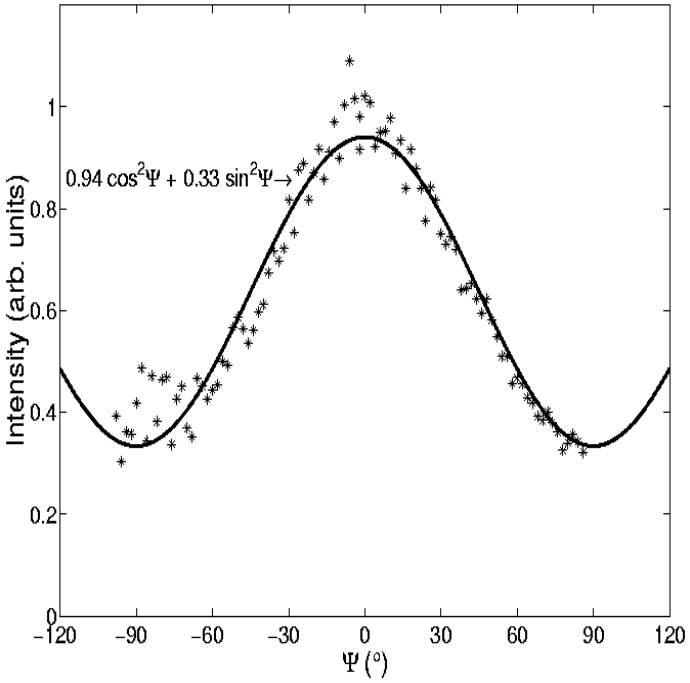

Figure 6.4.3 Azimuthal (Ψ) dependence of (3/2,0,0) reflection at resonance (6554 eV) at the base temperature (20 deg. K). This dependence can be fitted with squared sinusoids.

6.5 Structural Modulations

In addition to the superlattices that enhance at the Mn K-edge we have found a series of superlattices with very high intensities and Bragg-like energy dependence defined by the class (h/2, k, l), h odd and l nonzero. These superlattices appear in the insulating state only and disappear above 160 K. These are hysteretic too (Fig. 6.5.1). Once such superlattice is (1.5,2,3) which we studied in some detail. It has the same temperature dependence and hesteretic behavior as (300) but completely different resonance behavior. It's energy profile is Bragg-like. From (HKL) dependences we believe these reflections indicate some sort of structural modulations along the c-axis.

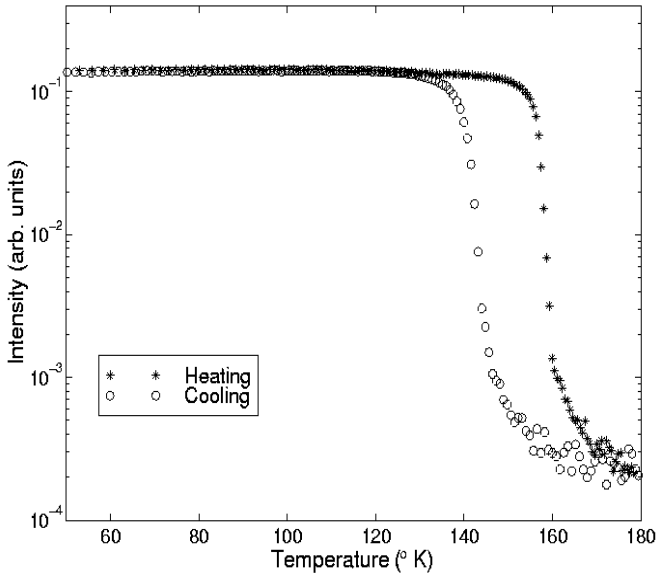

Figure 6.5.1 Temperature dependence of (1/2 0 4) peak. This peak corresponding to some structural modulation along the c-axis shows a hysteresis of about 15° K.

6.6 Conclusion

Perovskite manganite $(NdSr)_{1/2}MnO_3$ undergoes a huge resistivity jump near 160K and changes its magnetic correlations from ferro to antiferro-type as seen using neutron scattering. Using x-ray

scattering we have found evidences of carrier localization in this system. By going to resonance we have also observed superlattice peaks corresponding to some sort of lattice-coupled-orbital ordering in the system in the insulating state. The azimuthal anisotropy of this peak shows a two-fold symmetry which is what one would expect from ordering of the Mn-e_g states.

For future experiments, in order to understand the nature of the localized electronic states associated with this unusual phase it would be interesting to study how the scattering profiles of charge and orbital-like superlattices change as a function of doping as we go through the CE-phase by extracting the correlation length scales associated with localized charges and orientations of orbitals. This type of study would provide insights into the electronic mechanism behind long-range charge and orbital order that occur in various manganite systems leading to a better understanding of complex phase diagrams of manganites.

Besides the elastic resonant scattering reported so far, it would be interesting to frequency resolve the scattering signal and look at the (inelastic) excitations in a similar manner as demonstrated in case of cuprates (chapter 3-5). Resonant inelastic x-ray scattering can be used to look at new type of collective modes such as orbital waves ("orbitons" : Goldstone modes associated with orbital order) by studying their characteristic dispersions ($\omega(q)$: momentum-dependence) and polarizations. These orbital fluctuations are believed to play important roles in determining the physics of CMR and manganites in general [46][47]. Polarization tuned resonant inelastic scattering is the only direct technique to probe this novel type of orbital collective modes.

Chapter 7

Conclusion

The interplay of charge, lattice, spin and orbital degrees of freedom play important roles in determining various electronic and magnetic properties of transition metal oxides. The characterization of various groundstates and excitations in them is the goal of most spectroscopies. Charge localization, ordering and dynamics are among the central issues of strongly correlated electron systems. High energy and momentum resolution x-ray scattering spectroscopy can play a key role in elucidating the "charge" physics of correlated electron systems. Compared to electron-based techniques x-ray scattering possesses some key advantages and provides unique information about the scattering system :

- Often times interesting and nontrivial correlations appear at the edge or corner of Brillouin zones (BZ). X-rays allow to probe such parts of the BZ by covering much larger momentum space compared to electron scattering .
- Being a weak-coupling probe X-rays do not lead to multiple scattering and the spectra need no corrections based on sum-rules hence subtle effects are retained in the raw data.
- Polarization of x-rays allow one to study the symmetry character of excitation features.
- Core resonances accessible at x-ray energies allow one to determine the dominant chemical origin of charge excitations. This allows one to tune the intensities of excitation features of interest.
- X-rays probe the bulk (~ 1-10 micron in transition metal oxides) electronic properties thus surface complications (as they arise in electron-based spectroscopies) are avoided .
- X-ray scattering can be applied in the presence of an external field such as a high magnetic field unlike electron-based spectroscopies. One can then study changes in

the electronic structure driven by the magnetic field which is quite relevant for studying CMR effect, metamagnetic transitions or even quantum phase transitions.

- X-ray scattering can also be performed in the presence of high pressure. Such study are already underway in connection with modeling extreme geological conditions.

The disadvantage of x-ray scattering as a probe of electronic structure is its small cross-section. However, with the advent of 3rd generation of synchrotron facilities it is becoming possible to optimize beamlines for high count rates and high energy resolution (in the 1 to 100 meV range depending on cross-section of a particular process).

In this thesis, we have presented (and demonstrated) several momentum-resolved x-ray scattering study of charge dynamics and electronic order (localization) in Mott systems by starting with studying a simple metal to demonstrate the technique.

In case of the simple metal - a weakly interacting electron gas we found that the dominant contributor to density fluctuations was a volume plasmon. Plasmons are the zero-sound modes of a charged Fermi liquid but possess a mass even in the long-wave-length limit (small wave-vectors) due to the long-range nature of the Coulomb interactions. In case of weak interactions among electrons in the gas and at high number densities random phase approximation (RPA) works well to describe the excitation spectra. Under RPA, plasmon is stable and sharp at low momenta and increases in energy quadratically as a function of momentum until it hits the free particle-hole continuum and gets damped (Landau damping). The experimental results are consistent with RPA expectations within the level of energy and momentum resolution. We have also seen a change in plasmon scattering near a core resonance of the material. The scattering profile shows a dip near resonance suggesting some sort of interference effect. More systematic studies of such an interference effect can potentially be used to extract phase information associated with electronic excitations. Our preliminary studies are inadequate for a detailed analysis at this point but the results are promising for a future pursuit.

Perhaps the highlight of this thesis is the study of momentum-resolved charge fluctuations in low dimensional cuprate Mott insulators. Fluctuations dominate in low dimensional systems due to the existence of kinematic singularities. Many low dimensional systems exhibit exotic groundstates. Our momentum-resolved inelastic x-ray scattering studies show that in contrast to the mean field theories, charge fluctuations in 1-D are more dispersive than in 2-D which is

consistent with the view that in 1-D, due to spin-charge separation, charge motion is almost free. It is also interesting that the dispersions are consistent with calculations based on Hubbard model using parameters extracted from different types of experiments such as angle-resolved photoemission and neutron scattering. This is the first study of momentum-resolved charge dynamics in low dimensional Mott insulators covering the entire Brillouin zone for the first time.

Our study of charge localization in doped Mott insulators using resonant elastic scattering fell little short of its kind to be the first but the data quality obtained and the systematics performed are probably the best thus far as considered by many. We studied a system that shows the most dramatic metal to insulator transition (several orders of resistivity jumps). Associated with the jump was found a long-range ordering of e_g electrons. Scattering profiles, polarization dependence and length-scales associated with the superlattices observed are consistent with a CE-type ordering of charge, spin and orbital degrees of freedom. Results contribute to understanding the nature of e_g electron ordering in doped manganese oxides. It would be interesting to extend the study using inelastic x-ray scattering to understand the dynamics of these degrees of freedoms.

Although, we have focused to study charge dynamics in frequency space x-rays are being used to study dynamics in time domain. Unfortunately, the time domain studies are limited to slow time scales (up to micro-seconds) hence can not provide much insight about electron dynamics. The recent developments in building a coherent x-ray source is a promising step forward in studying dynamics of condensed matter systems with x-rays [106].

Appendix : A-1

[1]Basic Instrumental Components of Synchrotron Radiation

Synchrotron Radiation :

Charged particles do not radiate while in uniform motion, but during acceleration a rearrangement of its electric fields is required and this field perturbation, travelling away from the charge at the velocity of light, is what one observes as electromagnetic radiation [28]. Such emission occurs, for example, in a radio antenna where electric charges are periodically driven up and down the antenna at the carrier frequency specific for the station. Free accelerated electrons radiate similarly, although now the source (antenna) is moving. Radiation from a fast moving particle source appears to the observer in the laboratory as being all emitted in the general direction of motion of the particle. This forward collimation is particularly effective for highly relativistic electrons where most of the radiation is concentrated in a small cone with an opening angle of $1/\gamma$ (some 0.1 to 1 mrad), where γ is the particle energy in units of its rest energy (typically 10^3 - 10^4) [28]. In synchrotron radiation sources (storage rings) highly relativistic electrons are stored to travel along a circular path for many hours. Radiation is caused by transverse acceleration due to magnetic forces in bending magnets (forming the circular path) or periodic acceleration in special insertion device magnets like undulators, wiggler magnets and wave length shifters. Radiation is linearly polarized in the plane of acceleration (in most cases the horizontal plane). Elliptical polarization occurs for bending magnet radiation observed from above or below the midplane. The radiation is emitted in pulses of 10 - 20 picosecond separated by some 2 nanosecond or longer separation if desired [28].

[1] H. Wiedemann "Synchrotron Radiation Primer" (1998). Web-reference : http://www-ssrl.slac.stanford.edu

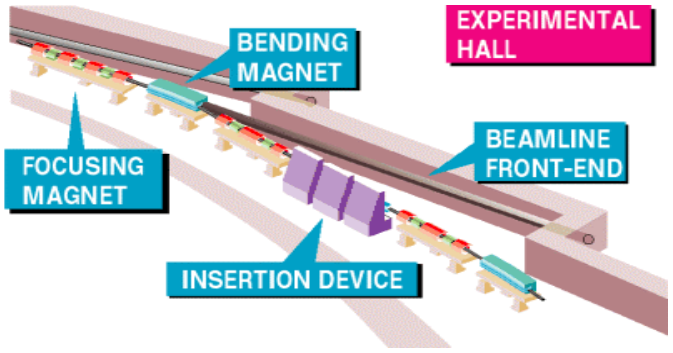

Figure A.1.1 A schematic showing the standard arrangement of magnet-based devices used to amplify photon beams with respect to the synchrotron source [27].

Undulator :

The electron beam is periodically deflected by weak magnetic fields. Similar to antenna radiation the particle emits radiation at the wavelength of its periodic motion in the undulator. To the particle this wavelength is the undulator period length λ_p) divided by γ due to relativistic Lorentz contraction. In the laboratory system this wavelength appears to the observer further reduced by another factor γ due to the Doppler effect. The undulator period length of the order of cm's is thus reduced by a factor γ^2 (10^6 - 10^8) to yield short wavelength radiation in the VUV and x-ray regime. The spectral resolution of the radiation is proportional to the number of undulator periods and its wavelength can be shifted by varying the magnetic field.

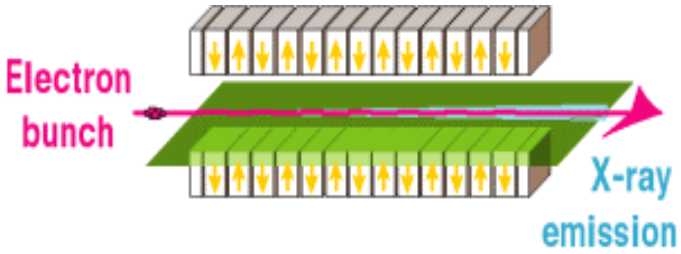

Figure A.1.2 Schematic of an undulator. An electron bunch traveling through the undulator generates high intensity co-propagating x-ray beams [27].

Wiggler magnet :

Increasing the magnetic field strength causes the pure sinusoidal transverse motion of electrons in an undulator to become distorted due to relativistic effects generating higher harmonics of the single wavelength undulator radiation. The monochromatic undulator spectrum therefore changes into a line spectrum. For very strong fields many harmonics are generated which eventually merge into a continuous spectrum from IR to hard x-rays. The spectral intensity varies little over a broad wavelength range and drops off exponentially at photon energies higher than the critical photon energy, $e_{crit} \sim B\gamma^2$. Compared to bending magnet radiation, wiggler radiation is enhanced by the number of magnet poles and is well collimated within an angle of K/γ or a few mrad [28].

Bending magnet :

Radiation is emitted tangentially to the orbit similar to a search light while well collimated in the nondeflecting, or mostly vertical plane. the observer at the experimental stationsees radiation from only a small fraction of the circular path which can be described as a piece of a distorted sinusoidal motion. The radiation spectrum is therefore similar to that of a wiggler magnet while the intensity is due to only one pole. Because the geometry of the storage ring is determined by bending magnets, it is not possible to freely choose the field strength and the critical photon energy is therefore fixed [28].

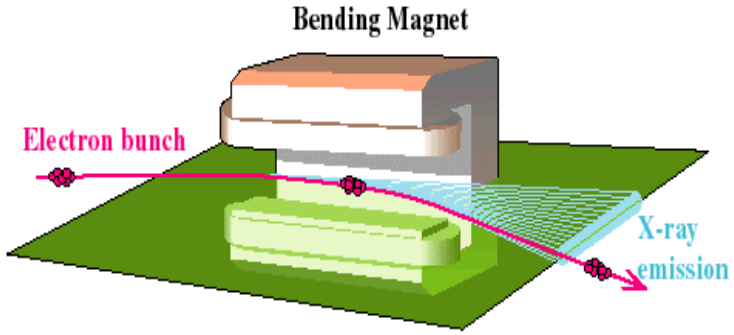

Figure A.1.3 An electron bunch deflected by a strong magnetic field generates high intensity x-ray beams [27].

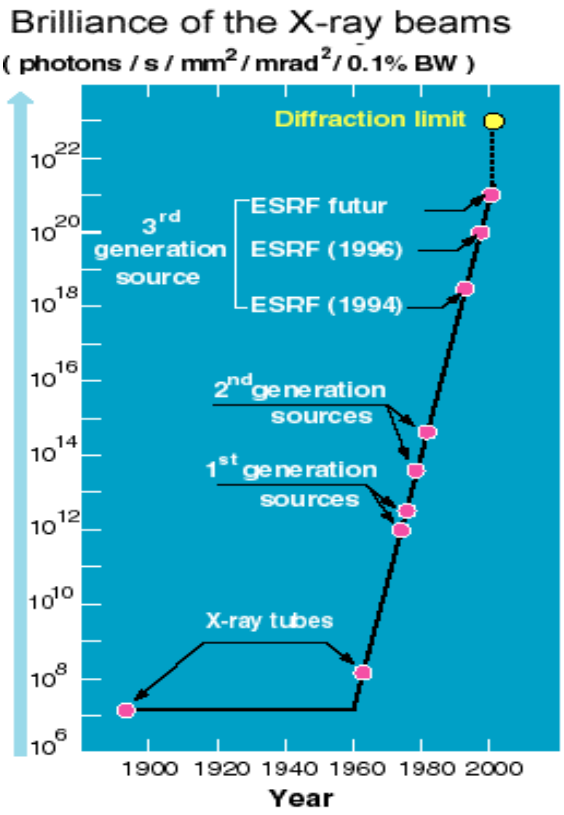

Figure A.1.4 A timeline sketching the development of x-ray sources. It is interesting to note that the sources have developed by more than 14 order of magnitude in last 40 years [27].

Appendix : A-2

Extraction of a Resonance Profile for Plasmon Scattering

X-ray Resonance Study of Plasmons in Electron Gases : Analysis of Al_3Ni Data

Systematics of Analysis :

O Raw Intensitites are normalized by incident flux (detector closest to the sample).

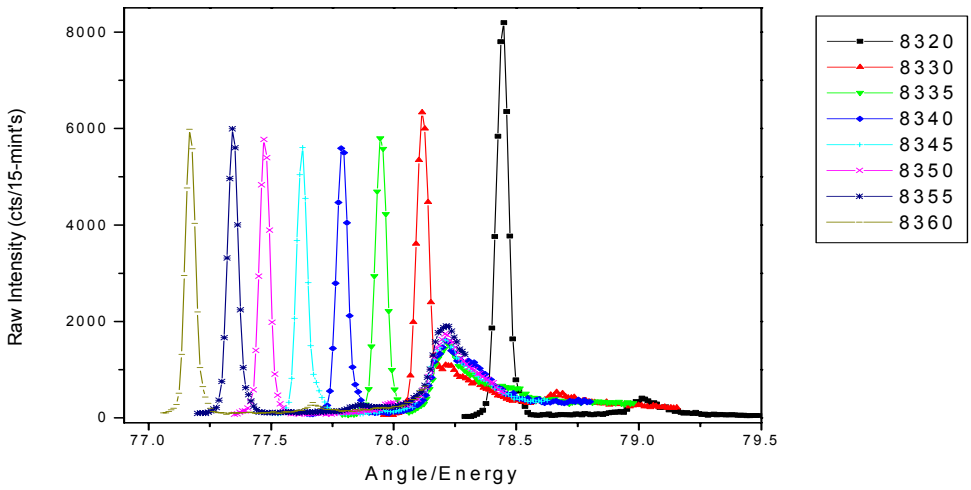

Figure A.2.1 Energy dependence of raw intensitiesof the excitation spectra

Dealing with the Background :

O Spectra show a (Auger-type) fluorescence decay near and above resonance. Plasmon sits on top of this fluorescence for energies near resonance. To extract plasmon intensities we need to correct for this additional flsc background. Plasmon peak moves on top of this background. We take two spectra where plasmons are well separated from each other but on either side of the flrsc peak and use one for the other's background. It is necessary to rescale the plots within 10% for the

flrsc curves match exactly in intensity as it should be (Note: flrsc intensity increases with increasing incident energy - an expected behavior). For Eo = 8345 eV plasmon is on the lower energy-loss side of the flrsc peak so it is safe to use the higher energy-loss side part of the flrsc peak for background subtraction to extract the plasmon for Eo = 8335 eV (below).

O Background corrected plasmons are presented in the plot below. We extract the integrated intensity of plasmons (this is not corrected for absorption yet).

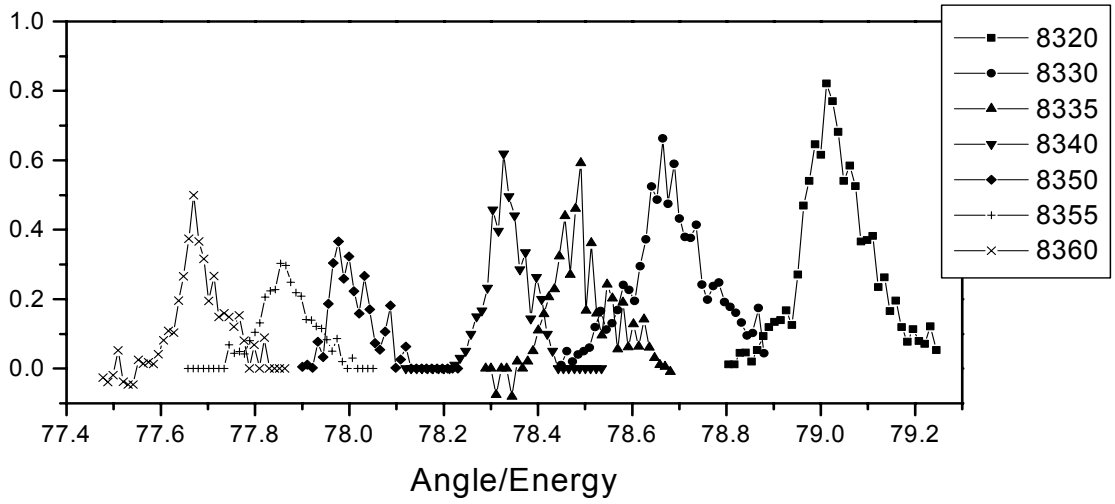

Figure A.2.2 Energy dependence of background subtracted intensities of the excitation spectra.

Dealing with the Differential Absorption :

O Now we move into the business of absorption correction. For a symmetric reflection geometry absorption would introduce an effective scattering volume namely, $A_o/2\mu$, where A_o is the beam size and μ is the inverse absorption length (for which intensity falls off by a factor of 1/e, about 37%). Inverse absorption length is related to the absorption cross-section by the material's density ($\mu(E) = \sigma_{Abs}(E) * \rho$). We are only interested in the ratio of absorption at resonance compared to the non-resonant absorption :

$$V_{NR}/V_R = (1/\sigma_{NR})/(1/2\sigma(E_{in}) + 1/2\sigma(E_{out}))$$

$$V_{NR}/V_R = ((1/\mu_{NR}/((1/2\mu(E_{in}) + (1/2\mu(E_{out}))), \quad \mu = \sigma_{Abs} * \rho$$

$$V_{NR}/V_R = (L_{a\,(NR)}) / ((L_a(E_{in}) + (L_a(E_{out}))/2), \qquad 1/\mu = L_a$$

L_a 's (Absorption lengths) are calculated using the standard program available at the CXRO/Berkeley website (http://cindy.lbl.gov/optical_constants/atten2.html). *(Note : Elastic peak intensities do NOT quantitatively follow these absorption ratios but qualitatively similar).*

Table A.2.1

Energy	*Abs-Corr Factor*	*Error Factor*
8320	1	1
8330	1.15	1.5
8335 (mid-edge)	1.6	1
8340	1.6	1
8345*	Not used	N/A
8350	3	1.1
8355	3.8	1.1
8360	3.8	1.1

* Plasmon can not be identified in the raw data hence Eo = 8345 eV was not used for analysis.

O Plasmon intensities (area) were extracted from the background corrected data and further corrected for absorption factors resulting in the following table and plot (errors are statistical plus that arise from backgroud corrections) :

Table A.2.2

Energy	*Raw-Int*	*Abs-Corr*	*Corr-Int*	*Error*
8305	10.5	1	10.5	0.6
8320	10.04	1	10.04	0.6
8330	8.6	1.15	9.9	1.1
8335	4.67	1.6	7.47	1.6
8340	4.52	1.6	7.23	1.7
8345	Not used	--	--	--
8350	2.9	3	8.7	1.7
8355	3.24	3.8	12.31	1.2
8360	3.67	3.8	13.95	1.2

Incident X-ray Energy Dependence of Plasmon Cross-section

Data show a dip in the resonance profile of plasmons in Al_3Ni near the absorption edge but beyond the absorption edge plasmon is enhanced. This suggests a coupling of plasmons to the resonance process (resonant and non-resonant channels interfere) and create features on the resonance profile. Earlier analysis suggests that dispersion (q-dependence) of plasmons remains identical above the resonance where an effective enhancement of intensity is observed. This is the first experimental demonstration of coupling (and role of the local phase) of a long-range charged collective mode to the resonance process using inelastic x-ray scattering. These results shed light on interpreting dispersion behavior (q-dependence) of charged excitations at resonance using inelastic x-ray scattering.

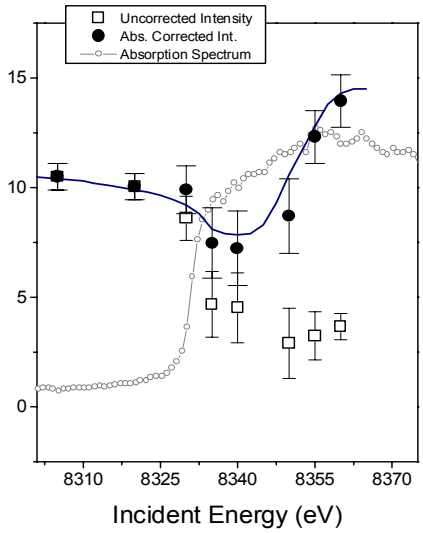

Figure A.2.3 Incident energy dependence of plasmon scattering. Both absorption corrected and uncorrected intensities are plotted.

Appendix : A-3

Equivalent Brillouin Zone Co-ordinates for a 2-D Square Lattice

Acutal measured q point	Near Equivalent Zone Co-ordinate
(1.92π, 1.92π)	(0, 0)
(1.72π, 1.72π)	(π/4, π/4)
(1.56π, 1.56π)	(π/2, π/2)
(1.23π, 1.23π)	(3π/4, 3π/4)
(1.1π, 1.1π)	(π,π)
(2.11π, 0)	(0, 0)
(2.2π, 0)	(π/4, 0)
(2.51π, 0)	(π/2, 0)
(2.7π, 0)	(3π/4, 0)
(2.91π, 0)	(π, 0)

Appendix : A-4

X-ray Scattering from Charge, Spin and Orbital Densities in Condensed Matter Systems

(This brief description is based on the book "X-ray Scattering and Absorption by Magnetic Materials" by S.W. Lovesey and S.P. Collins, Oxford Univ. Press, Oxford (1996))

Scattering Amplitude Operator (G)

Dimensionless quantum mechanical operator describing the probability of scattering events (Fermi's Golden Rule) between photons and charge, spin and orbital densities of a system. G (= $\alpha I + \beta * \sigma$) is augmented by a 2 * 2 matrix to describe the polarization states of photon.

Scattering length : $f = r_o \langle G \rangle$

Absorption and Scattering Cross-sections are related to the amplitude operator and r_o is the Thomson length (coupling of photon to the electronic charge).

Absorption :

Imaginary part of the Amplitude Operator (G)'s matrix elements with respect to the states of the target and averaged over the polarization states of the primary beam. $\alpha \sim \mathrm{Im}(r.G)$

Elastic Scattering :

Products of the diagonal elements of G with respect to the states of the target and averaged over the polarization states of the primary beam. $CS = r^2 \mathrm{Tr}\{\mu |\langle G \rangle|^2\}$

Inelastic Scattering :

Products of the off-diagonal elements of G with respect to the states of the target and averaged over the polarization states of the primary beam. $\mathrm{Tr}\{\mu |\langle G^* G(t) \rangle|^2\}$

Absorption & Thomson Scattering :

Absorption limits the volume for Thomson scattering.

Electron-Photon Hamiltonian : $(1/2m)\,[(e/c)A \,.\, (e/c)A] \;\rightarrow\; \sigma = r^2 = (e^2/mc^2)^2$

Thomson length is the electron-photon coupling: $L_{th} \sim /\sigma * n$, and $L_{th} \sim 1/Z^4$

Absorption scattering length :

Away from resonances, higher energy X-rays can go through the materials easier (γ-ray goes through, very short wavelength so less sensitive to atomic scale features).

$L_{Abs} \sim \omega^3$

Thomson Cross-section : Scattering processes are favored for : $L_{th} * L_{Abs} \sim w^3 / Z^4$

High energy and low-Z samples are good for X-ray studies.

Nonresonant Scattering

Charge and Spin Scattering Length :

$f = r * \langle G \rangle = r [(\varepsilon' * \varepsilon) F_c(q) - i \lambda F_s(q) . B]$

$B = (\varepsilon' \times \varepsilon) - (k' \times \varepsilon') \times (k \times \varepsilon) + (k' . \varepsilon) . (k' \times \varepsilon') - (k . \varepsilon') . (k \times \varepsilon)$

- Spin scattering is reduced by a factor of $\lambda^2 = (E/mc^2)^2$ compared to the intensity of Charge scattering. Spin scattering is weak by a factor of 10^{-4}
- Charge scattering does NOT rotate ($\sigma \rightarrow \sigma'$) the incident plane polarization but spin scattering causes a partial rotation of the plane of polarization ($\sigma \rightarrow \pi'$).
- Spin scatt. Amplitude scales with <S>, the net spin polarization.
- For a plane polarized primary beam charge & spin amplitudes are 90^o out of phase with each other hence no interference is possible between them.

  The interference term would lead to a term in the cross-section that is linear in F_s and of the order of λ rather than λ^2, hence large ! There are three ways an interference can be realized :

  1. Crystals with NON-centrosymmetric space group. Structure factor complex.
  2. Primary beam Cricularly Polarized.
  3. Resonance : scattering near a core-hole. Complex phase component
     [(fc + ifs)] -> [(fc + fc' + ifc") + ifs] mixes fc" and fs and introduces term linear in fc" and fs (2fc"*fs) in intensity.
  4. Application of a magnetic field for ferromagnetic systems. Interference term is linear in magnetic orientation so by reversing the target's magnetisation causes the interference term to change sign.

Orbital Moment Scattering Length :

$i^* \lambda \langle Z \rangle . e'\rangle\langle e = - (l/hk2) < \Sigma j [\exp\{ik.Rj\} . \{k\rangle\langle pj\}]\rangle . (e'\rangle\langle e)$

- Orbital scattering scales with λ^2 (like spin scattering)
- Out of phase with charge scattering (like spin scattering)
- $\sigma \rightarrow \sigma'$ always vanishes identically.

Orbital Scattering vanishes under two conditions :

1. Free electrons (plane waves)
2. Electrons in a non-degenerate orbitals

(Quenching of orbital moments via the removal of degeneracy, e.g., crystal fields etc.)

How to Separate Orbital & Spin Magnetization using X-rays ?

Since the $\sigma \rightarrow \sigma'$ orbital scattering always vanishes whereas the spin amplitude is generally finite and scales with the projection of the magnetic polarization NORMAL to the diffraction plane (along the Scattering vector). The other three polarization channel is generally sensitive to both spin and orbital moments. Spin and Orbital contribution (relative) to the scattering can be extracted by linear polarization analysis of the scattered beam for primary beam linearly polarized.

$$I_{[\sigma \rightarrow \pi']} / I_{[\sigma \rightarrow \sigma']} \sim (\sin(\theta))^2 * \{3. F_l(q)/f_s(q) + 1\}^2$$

Neutron is sensitive to the total magnetic moment of the scattering centers hence it can not separate the orbital and spin contribution rather gives the total ($m_s + m_l$).

Determination of magnetisation densities

Neutron (polarized): $m_s + m_l$

X-ray (non-resonant) : m_s / m_l

Contribution to individual magnetization densities due to orbital moments and spin moments can be separated.

Resonant Scattering (Diffraction)

- Resonance introduces an additional phase-shift to the scattering photon. In general, for weak resonances, this leads to an interference of the non-resonant and the resonant amplitudes close to the resonant frequency.

- Magnetic resonant scattering does not give direct information about magnetization densities (like non-resonant magnetic scattering does).
- Magnetic resonant scattering is sensitive to the direction of local magnetic moments and is optimized when polarization is aligned with k' the direction of the scattered beam.
- Since resonant scattering involves a highly localized core-level scattering only occurs near the atomic site and form-factor effects can be neglected.
- For a single resonance, resonance enhancement of some feature is determined by the width of the white-line. The relative magnitude of resonance enhancement can be estimated by taking the ratio of the distance elastic amplitude starts to dominate and the width of the whiteline.

Resonances involving core-level excitations :

Structure factor (F(Q) acquires extra contributions from through the changes in the atomic form factors due to the electronic resonance that take place in the atom.

$$F(E) = f_o(E(k)) + f'(E_R) + i f''(E_R)$$

The physics is like that of a Lorentz Oscillator (the response of a damped harmonic oscillator driven by the x-ray field)

$$f'(E_R) \text{ --- KKT -} \rightarrow f''(E_R)$$

The resonance term gives chemical specificity.

$F''(E_R)$ is given by the absorption coefficient, a.

$$A \sim f''(E_R) \sim \text{Absorption Matrix element.}$$

Anisotropy of a shows up in the diffraction patterns if we use polarized light.

At resonance the M is dominated by the second-order term. The second-order term has the intermediate states in it. For different symmetries of intermediate states M is different.For highly anisotropic electronic states M is a tensor in a crystal. ATS : Anisotropic Tensor Susceptibility. Anisotropy in dielectric polarization response.

Nuclear Resonant Magnetic Scattering : Hyperfine splittings (coupling of nuclear spins to the total electronic spins J's). The magnetic intensity is finite and strongly dependent on

the evolving phase differences between each hyperfine transition. Quantum beats can be observed with pulsed SR beams.

Other types of weak scatterings in crystals :

Magnetization induced weak charge modulation : Periodicity : 1/2(magnetic unit cell)
Multiple(double) diffraction : Check by doing an azimuthal scan.
Double diffracted beam should have sharp dependence.

Interference Scattering :

Magnetic-Charge Interference Scattering :
Magnetic - Resonant Charge Interference Scattering (M-RC)
Resonant Magnetic - Charge Interference Scattering (RM-C)
The magnetic projection vector is normal to the scattering plane (parallel to scattering vector). Diffraction Plane : (for incident SR)
M-RC : Vertical or Horizontal
RM-C : Only Horizontal ($\pi \rightarrow \pi'$)

Resonance Line-shape and Exchange gap :
The resonance profile of magnetic reflections can be very sensitive to the existence of a gap. The effect of a gap may be seen in the line-shape even in the case where life-time width is larger than the gap size.

Appendix : A-5

Angle-Resolved Photoelectron Spectroscopy of Striped Phases of Nickelates

The physics of charge ordering in transition metal oxides have recieved a lot of research interest because of their possible connection to the phenomena of high Tc superconductivity and colossal magnetoresistance [108]-[110]. The two dimensional ordering of doped charges are believed to exist most robustly in comensurately doped nickel oxides [111][112]. We have recently perfomed Angle-Resolved Photoemission Spectroscopy (ARPES) on $La_{2-x}Sr_xNiO_4$ (x=1/3) using BL 10.0.1 at the Advanced Light Source to study how the single particle properties (spectrum) changes as the system goes through long-range charge stripe ordering. A clear feature around 1.5 eV binding energy is seen in all spectra which disperses about 250-300 meV to lower binding energies along (0,0) to (π,π).

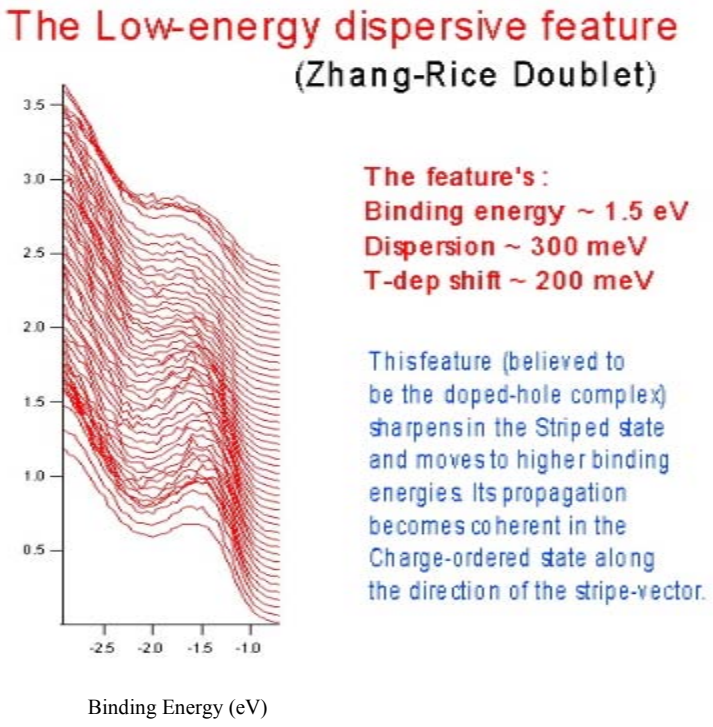

Figure A.5.1 **k**-dependence of the low-energy excitation feature (1.5 eV binding energy) in $La_{5/3}Sr_{1/3}NiO_4$ (x=1/3). The data is from a Brillouin zone cut parallel to the line from (0,0) to (π, π).

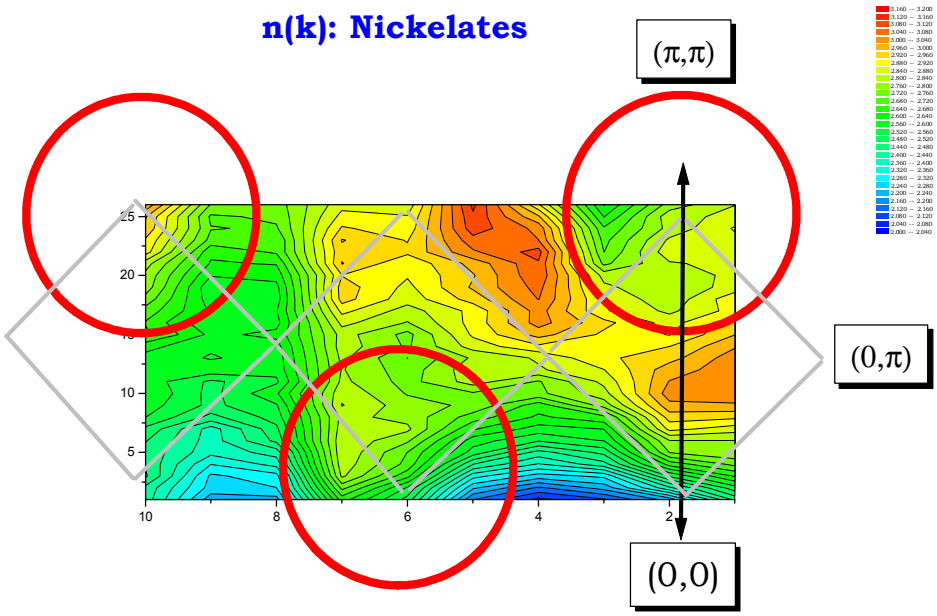

Figure A.5.2 Frequency integrated (up to 2 eV) spectral weight partial "**n(k)**" dependence of the low-energy excitation feature (1.5 eV binding energy). The data is from a Brillouin zone cut parallel to the line from (0,0) to (π, π).

This feature is believed to be the d^8L (doped hole complex) identified in earlier experiments [113]. This feature, in the x=1/3 compound shows a strong temperature dependence in intensity near the charge ordering transition (T_{co} ~ 230 K) where as the most of the valence band changes very little as a function of temperature. In addition to sharpening of the spectral intensity, the feature moves to higher binding energy at lower temperatures (150-180K) by about 200 meV. Sharpening of spectral intensity is also strongly k-dependent. A frequency integrated spectral intensity of this feature (partial n(k)) is consistent with Luttinger sum rule within the limits of experimental error bars.

The anisotropic sharpening of the feature and its change in binding energy as a function of temperature near the metal-insulator transition can possibly be interpreted in terms of long-range ordering of doped charges [114]. More systematic work is necessary to check for this scenario.

Appendix : A-6

Phase-Sensitive X-ray Standing Wave Scattering Study of Doped Manganites

By creating an X-ray standing wavefield around a bulk Bragg reflection, it is possible to maximize the X-ray field intensity at different positions within the chemical unit cell of a sample [115]. From the observed differences in the valence band photoemission spectra as the wavefield position is moved, one can determine experimentally the contributions of valence electrons from different parts of the unit cell to the (energy) states in the valence band of the sample under study. Here we briefly report our preliminary findings in studying a layered manganite.

The perovskite structure is common to colossal magnetoresistive (manganite) and high-T_c superconducting (cuprate) materials. The origin of these effects are the Mn-O (or Cu-O) planes in the layered planar tetragonal structure of the perovskites, and "charge ordering" and "orbital ordering" of valence electrons in the Mn-O plane have been seen at low temperatures [47][102][103] (below T_{CO} = 217 K for $La_{1/2}Sr_{3/2}MnO_4$ (LSMO). Experiments were performed

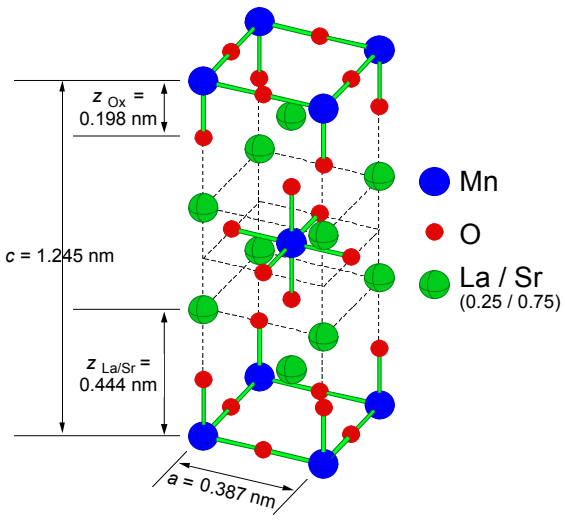

Figure A.6.1 Crystal structure of layered manganite $La_{1/2}Sr_{3/2}MnO_4$

at beamline X24A at the NSLS in collaboration with E. Nelson, J. Woicik et.al. [116]-[118]. The LSMO sample was cleaved in ultrahigh vacuum (10^{-10} torr) to expose the (001) surface. Four reflections – (114), (116), (204), and (213) – were examined in the backreflection configuration, at Bragg energies of $h\omega$ = 3017.3 eV, 3750.1 eV, 3773.8 eV, and 3882.6 eV, respectively. The increased angular width of Bragg reflections in backreflection accommodates the mosaicity of the sample. The monochrometer crystals were Si(111).

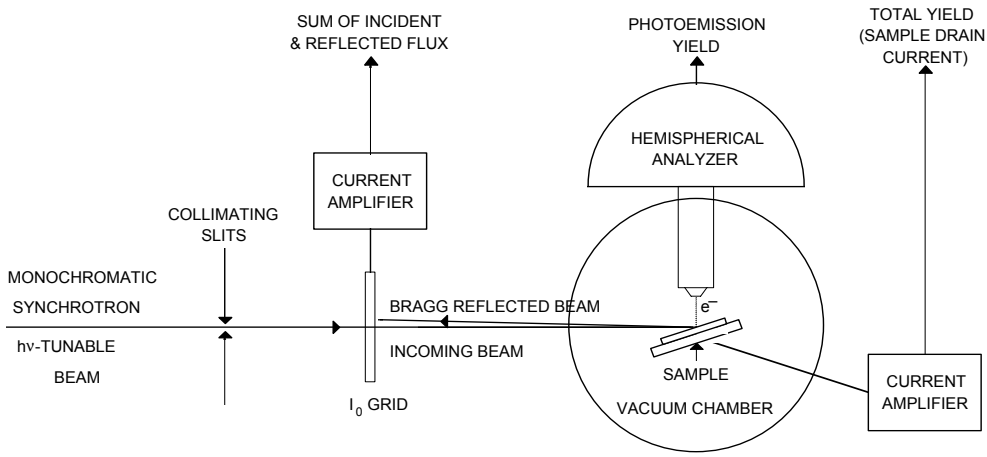

Figure A.6.2 A schematic of the x-ray standing wave scattering set-up (in the photoelectron mode).

Fig. A.6.3 shows the (114) photoemission XSW yields, respectively, of La, Mn, and O core-levels, and the Sr LMM Auger XSW yield, as well as the valence band photoemission XSW yield, taken with a hemispherical analyzer energy window which surrounds the entire valence band. The O 1s and La $3p_{3/2}$ core-level yields and Sr LMM Auger yield as well as the valence emission yield have a lineshape corresponding to a coherent position of zero, while the Mn 2p yield corresponds to a coherent position of 1/2. The valence band emission has a coherent fraction near zero, and looks more like the reflectivity. This lineshape suggests the contributions from Mn (coherent position 1/2) to the valence emission are similar in magnitude to the combined contributions from La, Sr, and O (coherent position 0), so the total X-ray structure factor for valence band emission cancels out. By setting the photon energy at the values for the maximum of the core-level XSW yields for either coherent position 0 or 1/2, we increase the X-ray electric field intensity and therefore electron emission at this position, while emission is minimized at the opposite position.

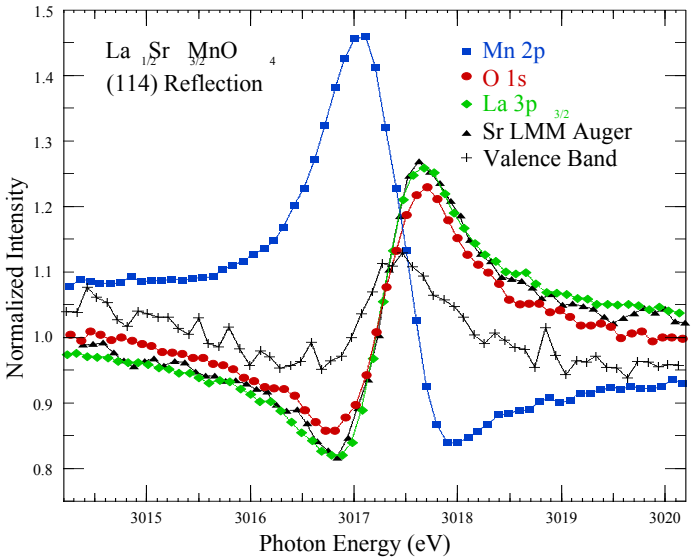

Figure A.6.3 Mn 2p, O 1s, La $3p_{3/2}$, and core-level photoemission XSW yields, Sr LMM Auger XSW yield and valence band photoemission XSW yield as a function of photon energy for the (114) backreflection of $La_{1/2}Sr_{3/2}MnO_4$.

High-resolution photoemission spectra [118] taken at these two photon energies, as well as a difference spectrum. Emission at the higher binding energy part of the valence band is enhanced when the standing wavefield is maximized on the Mn positions, indicating a higher density of Mn valence states at these energies. Similarly, the lower binding energy part of the valence band is higher in La, Sr, and O valence state density. The results for (204) reflection, which also separates Mn atoms from La, Sr, and O atoms in terms of coherent position, are similar to the (114) reflection data shown. However, the (116) and (213) reflections, which separate the O atoms in the Mn-O planes from those outside them, show no change in the valence band spectra lineshape as one moves the standing wavefield. This suggests that O 2p emission is very weak within the valence band near 4 keV photon energy. This is the first example of such study of d-electron systems to the best of our knowledge.

Core-Level X-Ray Standing Wave Study of Manganites

We examined the bulk atomic structure of the perovskite $La_{1/2}Sr_{3/2}MnO_4$ using photoemission-yield X-ray standing waves. Core-level X-ray standing waves (XSW) has the advantage over X-ray diffraction that it is element specific. The atomic position distribution of each of the four elements in $La_{1/2}Sr_{3/2}MnO_4$, can be separated.

Experiments were performed at beamline X24A at the NSLS. The $La_{1/2}Sr_{3/2}MnO_4$ sample was cleaved in ultrahigh vacuum (10^{-10} torr) to expose the (001) surface. Five reflections – (006), (114), (116), (204), and (213) – were examined in the backreflection configuration, at Bragg energies of $h\omega$ = 2987.6 eV, 3017.3 eV, 3750.1 eV, 3773.8 eV, and 3882.6 eV, respectively. The increased angular width of Bragg reflections in backreflection accommodates the mosaicity of the sample. The monochrometer crystals were Si(111). Core-level yields were monitored by defining the hemispherical analyzer energy window around the core-level peak. A sample bias is applied to keep the photoemission peak centered in the window as the photon energy is swept through the Bragg condition. Background yields were collected using a second energy window at binding energies just below the peak, and were subtracted from the on-peak yields.

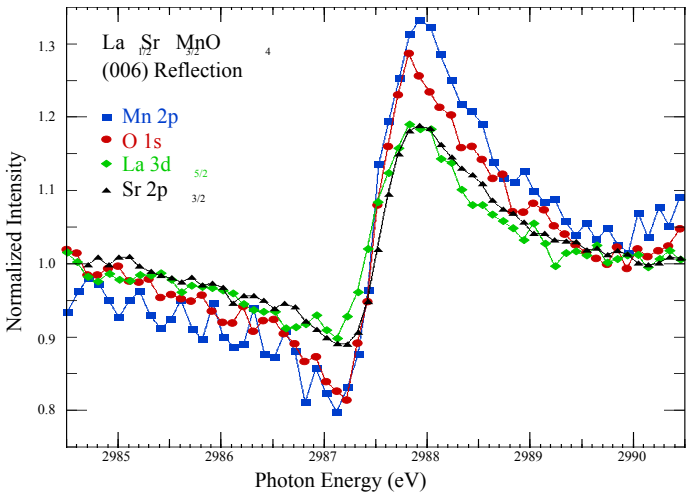

Figure A.6.4 Mn 2p, O 1s, La $3d_{5/2}$, and Sr $2p_{3/2}$ core-level photoemission XSW yields as a function of photon energy for the (006) backreflection of $La_{1/2}Sr_{3/2}MnO_4$.

Figures A.6.3 and A.6.4 show the (006) and (204) photoemission XSW yields, respectively, of La, Sr, Mn, and O core-levels. For the (006) reflection, all four yields have a lineshape corresponding to a coherent position of zero, indicating that the position distribution of each element is centered on the diffraction plane. For the (204) reflection, the La and Sr yields again have a lineshape with a coherent position of zero, while Mn and O have lineshapes indicating coherent positions of 1/2. The other three reflections – (114), (116), and (213) – single out the Mn, in-plane O, and out-of-plane O atoms, respectively, placing them at a coherent position of 1/2 while the remaining atoms are at a position of zero. This contrast between the yields directly indicates the differences in the position distributions of each element in $La_{1/2}Sr_{3/2}MnO_4$.

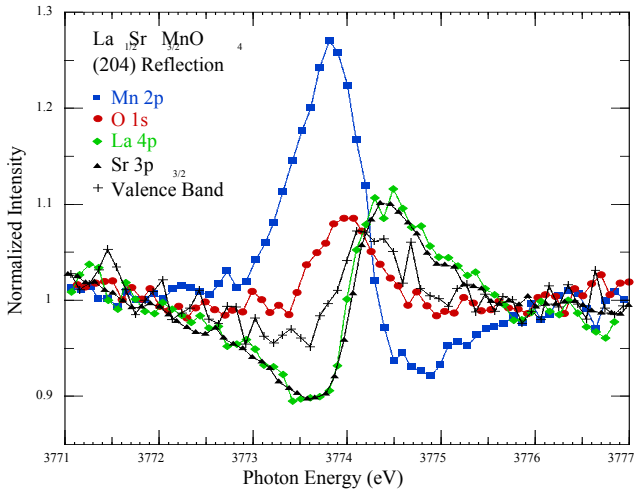

Figure A.6.5 Mn 2p, O 1s, La 4p, and Sr $3p_{3/2}$ core-level photoemission XSW yields as a function of photon energy for the (204) backreflection of $La_{1/2}Sr_{3/2}MnO_4$.

The size of the features, which corresponds to the coherent fraction or amplitude of the XSW structure factor, is largest for Mn, intermediate for O, and smallest for La and Sr in Fig. A.6.4. This agrees with the known perovskite structure in that the Mn atoms and half of the O atoms are in crystallographic positions on the Mn-O planes, while the La, Sr, and other half of O atoms are distributed about the diffracting planes at distances which are not integer or half-integer multiples of the diffraction plane spacing. Note the small feature size of the O 1s yield of Fig. A.6.5. For the (204) reflection, the XSW contribution of half of the O atoms outside the Mn-O planes cancels that of the in-plane O atoms, for a total coherent fraction near zero.

The XSW data for all five reflections are consistent with the perovskite structure and lattice parameters determined from X-ray diffraction. In addition, for all five reflections, the La and Sr core-level yields produced the same lineshape and feature size. This is a direct verification that La substitutes exactly in the Sr sites, without distortion due to the difference in the atomic sizes of La and Sr.

Appendix : A-7

[2]Study of BULK electronic structure of strongly correlated quantum systems by using a novel momentum-resolved inelastic emission soft x-ray spectrometer at the Advanced Light Source, Berkeley, Ca.

Purpose/Goals:

The electronic structure of strongly correlated quantum systems continues to be a major class of unsolved problems in physics despite several decades of intense research efforts. The discovery of high-temperature superconductivity, colossal magnetoresistance and novel dielectric properties in doped Mott insulators presents major intellectual challenges to the scientists working in the field. Well-developed momentum-resolved spectroscopies such as photoemission and neutron scattering cannot directly probe valence charge-charge correlation (fluctuation) spectrum in a momentum-resolved manner as angle-resolved photoemission probes the single-particle occupied states and neutrons do not couple to the electron's charge directly. Optical Raman and Infrared spectroscopies measure charge-fluctuation spectrum (occupied to unoccupied) but they are confined to the zone center (q~0) hence not momentum-tuned. A good understanding of momentum-resolved charge-charge correlation function is of paramount importance to gain insights into the charge-transport mechanisms in correlated systems. In addition, there is no momentum-resolved *bulk* spectroscopy to study the unoccupied states. To fill in this gap in electronic spectroscopies we proposed last year to build a novel momentum-resolved inelastic soft x-ray spectrometer [a].

Approach/Methods:

Previous work by some of us have demonstrated that such experiments are possible in the hard x-ray (~10 keV) regime [b][c] where the scattering experiments need to be done under resonant conditions (K-edge) due to weak non-resonant cross-section. However, under these coupling to

[2] A text version of a proposal for LDRD/LBNL funding (FY-2002).

the valence excitations is indirect for hard x-rays. Based on our recent experiences from NSLS, APS and ALS, we believe that such experiments would greatly benefit the use of soft x-rays because they could provide much better energy resolution with higher efficiency. The fact that the energy resolution of resonant inelastic soft x-ray scattering is not limited by the lifetime broadening of the core-excited state creates many excited possibilities. It would be invaluable to be able to look at the charge, lattice, or spin excitation in highly correlated materials with kT-resolution. ALS would be an ideal place to build such a momentum-resolved inelastic scattering spectrometer for its high brilliance at the soft x-ray energies as well as the expertise that exist in developing such an emission spectrograph utilizing variable line spacing grating in spectrograph mode and thus improving the performance by a significant amount. Although compared to the hard x-ray regime where the beam can transfer a large momentum into the scattering system the soft x-ray regime is limited due to relatively smaller momentum transfer. However, the available momentum transfers in soft x-rays still offer the possibilities to probe more than half way along (0,0) to (π, 0) of the first Brillouin Zones of late transition metal oxides with better momentum as well as energy resolution compared to the hard x-ray regimes.

Initial progress has been made in designing a novel spectrograph that is optimized around Mn L-edge where it will focus on studying the charge excitations near the edge of the Mott gap (effective charge gap) in insulating maganites. The gap anisotropy measured at finite momentum transfers would provide information about the particle-hole pair excitations along different directions [b][c]. Particle-hole pair excitations are the key to understand the anomalous transport properties of manganites (including CMR effect in the presence of magnetic fields). These results can also complement the studies on manganites using angle-resolved photoemission (ARPES) [d] by providing insight about the k-resolved information about the unoccupied electronic states although somewhat indirect. Another key aspect of manganite physics is the orbital degeneracy (unlike copper oxides) [e]. Recently, numerical work has shown that the effects of orbital degeneracy and fluctuations can be probed through the q-dependence of the charge gap as seen in inelastic x-ray scattering [f].

In general, given its bulk-sensitivity and weak-coupling nature as well as the ability to probe dispersive behavior of the unoccupied bands and charge-charge dynamical correlations over the significant part of the Brillouin zone, we believe that inelastic soft x-ray scattering has the potential to emerge as an important experimental tool to fill in a gap in spectroscopic knowledge of the electronic structure of correlated systems. Advanced Light Source has the unique

capabilities to fill in this gap of scientific knowledge. We believe that ALS can take a lead in such an endeavor and this effort could lead to new directions in exploring the momentum resolved electronic structures of different kind of materials, highly correlated electron systems being only one class of them.

Present status of the project and design concepts:

During the first year of the LDRD (FY2001), we have successfully completed the optical design of the spectrograph (Fig. Below) which is fully optimized for the study of magnites near the L-absorption edges. A through analysis of our new design have shown that at this energy our 1.5 m long spectrograph will provide an energy resolution of 50 meV and will be 100-1000 times more efficient than any other existing design. In future it is possible to further improve the energy resolution down to 10 meV by making the spectrograph longer in length and by increasing the groove density to increase the dispersive power but at the expense of flux. All the optics and back illuminated 2-D CCD detector with pixel size of 13.5 micron have been ordered. Collaboration with MES project (D. S.) at the ALS has been developed who also have interest in the use of such an emission spectrograph for MES research.

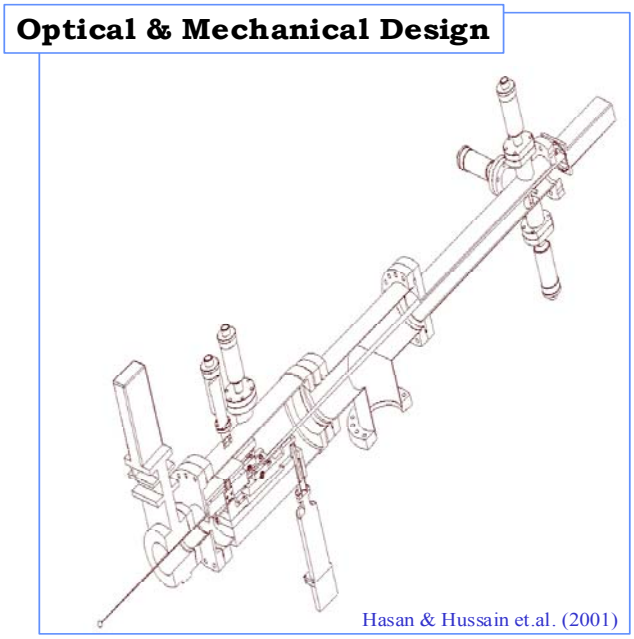

The implementation of the following design characteristics have made this design very unique in providing a considerable efficiency gain over the existing spectrographs:

1) The instrument is made slitless for higher throughput. This requires a pre-focusing system to illuminate the sample with a spot size of 5 microns in the vertical direction.

2) For collection of higher photon flux the acceptance solid angle has been increased by incorporating a spherical pre-mirror.

3) A blazed grating, optimized for the desired 640 eV, with Ni coating is used to provide highest possible efficiency of the system.

4) Finally a back illuminated 2-D CCD detector (2kx2k arrays, efficiency upto 80%) with high spatial resolution (pixel size 13.5 microns) and designed for normal orientation to principal rays from grating is utilized.

The result of all these optimization is 100-1000 fold increase in efficiency for detection of soft x-rays with high-energy resolution. Such an improvement is necessary to carry out the proposed experiments, as inelastic scattering signal is several order of magnitudes smaller than the normal elastic emission (fluorescence) signal.

[a] M. Z. Hasan et.al., *"Filling-in a Big Gap : A Novel Soft X-ray Momentum-Resolved Inelastic X-ray Scattering Spectrometer at the Advanced Light Source",* **LDRD Grant Proposal**, LBNL(2000-01)

[b] M. Z. Hasan et.al., *Science* **288**, 1811 (2000).

[c] M. Z. Hasan et.al., *NSLS Research Highlight*, **2-78** (2000).

[d] Y. -D. Chuang et al, *Science* **292**, 1509 (2001).

[e] Y. Tokura and N. Nagaosa, *Science* **288**, 462 (2000).

[f] S. Ishihara & S. Maekawa, *Phys. Rev. B* **62**, 2338 (2000).

Future Direction (Second Phase) for SXIS :

The second phase of the construction would include several additional capabilities :

- Additional degrees of freedom to allow for polarization dependent study under all possible scattering geometries. Initial experiments near Cu L-edge performed at ALS BL-7 by M. Z. Hasan et.al. have been reported already [120]
- Integration of a **magnetic field** (up to 13 T).
- Integration of a **high-pressure** cell to allow for tuning the pressure-field.

These are among the most unique aspects of inelastic x-ray scattering adding to its versatility in terms of diverse applications.

Appendix : A-8

Media Coverages, Interviews and Press Releases for work related to this thesis

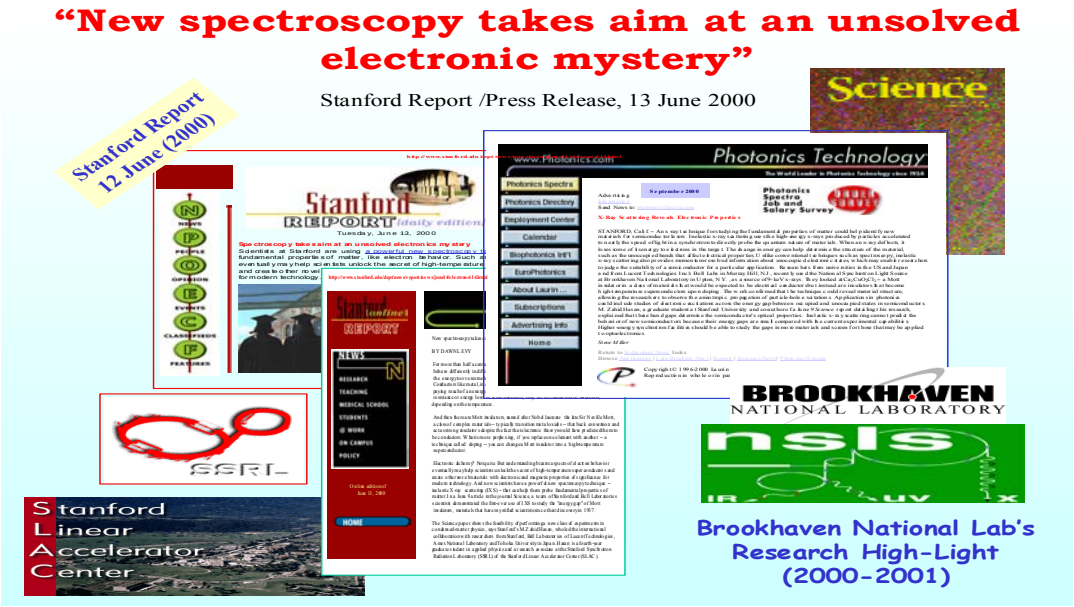

Press Release & Interview by Stanford News Services & Bell-Labs/Lucent Tech. (June 12, 2000)

"New spectroscopy takes aim at an unsolved electronic mystery"

http://www.stanford.edu/dept/news/report/news/june14/electron-614.html

http://www.stanford.edu/dept/news/pr/00/3electron614.html

Photonics magazine (September, 2000)

"New X-Ray Scattering Reveals Electronic Properties"

http://www.photonicstechnology.com/sep00/techxray.html

Japanese Media (June 2000) http://www.kahoku.co.jp/NEWS/2000/06/20000610J_02.htm

Cover Story at Stanford Report (June 13, 2000)

Spectroscopy takes aim at an unsolved electronic mystery

"Scientists at Stanford are using a powerful new spectroscopy technique to probe fundamental properties of matter, like electron behavior. Such an understanding eventually may help scientists unlock the secret of high-temperature superconductors and create other novel materials with electronic and magnetic properties of significance for modern technology."

http://www.stanford.edu/dept/news/pr/00/3electron614.html

http://www.stanford.edu/dept/news/report/indextues.html

Bibliography

[1] R. B. Laughlin, D. Pines, J. Schmalian, B. P. Stojkovic, P. Wolynes, *Proc. Natl. Acad. Sci. USA* **97**, 32-37 (2000).

[2] W. Schulke "*Inelastic Scattering by Electronic Excitations*" in Handbook on Synchrotron Radiation, Vol. 3, eds. G. Brown and D.E. Moncton, Elsevier Science, The Netherlands (1991); E. Burkel "*Inelastic Scattering of X-rays with Very High Resolution*", Springer Tracts in Modern Physics, Springer-Verlag, Berlin (1991).

[3] E. D. Isaacs and P. M. Plaztman, *Phys. Today* **49** (2), 40 (1996).

[4] L. Van Hove, *Phys. Rev.* **95**, 249 (1954).

[5] D. Pines and P. Nozieres, *The Theory of Quantum Liquids* Vol. 1, Adv. Book Classics Benjamin, New York (1989).

[6] C. J. Sparks, *Phys. Rev. Lett.* **33**, 262 (1974)

[7] P. Eisenberger, P.M. Platzman and J. Winick, *Phys. Rev. B* **13**, 2377 (1976)

[8] K. Hamalainen et.al., *Phys. Rev. Lett.* **67**, 2850 (1991)

[9] C.-C. Kao et.al., *Phys. Rev. B* **54**, 23 (1996)

[10] P. M. Platzman and E. D. Isaacs *Phys. Rev. B* **57**, 11 107 (1998).

[11] P. Abbamonte et.al., *Phys. Rev. Lett.* **83**(4), 860 (1999)

[12] F. Sette et.al., *Phys. Rev. Lett. 77*, **83** (1996)

[13] M. H. Krisch et.al., *Phys. Rev. Lett.* **78**, 2843 (1997)

[14] F. Sette et.al., *Science* **280**, 1550 (1998).

[15] G. Ruocco et.al., *Nature* **379**, 521 (1996)

[16] E. D. Isaacs et.al., *Phys. Rev. Lett.* **76**, 4211 (1996).

[17] P. M. Platzman and P. E. Eisenberger, *Phys. Rev. Lett.* **33**, 152 (1974).

[18] P. E. Eisenberger, P. M. Platzman and K. C. Pandy, *Phys. Rev. Lett.* **31**, 311 (1973).

[19] P. M. Platzman et.al., *Phys. Rev. B* **46**, 12943 (1992).

[20] J. P. Hill et.al., *Phys. Rev. Lett.* **77**, 3665 (1996).

[21] B. C. Larson et.al., *Phys. Rev. Lett.* **77**, 1346 (1996).

[22] D. Gibbs et.al., *Phys. Rev. Lett.* **61**, 1241 (1988).

[23] E. D. Isaacs et.al., *Phys. Rev. Lett.* **75**, 1178 (1995).

[24] K. Hamalainen et al., *Phys. Rev. B* **61**, 1836 (2000).

[25] J. P. Hill et. al., *Phys. Rev. Lett.* **80**, 4967 (1998).

[26] H. Kondo et.al., *Phys. Rev. B* **64**, 14414 (2001).

[27] Webinfo Link: http://www.esrf.fr

[28] H. Wiedemann "Synchrotron Radiation Primer" (1998).
Web-reference : http://www-ssrl.slac.stanford.edu

[29] G. D. Mahan, *Many Particle Physics*, Plenum, New York (1983).

[30] D. Pines, *Elementary Excitations in Solids*, Benjamin, Massachusetts (1983).

[31] C. A. Burns et.al., *Phys. Rev. Lett.* **83**, 2390 (1999).

[32] H. Raether, *Springer Tracts in Modern Physics*, vol. **88**, Springer, Berlin (1980).

[33] J. Fink, *Unoccupied Electronic States*, eds J. C. Fuggle and J. E. Inglesfield, Topics in Applied Physics Vol. **69**, Springer, Berlin (1992).

[34] J. Kotran et.al. (unpublished).

[35] P. M. Platzman and P. A. Wolff, *Waves and Interactions in Solid State Plasmas*, Academic Press, New York (1973).

[36] J. P. Hill et.al., *Phys. Rev. Lett.* **77**, 3665 (1996).

[37] A. Vom Felde et.al., *Europhys. Lett.* **4**, 1037 (1987).

[38] A. Vom Felde, J. Sprosser-Prou and J. Fink, *Phys. Rev. B* **40**, 10181 (1989).

[39] W. Schulke et.al., *Phys. Rev. B* **33**, 6744 (1986).

[40] W. Schulke, H. Nagasawa, S. Mourikis and A. Kaprolat, *Phys. Rev. B* **40**, 12215 (1989).

[41] W. Schulke, H. Schulte-Schrepping and J. R. Schmitz, *Phys. Rev. B* **47**, 12426 (1993).

[42] J. G. Bednorz and K. A. Muller, *Z. Phys. B* **64**, 189 (1986).

[43] P. W. Anderson, *Science* **23**, 1996 (1987).

[44] P. W. Anderson, *Science* **256**, 1526 (1992).

[45] J. Orenstein and A. J. Millis, *Science* **288**, 468 (2000).

[46] Y. Tokura and N. Nagaosa, *Science* **288**, 462 (2000).

[47] M. Imada, A. Fujimori, Y. Tokura, *Rev. Mod. Phys.* **70**, 1039 (1998) .

[48] V. J. Emery and S. A. Kivelson, *Nature* **374**, 434 (1995) .

[49] N. F. Mott, *Proc. Phys. Soc. London A* **62**, 416 (1949).

[50] J. Hubbard *Proc. Phys. Soc. London A* **277**, 237 (1964).

[51] P. W. Anderson *Phys. Rev.* **115**, 2 (1959).

[52] J. Zaanen, G. A. Sawatzky, J. W. Allen *Phys. Rev. Lett.* **55**, 418 (1985).

[53] Z. X. Shen et. al., *Science* **267**, 343 (1995).

[54] A. Auerbach, *Interacting Electrons and Quantum Magnetism*, Springer-Verlag, New York (1994).

[55] P. Fulde, *Electron Correlations in Molecules and Solids*, Springer Series in Solid-State Sciences 100, Springer-Verlag Berlin Heidelberg (1991).

[56] E. Fradkin, *Field Theories of Condensed Matter Systems*, Frontiers in Physics, Addison-Wesley (1991).

[57] D. Vaknin et.al., *Phys. Rev. B* **41**, 1926 (1990).

[58] T. R. Thurston, et al., *Phys. Rev. B* **40**, 4585 (1989).

[59] H. Yoshizawa, et al., *J. Phys. Soc. Jpn.* **57**, 3686 (1989).

[60] S.-W. Cheong, et al., *Phys. Rev. Lett.* **67**, 1791 (1991).

[61] B. Keimer et.al., *Phys. Rev. B* **46**, 14034 (1992).

[62] T. E. Mason, G. Aeppli and H. A. Mook, *Phys. Rev. Lett.* **68**, 1414 (1992).

[63] T. R. Thurston, et al., *Phys. Rev. B* **46**, 9128 (1992).

[64] J. Tranquada, et al., *Nature* **375**, 561 (1995).

[65] J. Tranquada, et al., *Phys. Rev. Lett.* **78**, 338 (1997).

[66] Z. X. Shen, et al., *Phys. Rev. Lett.* **70**, 1553 (1993).

[67] A. G. Loeser, et al., *Phys. Rev. B* **56**, 14185 (1997) .

[68] Z. X. Shen and D. S. Dessau, *Phys. Rep.* **253**, 1 (1995) .

[69] J.C. Campuzano et.al.,*The Gap Symmetry and Fluctuations in High-Tc Superconductors*, J. Bok et al., Eds. , Plenum, New York, (1998)

[70] H. Ding, et al., *Phys. Rev. Lett.* **74**, 2784 (1995)

[71] F. Ronning et. al., *Science* **282**, 2067, (1998).

[72] S. LaRosa et.al., *Phys. Rev. B* **56**, R525 (1997).

[73] C. Kim et.al., *Phys. Rev. Lett.* **80**, 4245 (1998).

[74] Y. Y. Wang et.al., *Phys. Rev. Lett.* **77**, 1809 (1996).

[75] P. Schiffer et.al., *Phys. Rev. Lett.* **75**, 3336 (1995).

[76] M. Z. Hasan, E. D. Isaacs et.al., *Science* 288, 1811 (2000).

[77] F. C. Zhang and T. M. Rice, *Phys. Rev. B* **37**, 3759 (1988).

[78] K. Tsutsui , T. Tohyama, S. Maekawa *Phys. Rev. Lett.* **83**, 3705 (1999).

[79] K. Tsutsui , T. Tohyama, S. Maekawa *Phys. Rev. B* **61**, 7180 (2000).

[80] S.L. Cooper et.al., *Phys. Rev. B* **47**, 8233 (1993).

[81] C.-C. Kao et.al., *Rev. Sci. Instrum.* **66**, 1699 (1995).

[82] L. L. Miller et.al., *Phys. Rev. B* **41**, 1921 (1990).

[83] T. Ide and A. Kotani, *J. Phys. Soc. Jpn* **68**, 3100 (1999).

[84] P. W. Anderson, *A Career in Theoretical Physics*, World Scientific Series in 20th Century Physics (World Scientific, Singapore, (1994), Vol. 7).

[85] Z. Zou and P. W. Anderson, *Phys. Rev. B* **37**, 627 (1988).

[86] R. B. Laughlin, *Phys. Rev. Lett.* **79**, 1726 (1997).

[87] E. H. Lieb and F. Y. Wu, *Phys. Rev. Lett.* **20**, 1445 (1968).

[88] J. Solyom, *Adv. Phys.* **28**, 201 (1979).

[89] W. Stephan and K. Penc, *Phys. Rev. B* **54**, R 17269 (1996).

[90] K. Penc and W. Stephan, *Phys. Rev. B* **62**, 12707 (1996).

[91] J. W. Allen et.al., *J. Phys. Chem. Solids* **56**, 1849 (1995).

[92] Claessen, G.-H. Gweon, F. Reinert, J. W. Allen, W. P. Ellis, Z.-X. Shen, C. G. Olson, L. F. Schneemeyer, and F. Levy, *J. Electron Spectrosc. Relat. Phenom.* **76**, 121 (1995).

[93] B. Dardel et.al., *Phys. Rev. Lett.* **67**, 3144 (1991).

[94] A. Sekiyama et.al., *Phys. Rev. B* **51**, 13 899 (1995).

[95] M. Nakamura, M. Nakamura, A. Sekiyama, H. Namatame, A. Fujimori, H. Yoshihara, T. Ohtani, A. Misu, and M. Takano, *Phys. Rev. B* **49**, 16 191 (1994).

[96] N. Motoyama, H. Eisaki and S. Uchida, *Phys. Rev. Lett.* **76**, 3212 (1996).

[97] H. Kishida et. al., *Nature* **405**, 929 (2000).

[98] C. Kim et. al., *Phys. Rev. Lett*. **77**, 4054 (1996).

[99] C. Kim et. al., *Phys. Rev. B* **56**, 15589 (1997).

[100] M. Z. Hasan et. al., *Physica C* **341-348**, 781 (2000).
M. Z. Hasan et.al., *NSLS Research Highlight*, **2-78** (2000).

[101] M. Z. Hasan et. al., *J. Elect. Spect. Rel. Phen.* **114-116**, 705 (2001).
M. Z. Hasan et.al., *Phys. Rev. Lett*. (2001) cond-mat/0102485.

[102] Y. Murakami et al., *Phys. Rev. Lett*. **81**, 582 (1998).

[103] H. Kawano et.al., *Phys. Rev. Lett.* **78**, 4253 (1997).

[104] This work was performed in collaboration with S. Larochelle, M. Greven, J. Arthur et.al.

[105] I. S. Elfimov et.al., cond-mat/9901058 (1999).

[106] For information on coherent x-ray sources see the LCLS project at SLAC : http://www.ssrl.slac.stanford.edu/

[107] S. W. Lovesey and S. P. Collins, *"X-ray Scattering and Absorption by Magnetic Materials"* Oxford Univ. Press, Oxford (1996)).

[108] S. A. Kivelson, E. Fradkin and V. J. Emery, *Nature* **393**, 550 (1998).

[109] Y. Tokura and N. Nagaosa, *Science* **288**, 462 (2000).

[110] X. J. Zhou et.al., *Science* **286**, 272 (1999).

[111] S-W. Cheong et.al., *Phys. Rev. B* **49**, 7088 (1994).

[112] T. Katsufuji et.al. *Phys. Rev. B* **54**, R14 230 (1996).

[113] M. Satake et.al. *Phys. Rev. B* **61**, 15515 (2000).

[114] M. Z. Hasan et.al., *Advanced Light Source Comp. (Research Report)*, BL-**10.0.1** (2001).

[115] J. C. Woicik et al., *Phys. Rev. Lett.* **84**, 773 (2000).

[116] This work was done in collaboration with Erik Nelson (Stanford), Joe Woicik (NIST & Brookhaven) et.al., and the samples were provided by S. Larochelle et.al.

[117] J. C. Woicik, M. Z. Hasan et.al., *National Synchrotron Light Source Research Activity Report*, x-24A, **7**-280 (1999).

[118] E. Nelson, J. C. Woicik, M. Z. Hasan, Z.X. Shen, D. Heskett and L.E. Berman. *National Synchrotron Light Source Research Activity Report*, X-24A, (2000).

[119] J. C. Woicik et.al., *Phys. Rev. B* **64**, 125115 (2001).

[120] M. Z. Hasan, E.D. Isaacs, A. Agui, C. Sathe, T. Käämbre, J.-E. Rubensson, J. Nordgren, E.M. Gullikson, P. Platzman et.al., *Advanced Light Source Comp.*, LBNL, **7.0.1** (1998)